



UNIVERSIDAD
DE LA REPÚBLICA
URUGUAY

ESQUEMAS DE UNITARIZACIÓN PARA DIFRACCIÓN HADRÓNICA

ANÁLISIS DEL POMERON SOFT EN EL LHC

Tesis de Maestría
Lic. Marina Maneyro

Posgrado en Física
Facultad de Ciencias
Universidad de la República

Mayo de 2023

Orientadores:

Dr. Emerson Luna
Dra. Marcela Peláez





UNIVERSIDAD
DE LA REPÚBLICA
URUGUAY

UNITARIZATION SCHEMES FOR HADRONIC DIFFRACTION

ANALYSIS OF THE SOFT POMERON AT THE LHC

Master's Thesis

Lic. Marina Maneyro

Physics Postgraduate Program

Faculty of Sciences

University of the Republic

May 2023

Supervisors:

Dr. Emerson Luna

Dr. Marcela Peláez



*MEMBERS OF THE DEFENSE TRIBUNAL
MIEMBROS DEL TRIBUNAL DE DEFENSA*

Dr. Lucía Duarte
Universidad de la República

Dr. Sofía Favre
Universidad de la República

Dr. Cristina Aguilar
Universidade Estadual de Campinas

Dr. Magno Machado
Universidade Federal de Rio Grande do Sul

Co-advisor / Co-orientador:
Dr. Emerson Luna
Universidade Federal de Rio Grande do Sul

Substitute / Suplente:
Dr. Rodrigo Eyheralde
Universidad de la República

Date / Fecha: 30th of June, 2023

Acknowledgments

I would like to extend my thanks to my supervisors, Marcela and Emerson, for their instruction, mentorship, and encouragement throughout this project. I would also like to acknowledge the support of my family in all my undertakings.

Additionally, I am grateful for the teachers, classmates, colleagues and proofreaders who have been a part of my journey in the past few years. Finally, I acknowledge the financial resources provided by ANII to carry out this project as part of FCE_2021_166479.

Resumen

Los protones son uno de los componentes fundamentales de los núcleos atómicos. Aunque su descubrimiento se remonta al comienzo del siglo XX, todavía hay muchos aspectos de sus interacciones que no se comprenden totalmente. Esta tesis se centra en las colisiones elásticas y difractivas entre protones, y entre protones y antiprotones. Estos tipos de colisiones pueden ocurrir en aceleradores de partículas, como los experimentos del CERN, para energías cada vez mayores.

Debido a la prevalencia de eventos de bajo momento transferido en estas colisiones, no es posible aplicar métodos perturbativos en su descripción. Por esta razón, un enfoque comúnmente utilizado para la difracción hadrónica se basa en el Pomeron *soft*, un estado que surge de la teoría de Regge.

Uno de los problemas presentes en el enfoque del Pomeron es que puede introducir violaciones de la unitariedad. La unitariedad impone un límite en la tasa de crecimiento de las secciones eficaces hadrónicas. Dos métodos ampliamente utilizados para restaurar la unitariedad son los esquemas eikonal y de matriz U, que llevan a predicciones asintóticas distintas (a altas energías).

Esta tesis ofrece una comparación entre ambos esquemas para determinar si los datos más recientes de choques entre protones para altas energías favorecen la unitarización eikonal o la de la matriz U. La pregunta se abordó utilizando datos de los experimentos TOTEM y ATLAS del LHC. La metodología consistió en obtener ajustes χ^2 para los datos de sección eficaz, sección eficaz diferencial y parámetro ρ , usando cálculos de teoría de Regge dominados por el Pomeron.

Motivados por el reciente descubrimiento de otro estado de Regge conocido como Odderon, el análisis incluye un modelo para esta contribución. Se realizó una comparación entre los resultados basados en el Pomeron y aquellos que también incluyen al Odderon.

Proporcionamos nuevos estimativos para los parámetros asociados al Pomeron y Odderon para los dos conjuntos de datos altamente divergentes que fueron considerados. De nuestro análisis, destacamos que los resultados favorecen el factor de fase $\xi_0 = -1$ para el Odderon. Esta es la fase que lleva a un acoplamiento no nulo para el Odderon. Esta conclusión es independiente de la elección del esquema de unitarización.

Palabras clave: Fenomenología de interacciones fuertes, física de altas energías, scattering hadrónico, Pomeron soft, unitarización, Odderon.

Abstract

Protons are one of the building blocks of atomic nuclei. Although their discovery dates back to the beginning of the 20th century, many aspects of their interactions are yet to be understood. This thesis focuses on elastic and diffractive collisions between protons, and protons and antiprotons. These kinds of collisions can occur at particle accelerators, such as the experiments at CERN, for increasingly high energies.

Due to the prevalence of low transferred momentum events in these collisions, it is not possible to apply perturbative methods in their description. Because of this, a common approach to hadronic diffraction is based on the soft Pomeron, a state arising from Regge theory.

One of the issues present in the Pomeron approach is that it may lead to unitarity violations. Unitarity imposes a limit on the rate of growth of hadronic cross-sections. Two widely used methods for restoring unitarity are the eikonal and U-matrix schemes, leading to distinct asymptotic predictions (at high energies).

This thesis offers a comparison of both of these schemes, to determine whether the latest high-energy data for proton scattering favors eikonal or U-matrix unitarization. The question was addressed using data from the TOTEM and ATLAS experiments at the LHC. The methodology consisted of producing χ^2 fits for cross-section, differential cross-section, and ρ parameter data, from Regge theory calculations dominated by the Pomeron.

Motivated by the recent discovery of another Regge state known as the Odderon, our analysis takes into account a model for this contribution. A comparison was drawn between results based on the Pomeron and those also including the Odderon.

We provide new estimations for Pomeron and Odderon parameters for both of the highly divergent datasets considered. From our analysis, we highlight that the results favor the Odderon phase factor $\xi_0 = -1$. This is also the phase leading to a non-zero Odderon coupling. This conclusion is independent of the choice of unitarization scheme.

Keywords: *Phenomenology of strong interactions, high-energy physics, hadron scattering, soft Pomeron, unitarization, Odderon.*

Contents

Introduction	1
1 Quantum Chromodynamics and Hadron Scattering	4
1.1 Quantum Chromodynamics	4
1.1.1 Fundamental Characteristics	5
1.1.2 Perturbative Quantum Chromodynamics	9
1.2 Scattering Cross-sections	11
1.3 Hadronic Processes	12
2 S-matrix Formalism	15
2.1 Historical Background	16
2.2 Unitarity	18
2.2.1 Optical Theorem	19
2.2.2 Further Implications of Unitarity	22
2.3 Analyticity and Crossing	23
2.3.1 Analyticity and Causality: An Example from Optics	23
2.3.2 Analyticity in Relativistic Scattering	24
2.3.3 Crossing	26
3 Regge Theory	28
3.1 Conceptual Overview	28
3.2 Partial Wave Expansion	29
3.3 Domains of Amplitude Convergence	30
3.3.1 Continuation to Complex Angular Momenta	32
3.4 Analytical Continuation for All Channels	32
3.4.1 Asymptotic Behavior in the Watson-Sommerfeld Representation	36
3.4.2 Signatures of Regge Poles	37
3.5 Regge Poles	38
3.5.1 The Pomeron	40

3.5.2	The Odderon	41
3.6	Some Open Questions in Regge Theory	42
4	Unitarization Schemes	44
4.1	Unitarity in the Impact Parameter Representation	45
4.2	The Eikonal and the U-matrix	46
4.2.1	Eikonal Scheme	47
4.2.2	U-matrix Scheme	47
4.3	Scheme Properties and Differences	48
5	Models and Methodology	50
5.1	Included Reggeons	50
5.1.1	Pomeron	51
5.1.2	Correction to the Pomeron Trajectory	53
5.1.3	Secondary Reggeon Trajectories $f - \alpha$ and $\omega - \rho$	55
5.1.4	Odderon	58
5.1.5	Summary of Fitted and Fixed Parameters	59
5.2	Computed Observables	60
5.3	Experimental Data	61
5.4	Fitting Method: χ^2	62
6	Results	64
6.1	Fits for the Pomeron	64
6.2	Fits for the Pomeron plus Odderon	72
6.2.1	The $\xi_0 = -1$ case	72
6.2.2	The $\xi_0 = +1$ case	79
6.3	Comparisons for all models at high energy	79
7	Conclusions	82
	Bibliography	88
	Appendices	89
A	Useful Tools in Particle Scattering	89
A.1	Units	89
A.2	Mandelstam Variables	90
B	Kinematics	91

List of Figures

1.1	Electric charge screening	7
1.2	Plot of the variation of the QED coupling with energy, based on [1].	8
1.3	Plot of the variation of the QCD coupling with energy, based on [2].	9
1.4	Example of a low-order Feynman diagram for an interaction between two quarks, mediated by the exchange of a virtual gluon.	10
1.5	Diagrams representing fermion-gluon vertices and gluon-gluon vertices contributing to QCD.	11
1.6	Types of processes conserving quantum numbers.	14
1.7	Diagram exemplifying the rapidity gap in Diffractive Deep Inelastic Scattering (DDIS).	14
2.1	Feynman diagram for the s-channel exchange of a scalar.	25
2.2	Diagram of the s-channel singularities for the two-body equal-mass example.	25
2.3	Diagram of the three physical regions associated with an equal-mass scattering in the s, t and u channels.	27
2.4	Diagram of the scattering amplitude singularities (all channels) for the two-body equal-mass example.	27
3.1	Scattering of a plane wave by a spherical potential.	30
3.2	Illustrations of convergence when allowing complex values of $\cos \theta$	31
3.3	Domain of convergence hyperbola for imaginary ℓ in the complex $\cos \theta$ plane (with Lehmann ellipse).	33
3.4	Integration contours for scattering amplitudes in the Watson-Sommerfeld representation.	34
3.5	Deformed contours for scattering amplitudes in the Watson-Sommerfeld representation.	35
4.1	Illustration showing impact parameter b in a particle collision event.	45

5.1	Diagram of Pomeron pole exchange between two protons.	52
5.2	Feynman diagram for the two-pion loop contribution to Pomeron exchange in nucleon interaction.	55
5.3	Example of proton-proton event diagram with Pomeron and ρ -meson contributions.	55
5.4	Chew-Frautschi plot of $ t = m^2$ (energy) vs spin (angular momentum) for leading mesonic trajectories, with a linear fit. Data from PDG [3] .	56
6.1	Total cross-section and ρ parameter fits for pp (\bullet , \blacktriangle , \blacktriangledown) and $p\bar{p}$ (\circ) channels. Results obtained using eikonal unitarization for Models I and II.	68
6.2	Differential cross-section for pp (\blacktriangle , \blacktriangledown) channel. Results obtained using eikonal unitarization for Models I and II.	69
6.3	Total cross-section and ρ parameter fits for pp (\bullet , \blacktriangle , \blacktriangledown) and $p\bar{p}$ (\circ) channels. Results obtained using U-matrix unitarization for Models I and II.	70
6.4	Differential cross-section for pp (\blacktriangle , \blacktriangledown) channel. Results obtained using U-matrix unitarization for Models I and II.	71
6.5	Total cross-section and ρ -parameter fits for pp (\bullet , \blacktriangle , \blacktriangledown) and $p\bar{p}$ (\circ) channels. Results obtained using eikonal unitarization for Models III and IV using $\xi_0 = -1$	75
6.6	Differential cross-section for pp (\blacktriangle , \blacktriangledown) channel. Results obtained using eikonal unitarization for Models III and IV using $\xi_0 = -1$	76
6.7	Total cross-section and ρ parameter fits for pp (\bullet , \blacktriangle , \blacktriangledown) and $p\bar{p}$ (\circ) channels. Results obtained using U-matrix unitarization for Models III and IV using $\xi_0 = -1$	77
6.8	Differential cross-section for pp (\blacktriangle , \blacktriangledown) channel. Results obtained using U-matrix unitarization for Models III and IV using $\xi_0 = -1$	78
6.9	High-energy comparison of results for Models I, I, III, and IV in the eikonal scheme. Also included is σ_{tot}^{pp} data obtained from cosmic-ray experiments (AUGER and TA).	80
6.10	High-energy comparison of results for Models I, I, III, and IV in the U-matrix scheme. Also included is σ_{tot}^{pp} data obtained from cosmic-ray experiments (AUGER and TA)	81
A.1	Diagram illustrating the considered four-momenta.	90
A.2	Feynman diagrams for the different (ρ)-channel reactions.	91
B.1	Momenta and scattering angle in the center-of-mass system.	92

List of Tables

5.1	Summary of the parameters and terms used for each Reggeon in Model I (without Odderon) and Model III (with Odderon).	59
5.2	Summary of the parameters and terms used for each Reggeon in Model II (without Odderon) and Model IV (with Odderon).	59
6.1	Fitted parameters obtained with Eikonal unitarization for the Pomeron (and secondary Reggeon) models.	66
6.2	Fitted parameters obtained with U-matrix unitarization for the Pomeron (and secondary Reggeon) models.	67
6.3	Fitted parameters obtained with Eikonal unitarization for the Pomeron plus Odderon models, for $\xi_0 = -1$	73
6.4	Fitted parameters obtained with U-matrix unitarization for the Pomeron plus Odderon models, for $\xi_0 = -1$	74
A.1	Dimensions in natural units for relevant quantities.	89

Introduction

Present day experimental capabilities have provided deeper knowledge of the structure of matter. In this context, the field of particle physics has enjoyed major landmark discoveries, enabled by colliders such as the LHC. At the core of the physics of elementary particles lies the Standard Model, providing a unified description of three distinct forms of matter interaction, comprised by electromagnetic, weak, and strong interactions. Despite this, many of the phenomena currently observed are yet to get complete first-principles descriptions.

This is the case for hadronic scattering events such as proton-proton collisions, which can be produced at increasingly high energies in laboratories. The study of these particles is tied to Quantum Chromodynamics (QCD), a theory within the Standard Model that has been extremely successful in its description of strong interactions. Strong interactions represent one of the four fundamental forces in nature, responsible for binding together the quarks that make up protons and neutrons.

Hadronic scattering at high energies includes significant contributions from diffractive processes. This category of events is not at present describable from QCD, as they do not correspond to the regime where perturbative techniques can be applied. Due to this, a central tool in diffractive scattering comes from Regge Theory [4–6]. This theory arose from the S-matrix theory, a candidate model for strong interactions in the pre-QCD era [7]. It explains processes such as proton-proton scattering by introducing the exchange of some ‘state’ known as the Pomeron. Pomeron physics has been used to obtain good phenomenological results for many decades. However, it is still unclear how it fits within QCD.

This thesis focuses on some problems that arise when using the Regge framework. In particular, it aims to determine whether the most recent collider data could shed light on aspects of this description. Some of these include unitarization schemes, the discrepancies in available datasets, and the inclusion of a counterpart of the Pomeron known as Odderon.

A known conflict in Regge theory is that the *soft* Pomeron (that is, the Pomeron used to describe diffractive or soft processes) violates unitarity. In order to reflect

the rise in hadronic cross-sections with energy, as observed in the experiments, the Pomeron description must have numerical parameters with particular characteristics.

However, these properties of the Pomeron may conflict with unitarity. The Froissart-Martin bound shows that although scattering cross-sections should increase, they must not do so at too high a rate [6, 8] for unitarity to be respected. Unitarity is a fundamental property of quantum theories, where the probabilities of all processes must add up to unity in order to be well defined. Although it has been suggested that unitarity violations could occur at energies far beyond our current experimental capabilities, compelling arguments of the contrary have been put forward as well.

In order to address the issue, unitarization methods have been developed which enforce the unitarity of Pomeron based predictions. This work compares the eikonal and U-matrix unitarization schemes commonly used in the area. Although the results obtained from both schemes are expected to be compatible at low energies they lead to different asymptotic behaviors at high energies. The goal is to elucidate if the latest LHC data could help determine which of the schemes results in better descriptions of the physical phenomena of interest. The data provides values of scattering observables for collisions of up to 13 TeV of energy.

The predictions of these unitarization methods were evaluated for data from two experiments: TOTEM and ATLAS. Although these experiments have obtained measurements of the same observables, the techniques applied by each of these collaborations lead to differences in the results obtained. These discrepancies lead to distinct estimations of the parameters linked to the Pomeron.

Recent TOTEM results have suggested that another state from Regge theory should be included in theoretical models of diffractive scattering [9, 10]. The contributions of this state known as the Odderon, are taken into account in the methodology of this thesis. The results of the models with and without the Odderon were contrasted for the different datasets and unitarization schemes considered.

The methodology utilized in this work was based on fitting the experimental data from ATLAS and TOTEM using the unitarized Regge framework. The fits were produced through χ^2 minimization, which provides tools to evaluate fit quality for each of the models used. It also results in new estimations of the numerical values of the parameters of the Regge states. These results were analyzed to determine if one of the unitarization schemes shows better agreement with high energy observations. The outcomes of the procedures also denote the effect of the Odderon inclusion and other model variations in the quality of the theoretical predictions.

In order to provide a more detailed picture of the questions addressed, this thesis is outlined as follows. Firstly, a general overview of QCD and hadronic diffraction

is provided in Chapter 1, highlighting the limitations that justify the need for Regge theory. Having established this, Chapter 2 provides a summary of S-matrix theory, which, besides being a rich framework in and of itself, explores some of the basic concepts that lead to Regge theory. Then, Chapter 3 describes Regge theory in detail, as well as the origins of the Pomeron and Odderon. As the introduction of the Pomeron has consequences for unitarity, the eikonal and U-matrix schemes implemented are described in Chapter 4, completing the theoretical background that underlies this work.

The following chapter explores the methodology that was followed, from the subtleties contained within the models used to the fitting procedure. The remainder of the thesis is dedicated to sharing the results obtained and highlighting the conclusions they lead to.

1 Quantum Chromodynamics and Hadron Scattering

This thesis focuses on some aspects of the description of proton interactions. Protons belong to a group of particles called hadrons, characterized by being composed of quarks. Quarks are fundamental particles sensitive to strong interactions, typically described using Quantum Chromodynamics (QCD), a field theory backed by extensive experimental evidence. However, explicit analytical calculations in QCD tend to be restricted to processes at high energy scales, through the use of perturbative methods. As a result, it is not always possible to obtain complete first-principle-based descriptions of all hadronic interactions from QCD.

Processes such as proton diffraction involve scales where perturbative QCD is not applicable. Section 1.3 will specify what diffraction entails in this context. Diffractive scattering phenomena represent a significant fraction of contributions to proton interactions, which motivates the need for alternative descriptions. Other implementations could rely on techniques such as effective theories, numerical simulations, and non-perturbative methods. This work's approach to the problem stems from Regge theory and is described in subsequent chapters.

In this chapter, general characteristics of QCD are introduced, along with further details about hadronic processes. The goal is to provide a general background of strong interactions, and thus give context to the theories and methods that will be introduced and applied in later chapters.

1.1| Quantum Chromodynamics

Quantum Chromodynamics is one of the main components of the Standard Model of particle physics. Alongside Quantum Electrodynamics (QED) and the Electroweak model, it describes fundamental interactions between quantum particles at relativistic speeds. As such it is necessary to consider its basic properties in order to understand its applicability and limitations for high-energy hadron scattering.

1.1.1| Fundamental Characteristics

Quarks, gluons, and color

QCD gets its name from the *color charges* associated with strongly interacting particles. These charges are analogous to the electric charges present in electrodynamic interactions. Hadrons like protons and neutrons have long been known to interact through the strong force, widely described as binding atomic nuclei. However, hadrons do not carry a net color charge. These particles were found to be bound states of quarks, color-charged elementary particles.

Quantum Chromodynamics provides a framework for the interaction between these point-like charges (not possessing internal structures). Hadrons can be classified into two groups, mesons and baryons¹. Mesons (such as pions and kaons) are typically composed of a quark and an antiquark, held together by the strong interaction. Baryons, on the other hand, usually contain three quarks. Protons (the hadrons of interest in this thesis) belong to the latter group.

As a gauge quantum field theory, QCD describes the strong force through particle exchanges. Particles that mediate an interaction are known as gauge bosons. Although some of these elementary particles can be detectable, they are usually exchanged as *virtual particles* [12]. These intermediate states share some of the properties of their *real* counterparts but can carry different masses and energies. *Virtual particles* cannot be detected experimentally because their presence is both allowed and restricted by the uncertainty principle. As such, they can be thought of as existing for extremely brief periods of time. Despite this, their inclusion in interaction calculations is well established.

In the same way QED (the field theory for Electromagnetism) can describe a Coulomb force as an exchange of virtual photons, QCD describes quark interactions as mediated by gluons. Gluons are gauge bosons carrying color charges. This property of gluons presents a first example of the differences between Electrodynamics and Chromodynamics. Photons have no electric charge and therefore do not interact with each other, but gluons do interact with other gluons (QCD is non-Abelian). Furthermore, there are three quark color charges (red, blue, green and their corresponding anti-colors for antiquarks) forming eight different possible color states for the gluons, compared to just one type of photon.

¹This classification is based on the quark model [11], taking into account the particles' valence quarks (those determining a hadron's quantum numbers). In reality, more complex descriptions are needed to fully model the hadron structure.

1. QUANTUM CHROMODYNAMICS AND HADRON SCATTERING

Color confinement, asymptotic freedom, and Chiral Symmetry Breaking

The physical phenomena related to the strong interaction present a few very important features. One characteristic behavior is referred to as *color confinement*. It relates to the fact that quarks and gluons have not been observed isolated in nature, and appear to always be present forming bound states (the hadrons). To accurately reflect this, a fundamental property of QCD is that only colorless particles should be allowed. Therefore, colored particles must always be contained in color-neutral bound states. This is yet to be fully proven from first principles.

Lattice simulations² have shown (for static quarks) that the quark and antiquark forming a meson are linked by a *flux tube* [13]. A consequence of this behavior is that the microscopic force between the particles remains constant as the distance between them varies. This is the case at large distances (of the order of the size of hadrons), where the potential increases linearly [14]. This is distinct from other interactions. It is well known, for example, that when separating electric charges the strength of their interaction decreases.

Confinement can be understood by considering that an effort to separate bound quarks leads to the creation of a quark-antiquark pair³. The nature of the strong interaction makes this more energetically favorable than a simple separation of the linked particles. In other words, instead of further “stretching” the flux tube, the increased distance “snaps” the flux tube, resulting in two bound states with their respective connecting tubes.

The confinement phenomenon applies to all color-charged states, including gluons which, unlike photons, cannot be directly observed [15]. Confinement also implies that the experimental study of strong force phenomena will not be possible using point-like particles. Therefore, it will require modeling internal hadron structures. These structures must reflect the distributions of partons (quarks and gluons) consistent with the results from probing each hadron.

A second special property of the strong interaction is known as *asymptotic freedom*, given by the magnitude of the strong interaction at different energy scales. It is tied to the fact that quarks seem to behave like free particles within hadrons. In other words,

²Lattice field theories can be developed by discretizing spacetime in a lattice. Although this does not necessitate that they will be analytically solvable, it allows for the application of Monte Carlo methods. The resulting simulations can provide very useful information on behaviors that can not be easily understood otherwise. Due to the unique characteristics of QCD, they are particularly useful when investigating its properties.

³Particle production is allowed by quantum field theory, provided that the energy available is greater than the rest mass energy of created particles and relevant quantum numbers are conserved. Given that antiparticles have charges opposite to the associated particle, this implies that production will be of particle-antiparticle pairs.

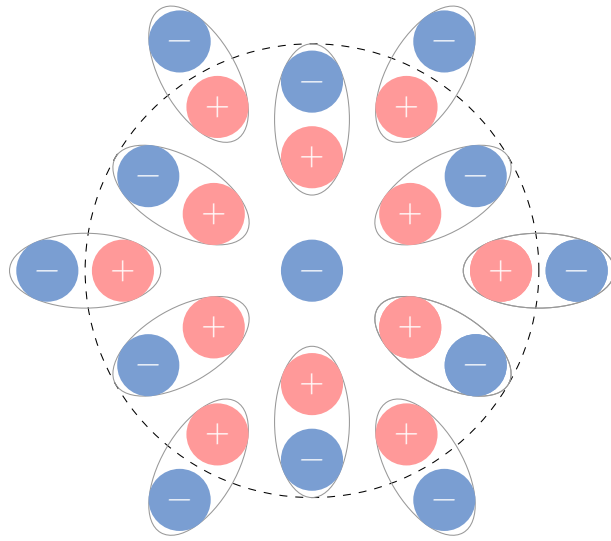


Figure 1.1: Electric charge screening

the strong interaction becomes weaker at high energies, taking into account that length scales are inversely proportional to energy and momentum scales.

Empirical evidence for asymptotic freedom arose from attempts to understand the structures within protons, validating the parton models that had been postulated at the time. Hadrons were initially expected to simply be elementary particles, in agreement with the fact that they could not be separated into smaller elements. Attempts to classify hadrons led to the proposal of quarks as constituent particles, but their physical nature was unclear. Furthermore, the quarks predicted by parton models carried fractions of elementary charge e , unlike previously known particles.

The discovery of quarks was realized through deep inelastic scattering experiments at SLAC (Stanford Linear Accelerator Center) [16, 17]. The experiments probed the insides of protons by colliding electrons and hydrogen atoms at high energies. The evidence gathered on the quark composition of hadrons also provided clues about the interactions occurring within them. As a result, it led to the development of the concept of asymptotic freedom and reconciled it with the seemingly contradictory idea of confinement [18, 19]. Proving that QCD successfully reproduced this behavior was instrumental to its acceptance as the leading theory for strong interactions.

The strength of an interaction can be represented through a coupling constant for a given theory. Contrary to what the name suggests, in quantum field theories, the value of the coupling can depend on the distance of the interaction. Qualitatively, the variation can be understood in terms of charge screening.

When measuring the charge of an electron, in light of quantum field theory, the presence of said charge is not the only effect detected. The electron could, for example,

1. QUANTUM CHROMODYNAMICS AND HADRON SCATTERING

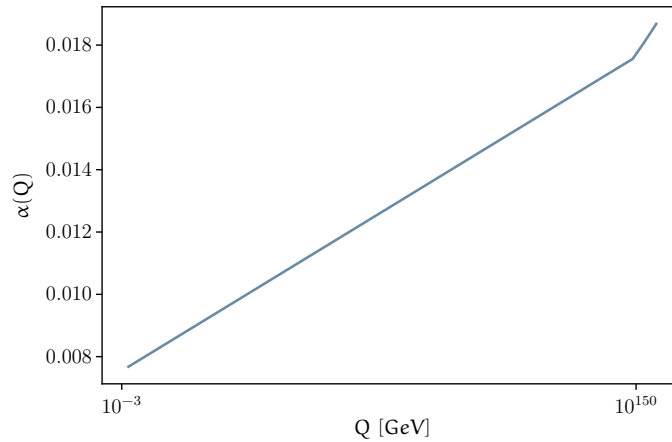


Figure 1.2: Plot of the variation of the QED coupling with energy, based on [1].

emit virtual photons, which in turn decay into electron-positron pairs. Electromagnetic interactions lead to the produced positrons being positioned closer to the initial electron, effectively causing the polarization of the space surrounding the initial charge.

Probing the area with a test charge, the perceived effect of the initial electron will be modified by the polarization, and its charge is said to be screened (as illustrated in Figure 1.1). The effective charge will depend on where the probing takes place, and therefore on the scale of the interaction. In this case, the measured charge decreases with distance from the particle, and so does the strength of the coupling α_{QED} . This corresponds to a smaller coupling at low probing energies (see Figure 1.2). Note how the plot shows extremely slow growth for the coupling. In reality, the scaling is expected to have a Landau pole. However, it occurs at such high energy⁴ that it is not within the scope of the measurable.

Focusing on QCD again, it is useful to consider how screening occurs if, instead of measuring the electric charge of an electron, the color charge of a quark is probed. In the same way electron-positron pairs are produced in QED, Chromodynamics allows for the production of quark-antiquark pairs surrounding the initial quark. Unlike what happens with photons, it is also possible to have gluons producing gluon pairs, which also affect the measured charge.

Favorable distributions will place color charges equal to the original quark's charge closer to it. The resulting behavior, in this case, is charge anti-screening. Accordingly, the QCD coupling α_{QCD} increases for larger distances. Therefore it is greater at low energies and smaller at high energies (Figure 1.3). Asymptotic freedom means quarks

⁴Roughly 10^{277} GeV if considering only the electron, 10^{34} GeV in the Standard Model [20].

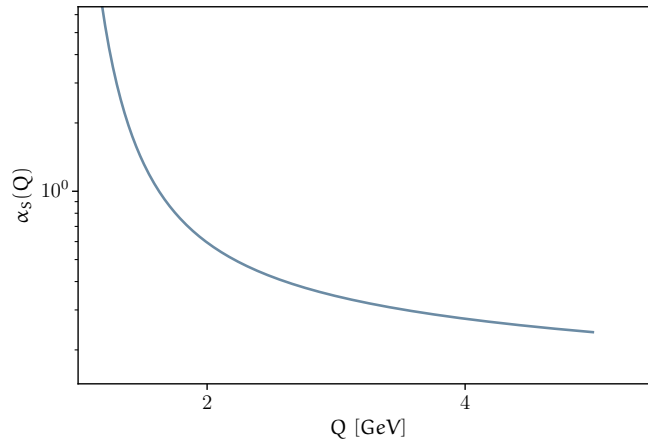


Figure 1.3: Plot of the variation of the QCD coupling with energy, based on [2].

are essentially “free” in terms of their mutual strong interactions when placed close together (inside a hadron), but their bond strengthens as they get separated, leading to confinement. The counter-intuitive short-distance nature of the interactions displays another significant way color charge forces differ from electric charge forces [15].

Another important property displayed in QCD is *Spontaneous Chiral Symmetry Breaking*. QCD has Chiral Symmetry (invariance under a parity transformation) only when quark masses are taken to be zero. However, using a QCD Lagrangian without quark mass terms gives rise to non-zero effective masses for quarks. In this model, there is no energetic cost associated with the creation of a (massless) quark-antiquark pair. Therefore, the vacuum could be filled by any number and combination of these pairs. The effect of the interactions between them is analogous to including the mass terms, giving rise to effective masses for valence quarks within hadrons [21]. This broken symmetry also explains the huge difference between the mass of a proton and the mass of its valence quarks.

1.1.2| Perturbative Quantum Chromodynamics

High energy coupling values related to *asymptotic freedom* have relevant consequences when trying to obtain testable predictions from QCD. As is the case for other theories, exact calculations of physical observables can be difficult to produce. However, it may be possible to write approximate solutions by adding perturbative corrections to a simpler (solvable) case. Successive corrections correspond to a power series for a parameter taken to be small. In the case of field theories such as QED and QCD, perturbative approximations can be performed using the corresponding coupling constants as expansion parameters. A given observable f can be expressed

1. QUANTUM CHROMODYNAMICS AND HADRON SCATTERING

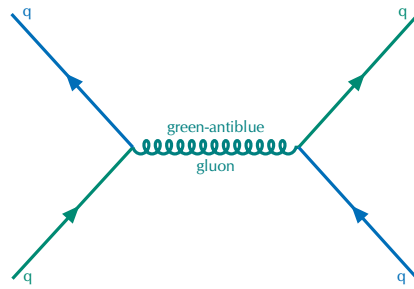


Figure 1.4: Example of a low-order Feynman diagram for an interaction between two quarks, mediated by the exchange of a virtual gluon.

as a series in the following way:

$$f = f_0 + f_1\alpha + f_2\alpha^2 + \dots \quad (1.1)$$

Generally, only first and second-order terms are considered. Increasing orders in α correspond to the exchange of a higher number of virtual particles.

Different terms in the expansion of probability amplitudes for a reaction can be represented as a Feynman diagram. The diagrams serve as a visual interpretation of the factors and integrals present in the calculation. An example of a QCD diagram is included in Figure 1.4. Each kind of particle (fermions, gluons, photons, etc.) is represented by a different style of line. Wherever these lines meet, there is an associated vertex, which contributes to the order of the interaction in terms of α . It is possible to define a set of Feynman Rules for each Field Theory, relating the graphical elements with mathematical expressions. These include the types of vertices allowed by a given interaction Lagrangian, as well as the types of particle lines [12].

QCD includes three distinct types of vertex, which are presented in Figure 1.5. The gluons (curled lines) can interact with fermions (straight lines). Gluon-gluon interactions can also occur, in two distinct ways. One gluon vertex is associated with a cubic term in the Lagrangian, and the other a quartic term.

In the case of QCD, the coupling is small only at high energies, as previously shown. Therefore perturbative methods cannot be applied to large-scale strong processes. To study an interaction it is necessary to consider its characteristic length scales to determine if this approximation is usable. This discussion is further developed in Section 1.3, but before that, it is convenient to introduce the main scattering observable, the cross-section.

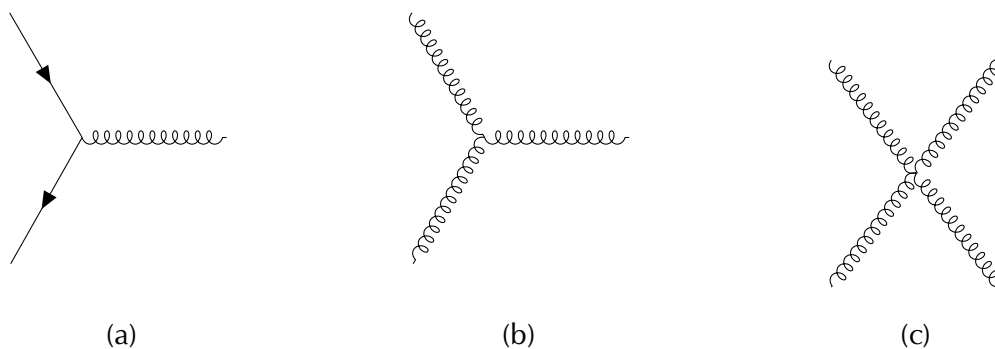


Figure 1.5: Diagrams representing fermion-gluon vertices and gluon-gluon vertices contributing to QCD.

1.2| Scattering Cross-sections

The study of elementary particles and their behavior is centered on scattering experiments. It is possible to cause beams of particles to collide and then measure the outcomes. Final states are determined by the beams of particles selected, and the momentum provided to the beams prior to an interaction. Accordingly, it is essential to define an observable that contains information on the probability of producing any of the states that could result from a particular collision.

Probabilities for a given process are tied to a *cross-section*, a quantity intrinsic to each scattering experiment. When describing classical collisions against a target with minimal non-contact interactions with the incoming particles, the cross-section is given by the size of the target. The area that the target presents for the collisions determines the odds of the incoming particles hitting it or continuing past it.

In particle physics defining an effective cross-section requires taking into account the deflection caused by non-contact interactions. Moreover, there is the possibility of non-elastic scattering where the final states may contain a different set of particles than the initial state. Each outgoing set (allowed by quantum number and energy-momentum conservation) has its own cross-section and contributes to the total or inclusive cross-section [12, 22].

Cross sections can be defined by considering a detector (placed at an arbitrary angle from the incoming beam) and the particles it is expected to measure. The differential cross section for a detector spanning solid angle $d\Omega = \sin\theta d\theta d\phi$ is defined as:

$$\frac{d\sigma}{d\Omega} = \frac{\text{Number of scattered particles detected in } d\Omega}{\text{Total number of scattered particles}} \quad (1.2)$$

Consequently, it represents the probability of finding a scattered particle traveling in a particular direction. Due to conservation, each solid angle corresponds to a particular

1. QUANTUM CHROMODYNAMICS AND HADRON SCATTERING

value of outgoing momenta. In terms of classical scattering, $d\sigma$ represents the area that an incoming particle needs to traverse to be scattered at angle $d\Omega$. The total cross-section for a process is obtained through integration over the solid angle:

$$\sigma = \int \frac{d\sigma}{d\Omega} d\Omega. \quad (1.3)$$

When working with quantum relativistic particles, distinct processes have associated probabilities stemming from the relevant field theories. That information will be included in the cross-sections. It is possible to define partial cross-sections for specific processes or categories. This allows, for example, to work with separate cross-sections for elastic and inelastic contributions.

In the relativistic case, the cross-sections do not correlate to target sizes. However, they are still expressed in units of area (typically in *barns*⁵). Inclusive cross-sections (also known as total cross-sections, but not to be confused with Eq. (1.3)) contain probability information for all viable processes in a scattering experiment, and result from adding all partial contributions. Probabilities depend on the energy involved in the process and therefore on the momentum of incoming particles. As an example, elastic scattering tends to dominate at lower energies, as the energy level does not favor the production of extra particles or the fragmentation of bound states.

Cross-sections will be discussed further in the following chapters, including some details of their calculation in quantum field theories. Due to the topic of this work, the concept will be relevant throughout, as it is the main observable considered in hadronic scattering.

For currently accessible energy scales there are available cross-section and differential cross-section datasets which were considered in the methodology applied in this thesis. These quantities were calculated from scattering amplitudes, as obtained from Regge theory. A further observable, known as the ρ -parameter was also taken into account. The parameter relates the real and imaginary parts of scattering amplitudes (in the forward direction) and is also studied at the LHC.

1.3| Hadronic Processes

When considering hadronic processes it is useful to apply classifications according to the length scales involved. To that end, it is possible to define two broad categories: *soft* and *hard* processes.

Hard processes involve large transferred momentum scales and can be treated

⁵1b (barn) = 10^{-28}m^2 ,

perturbatively. Predictions for these interactions typically require knowledge of the distribution of partons inside each hadron. These distributions are not wholly perturbative. However, they can be separated from the perturbative treatment of the problem as they are universal to processes involving the same hadrons [23]. The presence of these two approaches to working with hadronic scattering illustrates some of the issues that arise when seeking to develop comprehensive models for these phenomena.

Soft processes, on the other hand, are characterized by a length scale of the order of the involved hadron's size (R). This is a large scale in the context of strong interactions, as due to confinement it will not be possible to separate quarks beyond this distance. Consequently, it does not allow the application of perturbative Chromodynamics (pQCD).

The transferred momentum scale of a soft process can be expressed as $|t| \sim 1/R^2$ (where t refers to the Mandelstam variable, see Appendix A.2). The behavior of its differential cross-section in terms of t is $d\sigma/dt \sim e^{-R^2|t|}$. Therefore processes with high transferred momentum (high t) are suppressed [23].

Soft cross-sections at high energy can be phenomenologically described as dominated by the exchange of a Pomeron, which will be introduced in later chapters. This approach poses questions regarding the relationship between the soft Pomeron and QCD, obscured by the unknown physics contained in the Pomeron object.

This thesis focuses on soft phenomena and the Pomeron description. These processes are dominant in high energy scattering [24]. A group of processes typically associated with soft scales (low transferred momentum) are known as hadron diffraction. The term diffraction was chosen in analogy with optics, where the diffraction of a wave by an object produces a pattern of intensity peaks and valleys [25]. In hadronic diffraction, it is also possible to observe maxima and minima in the differential cross-sections [23].

Diffraction scattering is characterized by large *rapidity gaps*. These gaps refer to angular regions of space where no outgoing particles are detected after a collision (see Figure 1.7) [26]. More precisely, identifying a diffractive event requires the presence of a rapidity gap that is not exponentially suppressed. This means that the number of diffractive events N should not decrease according to $dN/d\Delta\eta \sim e^{-\Delta\eta}$ (or faster) as the gap size $\Delta\eta$ increases.

A perhaps more intuitive notion of diffraction is a process in which particle quantum numbers are not exchanged, as is the case in elastic scattering (e.g. $pp \rightarrow pp$)⁶. This definition may not always succeed at ruling out non-diffractive processes, however, it works well at high energies, where these non-diffractive events become less likely.

⁶It may be useful to note that in the literature elastic processes are often discussed separately from inelastic diffractive processes, or as a particular case in hadronic diffraction [27].

1. QUANTUM CHROMODYNAMICS AND HADRON SCATTERING

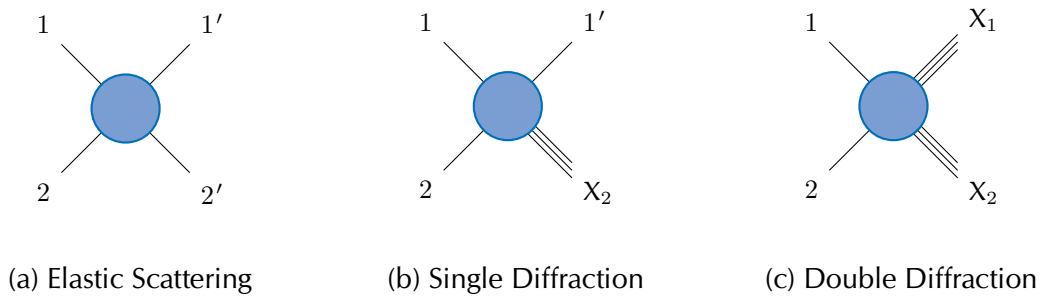


Figure 1.6: Types of processes conserving quantum numbers.

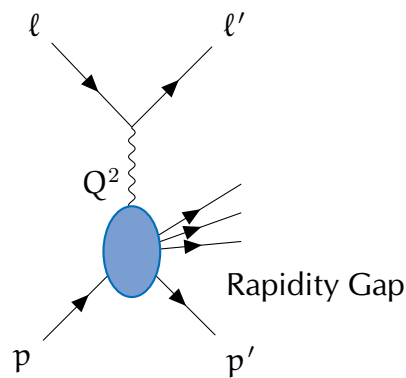


Figure 1.7: Diagram exemplifying the rapidity gap in Diffractive Deep Inelastic Scattering (DDIS).

Other diffractive processes are, for example, single and double diffraction, where one or both of the incident hadrons engender a set of particles (while conserving quantum numbers), as seen in Figure 1.6.

Further research has identified processes such as Diffractive Deep Inelastic Scattering (Figure 1.7) involving two length scales, one soft and one hard. These are also categorized as diffractive because they display the same characteristic rapidity gap behavior.

As was previously mentioned, diffractive phenomena can be described through Pomeron physics. In order to introduce the methodology involved, the next chapter discusses S-Matrix theory. The study of the S-Matrix and its properties produces ways to calculate scattering observables and gives rise to Regge theory and the Pomeron.

2 S-matrix Formalism

The S-matrix can be used to represent scattering processes in a variety of theories, including quantum field theories as well as non-relativistic quantum mechanics. The following chapter provides a brief overview of the goals of S-matrix Theory, developed as a possible contender for a complete model of strong interactions as QCD was emerging. The most relevant properties are also discussed, as their study leads to useful methods still applied in hadronic physics.

The S-matrix operator is defined as the transformation of an initial scattering state $|i\rangle$ into a final state $|f\rangle$, as expressed in the following equation:

$$|f\rangle = S |i\rangle. \quad (2.1)$$

The states are associated with free particles (outside the presumably short range of the interactions) and defined at times $t_i = -\infty$ and $t_f = +\infty$, respectively. Consequently, the S-matrix can be written using the time evolution operator for the system (\mathcal{U}) from t_i to t_f , as follows.

$$S \equiv \mathcal{U}(-\infty, +\infty) \quad (2.2)$$

In quantum field theory, the evolution operator can be calculated from the Hamiltonian of the theory.

In agreement with the quantum superposition principle, the S operator is linear. Its elements are also taken to be Lorentz invariant functions of the kinematic variables of the system, making the S-matrix independent of the chosen frame of reference. Other relevant properties, their physical significance and their consequences will be developed in further sections of this chapter, including unitarity, the focus of this thesis.

Usage of the S-matrix and the properties and principles tied to it were developed intensely in the 1960s, although the resulting theory was surpassed by QCD in the following decade. The next section provides a brief overview of the chronology and motivations behind the S-matrix theory of strong interactions.

2.1| Historical Background

The S-Matrix, also known as the scattering matrix, was initially introduced in 1937 as part of a model for composite nuclei [28]. A few years later, it was proposed as a foundation of elementary particle scattering by Heisenberg [29]. Heisenberg believed that the S-matrix formulation could eventually replace the work performed from a Hamiltonian. In the 1940s, advances developed in QED provided tools to address the scattering of particles such as electrons and photons. Heisenberg's approach was also shown to result in complete descriptions of those processes. Both methods were proven to be compatible, in the sense that S-matrix elements could be calculated through the perturbative methods (based on Feynman diagrams) that had already been established [30].

One of the issues arising in diagrammatic calculations from QED was the presence of divergences in the observables, which lead to the development of renormalization methods¹. From the S-matrix approach, however, divergences requiring infinite renormalization could automatically vanish by bypassing the Hamiltonian formalism. It was also expected that the S-matrix could help avoid the limitations inherent in perturbative calculations, which rely on weak couplings. In consequence, the S-matrix and its properties were studied extensively, leading to the S-matrix theory program, prevalent in the late 50s and early 60s.

The core idea behind S-matrix theory was developing a formalism that exploited the mathematical properties of this operator, such as unitarity and analyticity. If enough properties were formulated, it could lead to uniquely determined expressions for the S-matrix. This would be enough to make empirically verifiable predictions [31].

In order to understand the appeal of this, one could consider the roles of the fields in theories such as QED and QCD. Within them, the fields themselves are not entities of interest and instead constitute tools to construct physical observables. Therefore, it stands to reason that alternative frameworks could produce scattering amplitudes without using the formalism of local fields, and in doing so avoid the complications of field theories. The limitation of this perspective is that the complexities of the physics being described are relegated to a "black box", which shall remain inaccessible.

The S-matrix also relates to spacetime differently from field theories. The path integral perspective of quantum field theory relies on fragmenting a time interval into smaller steps. However, the S-matrix links the initial and final times directly.

¹Renormalization in quantum field theories consists in redefining a model's parameters in such a way that the infinities arising in the theory get "absorbed" away from measurable quantities, which need to be finite. In other words, the constants in a model need to be chosen in ways consistent with empirical values (such as masses) in order to avoid undesirable divergences.

The resulting theory was a particularly good candidate to model strong interactions, at a time when QCD was not yet discovered. The formalism that had been developed for electrodynamic interactions relied heavily on perturbative calculations. Nevertheless, as was detailed in Sections 1.1.1 and 1.1.2, the usability of perturbation theory in QCD is limited. A strong interaction S-matrix deduced from analyticity constraints, if found, could avoid the perturbation problem [32]. It is worth noting that the S-matrix for strong interactions is yet to be determined without relying on results from field theory. The advent of QCD and its empirical success led to the disuse of S-matrix theory, which at times got portrayed as an outdated curiosity of limited applicability. It remains to be seen if some of the more unusual properties of QCD could be clarified with the help of S-matrix theory.

In some areas, however, it has remained extremely useful. It is, for example, part of the basis of string theory. One of Heisenberg's concerns when proposing the framework was that quantum theories would break down at sufficiently small scales. At this stage, perturbative calculations were known to have divergences when integrating up to high momentum. Although his prediction was correct, Heisenberg overestimated the length at which this would occur. The S-matrix as a tool, however, has proven to be useful at the exceedingly small scales (Planck length of the order of 10^{-35} m) that quantum gravity is concerned with, and as such remains popular in the context of string theory [33].

The properties and postulates associated with the S-matrix were mainly based on known properties of existing field theories. One of the goals during the heyday of the theory was to prove that it is self-contained and physical. The framework was considered very abstract, even by the physicists proposing it. Leading contributions in the area included those of Geoffrey Chew, Stanley Mandelstam, Tullio Regge, and Steven Frautschi, among others.

Unitarity is perhaps the most straightforward property of the S-matrix, alongside Lorentz invariance (agreement with special relativity) and linearity. In quantum theories, the unitarity of operators is tied to the necessity of probability conservation. This property will be discussed further in Section 2.2, and has as a result the Optical Theorem, fundamental to the methodology in this work.

An extremely relevant postulate of S-matrix theory is analyticity, the basis of much of the developments in S-matrix theory. S-matrix elements, the scattering amplitudes, need to be analytical functions of the kinematic variables of the problem (generally expressed through Mandelstam variables, detailed in A.2). The postulate is at times referred to as maximal analyticity, as the singularity structure of the amplitudes is expected to include only the singularities required by other postulates, such as unitarity

and crossing [34]. Although it is highly nontrivial to prove that this property is necessary from first principles, it is arguably the most important in the S-matrix framework. The study of the analytical continuation of the S-matrix is, for example, the basis of Regge theory, the focus of the next chapter. The postulate was based on the fact that analyticity is tied to causality in quantum mechanics, and it was also present in perturbative field theory calculations available at the time. The analytical S-matrix will be explored in more depth in Section 2.3.

Another postulate refers to crossing symmetry, previously known in quantum field theories. It relates processes occurring in different channels (see A.2), by exchanging (or crossing) incoming particles with outgoing antiparticles. Knowledge of scattering amplitudes of s-channel gauge boson exchanges, for example, provides information on the related t-channel process as well. Thanks to this property, the S-matrix can simultaneously describe multiple different physical regions in the kinematic variables. This is relevant because, as will be developed in Section 2.3, different channel processes occupy non-overlapping kinematic regions.

Although the principles of Lorentz invariance, unitarity, analyticity and crossing symmetry were enough to obtain a formalism compatible with leading order perturbative calculations, further progress in implementing S-matrix theory required introducing new properties. The bootstrap, for example, states that, if particles get included in one channel (as singularities), it is possible to discover corresponding particles in other channels using unitarity and crossing operations.

Another relevant concept in the theory was nuclear democracy, where the idea of elementary particles was thought to be meaningless, and particles were all a priori bound states of each other. As per Chew [7, 34], this was inspired by Feynman's criteria, suggesting that a correct theory of particle physics should not distinguish between elementary particles, bound states, and resonances. A further consequence of nuclear democracy was that all particles would be associated with a Regge trajectory (see Chapter 3).

Following this general overview of the S-matrix and the goals of its usage, the subsequent sections expand on the mentioned properties and the useful developments that they enabled.

2.2| Unitarity

At its most fundamental level, the unitarity property of the S-matrix can be tied to the conservation of probability attributed to quantum systems. This conservation implies that the total probability of the complete ensemble of states is constant. It is possible to explicitly derive the unitarity requirement of the S-matrix by postulating

this conservation law.

In terms of the S-matrix, the probability of transition between a state $|i\rangle$ and state $|f\rangle$ can be defined as follows:

$$P_{i \rightarrow f} = |\langle f | S | i \rangle|^2 \quad (2.3)$$

In order to impose probability conservation, the sum of probabilities of going to any $|k\rangle$ in an orthogonal basis is expressed as:

$$\sum_k P_{i \rightarrow k} = \sum_k |\langle k | S | i \rangle|^2 \quad (2.4)$$

and set to 1. By rewriting the terms and using the completeness relation for the basis vectors ($\sum_k |k\rangle \langle k| = \mathbb{1}$), the unitarity constraint on the S-matrix can be obtained.

$$\sum_k |\langle k | S | i \rangle|^2 = \sum_k \langle i | S^\dagger | k \rangle \langle k | S | i \rangle = \langle i | S^\dagger S | i \rangle = 1 \quad (2.5)$$

$$\implies \boxed{S^\dagger S = \mathbb{1}} \quad (2.6)$$

Therefore, to fulfill the postulate, the operator needs to be unitary. It is worth noting that, for this relation to hold, it is necessary to include all possible states for the theory of interest. This is consistent with the previously mentioned assumption that the S-matrix relates free-particle states to free-particle states. What this entails is that the interactions considered are short-range. Short-range interactions can be guaranteed by choosing all force-carrying particles to be massive, as the range of interaction is inversely proportional to the carrier mass (per Heisenberg's uncertainty principle). The strong force in particular is mediated by massless gluons. However, confinement implies that its effects are short-range.

One of the central implications of the unitarity constraints on S-Matrix elements is the *optical theorem*. For this work, the theorem is essential, as it provides a straightforward way to calculate observable cross-sections from the approach of Pomeron exchange.

2.2.1| Optical Theorem

The optical theorem states that total scattering cross-sections can be completely determined from the imaginary parts of scattering amplitudes in the forward direction. To visualize how it is obtained from the unitarity relation, it is necessary to establish some preliminary definitions. Firstly, for convenience, the S-matrix can be expressed

2. S-MATRIX FORMALISM

in terms of a transition matrix T in the following way:

$$S = \mathbb{1} + iT. \quad (2.7)$$

This notation allows for the distinction between the scenario where the state of the particles is unchanged (identity) and the nontrivial processes (included in T).

Considering the relation in (2.7) in terms of matrix components as follows

$$S_{if} = \langle f|S|i\rangle = \langle f|i\rangle + i\langle f|T|i\rangle = \delta_{if} + iT_{if}, \quad (2.8)$$

it is possible to extract scattering amplitudes A . These amplitudes constitute the analytical parts of the transition matrix elements. Here δ_{if} is the Kronecker delta. The non-analytical contributions stem from energy-momentum conservation, which must be imposed on the S-matrix in the form of Dirac delta functions. Through this dissection, factors T_{ij} are thus

$$T_{if} = (2\pi)^4 \delta^{(4)}(p_f - p_i) A(i \rightarrow f), \quad (2.9)$$

where the inclusion of $(2\pi)^4$ stems from normalization conventions.

These formulae can be applied to the expression of S-matrix unitarity in Equation (2.6), resulting in:

$$(\mathbb{1} + iT)^\dagger (\mathbb{1} + iT) = \mathbb{1} \implies i(T^\dagger - T) = T^\dagger T. \quad (2.10)$$

Considering this correspondence in terms of matrix elements produces

$$i\langle f|T^\dagger - T|i\rangle = \sum_{\{n\}} \langle f|T^\dagger|n\rangle \langle n|T|i\rangle, \quad (2.11)$$

where a completeness relation has been inserted to represent all possible intermediate states $|n\rangle$. The summation $\sum_{\{n\}}$ includes all quantum numbers and integration in all the intermediate particle momenta.

Then, transition matrix elements, and therefore scattering amplitudes for different processes, must be related as follows:

$$2\text{Im} T_{if} = \sum_{\{n\}} T_{fn}^* T_{ni} \implies 2\text{Im} A(i \rightarrow f) = \sum'_{\{n\}} A^*(f \rightarrow n) A(i \rightarrow n). \quad (2.12)$$

In order to simplify notation, momentum delta functions are implicitly included in the phase space integration contained within $\sum'_{\{n\}}$.

Even though this expression constitutes a very complex set of equations, it can still be convenient to apply. It allows, for example, to obtain amplitudes for processes of perturbation order n through recurrence with amplitudes of lower orders.

The optical theorem stems from a special case of the relations in equation (2.12). Considering elastic processes for two identical particles $1 + 2 \rightarrow 1 + 2$ by choosing $|i\rangle = |f\rangle$ leads to

$$2 \operatorname{Im} A_{el}(s, t = 0) = \sum_{\{n\}} ' A^*(f \rightarrow n) A(i \rightarrow n). \quad (2.13)$$

The elastic amplitude is evaluated in terms of the Mandelstam kinematic variables, where for this particular case $t = 0$. This limit is known as *forward elastic scattering* because the study of the kinematics in the center-of-mass frame shows that $t \propto (1 - \cos\theta)$, where θ is the scattering angle (see Appendix B). It is clear then that $t = 0$ occurs for scattering events in the forward direction ($\theta = 0$).

The remaining step is to interpret the right-hand side of equation (2.13). Recalling the significance of the cross-section, we can relate them to scattering amplitudes. The cross-sections represent the ratio between the outgoing flux of states and the incoming flux of particles. The outgoing flux is given by the scattering amplitudes, and in order to obtain σ_{tot} the amplitudes for all possible outgoing states must be taken into account. For initial flux Φ , this results in

$$\sigma_{tot} = \frac{1}{\Phi} \sum_{\{n\}} ' |A(f \rightarrow n)|^2, \quad (2.14)$$

where the summation is once again made over all possible quantum numbers and regions of Lorentz-invariant phase space.

An invariant expression for the incident flux was proposed by Møller [35]. It is defined as $\Phi = 2E_1 2E_2 |\vec{v}_1 - \vec{v}_2|$ for two incident particles 1 and 2 (in terms of their respective energies and velocities). It is of particular interest to consider the high energy limit, where $s \rightarrow \infty$, and $\Phi \simeq 2s$. Using equation (2.14), it is straightforward to conclude that

$$\sigma_{tot} = \frac{1}{s} \operatorname{Im} A_{el}(s, t = 0) \quad (2.15)$$

when s is large.

In this way, cross-section predictions can be based exclusively on knowledge of one S-matrix element, corresponding to the elastic case. In this thesis, the optical theorem will be applied by considering amplitudes provided by Regge theory.

It is interesting to note that the optical theorem arises in scattering problems in

2. S-MATRIX FORMALISM

several areas of physics, and is not restricted to relativistic scattering. Before it got adopted and named in high-energy physics circles, it was a well-known property in optics [36]. In this context, it can be proven considering plane waves that scatter off some object. However, instead of stemming from quantum unitarity, it is linked to energy conservation. Analogous derivations can also be obtained for the scattering of nonrelativistic quantum mechanical states by a potential, through the conservation of probability currents [23].

2.2.2| Further Implications of Unitarity

Working from elastic scattering contributions can lead to qualitative notions of the behavior unitarity constraints should enforce. It may be interesting to consider, for instance, what happens when scattering deviates from the forward case, but only slightly. From the constraint equation (2.12), the imaginary contributions from different processes are expected to vanish. Assume that, at sufficiently high energies (high number of states $|n\rangle$), the phases for the right-hand terms become randomly distributed. A real right-hand term would require the suppression of imaginary contributions to the amplitudes, and therefore a decrease in cross-sections. As a result, the imaginary parts of amplitudes are expected to have a peak at $t = 0$ and rapidly decrease when t increases or decreases.

This also applies to diffractive processes, where $|i\rangle \simeq |f\rangle$ as well, because quantum numbers are preserved. In fact, the peak at $t = 0$ is expected to govern the behavior of the scattering amplitudes at asymptotically high energy. The result of having a slightly deflected but highly energetic hadron is a phenomenon known as the *leading particle effect*. In a significant fraction of the outcomes, the leading hadron will carry on traveling forward, leaving behind soft (slower) hadrons. In this approach, the focus is on inclusive processes, where there is no interest in observing the complete final state. More precisely, the leading hadron is detected, but the soft particles left behind are treated as an unresolved missing mass.

Since the Pomeron also has a peak in its contribution, Barone and Predazzi [23] propose that the source of the Pomeron could be linked to unitarity relations. However, as the Pomeron could represent a complex state or a complex collection of phenomena, an actual understanding of this relation would require a more exact grasp of the qualitative ideas discussed here.

2.3| Analyticity and Crossing

The second fundamental property postulated for the S-Matrix is analyticity. As was previously mentioned, the requirement is that scattering amplitudes given by the S-matrix will be analytical functions of kinematic variables, where the variables are analytically continued in the complex plane. To recover physical, and therefore real amplitudes, one must take the real limit of the variables.

The analyticity postulate is linked to the concept of *causality*, stating that an output can not precede an input, which quantum field theories are expected to hold. The link with causality can be explicitly established in some areas of physics, such as optics and nonrelativistic quantum mechanics.

2.3.1| Analyticity and Causality: An Example from Optics

One could consider for instance what happens with a wavepacket traveling along the z axis at time τ , as represented by the following equation:

$$A(z, \tau) = \frac{1}{\sqrt{2\pi}} \int_{-\infty}^{\infty} d\omega \alpha(\omega) e^{i\omega(\frac{z}{v} - \tau)}, \quad (2.16)$$

where the packet is assigned velocity v . Inverting this equation gives the amplitude

$$\alpha(\omega) = \frac{1}{\sqrt{2\pi}} \int_{-\infty}^{\infty} d\tau A(0, \tau) e^{i\omega\tau}. \quad (2.17)$$

If the wavepacket scatters off a particle placed at the origin, the resulting wave in the forward direction is

$$G(r, \tau) = \frac{1}{r\sqrt{2\pi}} \int_{-\infty}^{\infty} d\omega f(\omega) \alpha(\omega) e^{i\omega(\frac{z}{v} - \tau)}. \quad (2.18)$$

In this case, the wave travels radially, hence the spatial dependence on propagation radius r . Factor $f(\omega)$ represents the scattering amplitude.

In this situation, it is possible to extend the frequencies ω into the complex plane. It follows that $\alpha(\omega)$ is regular (analytical and single-valued) in the upper half of the complex plane if $A(0, \tau) = 0$ for negative τ . That is, under the imposition that the wave packet does not reach the origin before $\tau = 0$. The convergence of $\alpha(\omega)$ under the restriction for $A(0, \tau)$ is in fact improved by the inclusion of complex ω with positive imaginary parts.

For causality to be obeyed, the scattered wave cannot exist in regions of spacetime

2. S-MATRIX FORMALISM

not permitted by the arrival of the wave packet at $z = 0$. This condition can be expressed as $G(r, \tau) = 0$ for $v\tau - r < 0$. The causality requirement imposes that $f(\omega)\alpha(\omega)$ must be analytic in the upper complex plane. Then, the scattering amplitude $f(\omega)$ must be an analytic function for all ω in this region, except where $\alpha(\omega)$ happens to be zero [32].

This type of approach is common when studying dispersion relations in optics. In the case of quantum fields, the link is less straightforward. This is because, in reality, it is not feasible to impose the localization of the incident wave in such a way as to ensure $A(0, \tau) = 0$ for a well-defined range of time.

In quantum field theory, causality is typically expressed in terms of the commutativity of the fields evaluated at different points in spacetime. When these points have a spacelike separation $(x - x')^2 < 0$, field operators obey:

$$[\phi(x), \phi(x')] = 0 \tag{2.19}$$

This is often referred to as *microcausality*, and is considered less stringent than the more straightforward notion of causality applied in other contexts. This limits the applicability of causality in the determination of dispersion relations for relativistic scattering, and the confidence that can be placed behind these results [23]. However, there is no known rigorous way to prove the link between analyticity and causality without relying on perturbation theory.

Despite this, the study of the analyticity of the S-matrix is fundamental to the study of scattering amplitudes. In fact, through dispersion relations, it is possible to relate the real and imaginary parts of these quantities [37]. It also leads to the crossing property, which allows us to relate processes occurring in different physical regions (different scattering channels, see Figure 2.3).

2.3.2| Analyticity in Relativistic Scattering

A further concept that forms the basis of the study of the analytical properties of scattering amplitudes is *maximal analyticity*. Under this postulate, the singularity structure is restricted to those required by unitarity and crossing. This implies that all the singularities present in the amplitude have a dynamical origin, as will be further developed in this section.

Through unitarity, it is expected that a new singularity will appear every time the threshold allowing for the production of a new particle is crossed. This represents the addition of a right-hand term in equation (2.13). Working from Feynman diagrams helps justify the analyticity postulate, as the singularity structures they provide are consistent with S-matrix theory.

In order to understand this, what follows is an analysis of the analytical properties for the case of two-body processes. For the sake of simplicity, it will be limited to the equal-mass limit. To begin, consider pole-type singularities.

The exchange of particle of mass m represented by a scalar field has the following s-channel Feynman diagram:

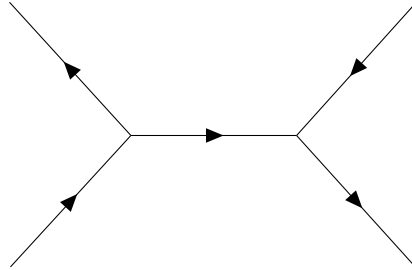


Figure 2.1: Feynman diagram for the s-channel exchange of a scalar.

The propagator for this exchanged particle is of the form

$$\frac{1}{s - m^2 + i\epsilon} \tag{2.20}$$

leading to a singularity at $s = m^2$ in the scattering amplitude $A_s(s, t)$ for the process. The same will occur in channels t and u for $t = m^2$ and $u = m^2$ respectively.

If two or more particles were exchanged instead, the singularities would correspond to branch cuts, starting from $s = (nm)^2$, where n represents the quantity of exchanged scalars. This can be seen by applying the unitarity constraint in equation (2.13) for this particular case. Once again, the singularities in the other channels are analogous. The singularity structure for this example can be visualized in the s -plane in Figure 2.2.

In the center-of-mass frame, the Mandelstam variable s corresponds to the square of the total energy (see Appendix B). Therefore, poles and branch cuts occur at the energy thresholds for the production of particles. In this case, for example, it is not possible to produce two particles of mass m for $s < 4m^2$, that is, before the branch cut. As a result, the addition of a singularity also entails the inclusion of a new possible intermediate term to be summed over in the unitarity relation (2.13).

It is worth noting that the fact that these kinds of singularities are present can be



Figure 2.2: Diagram of the s-channel singularities for the two-body equal-mass example.

2. S-MATRIX FORMALISM

derived in more general terms by studying the unitarity equations. This is beyond the scope of this thesis.

2.3.3| Crossing

As was previously mentioned, the analyticity property will permit us to link the amplitudes of the processes occurring through different channels. This crossing symmetry is a highly relevant concept in quantum field theories. It draws the equivalence between an incoming particle (with momentum p) and an outgoing antiparticle (with momentum $-p$, traveling backward in time).

Applying the crossing operation relates the different channels as follows:

$$A + B \rightarrow C + D \quad (\text{s-channel}) \quad (2.21)$$

$$A + \bar{C} \rightarrow \bar{B} + D \quad (\text{t-channel}) \quad (2.22)$$

$$A + \bar{D} \rightarrow \bar{B} + C \quad (\text{u-channel}) \quad (2.23)$$

Note that the overlined terms represent antiparticles.

Furthermore, the *CPT symmetry*² provides further reactions that can be described from the same amplitude, such as:

$$\bar{C} + \bar{D} \rightarrow \bar{A} + \bar{B} \quad (\text{s-channel}) \quad (2.24)$$

$$B + \bar{D} \rightarrow \bar{A} + C \quad (\text{t-channel}) \quad (2.25)$$

$$B + \bar{C} \rightarrow \bar{A} + D \quad (\text{u-channel}) \quad (2.26)$$

The result of these symmetries is that one function of the invariant Mandelstam variables can be used to describe the distinct regions of kinematic space illustrated in Figure 2.3. This can be realized by simply exchanging the role of each of the variables. Therefore, through knowledge of the singularity structure in one of these regions, one can infer the singularity structure elsewhere. It is worth noting that the regions associated with each of the channels do not overlap. An analytical continuation of, for example, the s -channel amplitude to different domains of s , t , and u is postulated to be possible. This is once again not easily proven for a general S -matrix, but is well justified when restricted to perturbative calculations.

From the previous example, it is possible to see the continuation of the s -channel structure through a well-known property of the Mandelstam variables. Only two of

²CPT symmetry refers to the invariance when conjunctly applying the charge conjugation, time reversal, and parity transformations. It has been observed for all known physical laws.

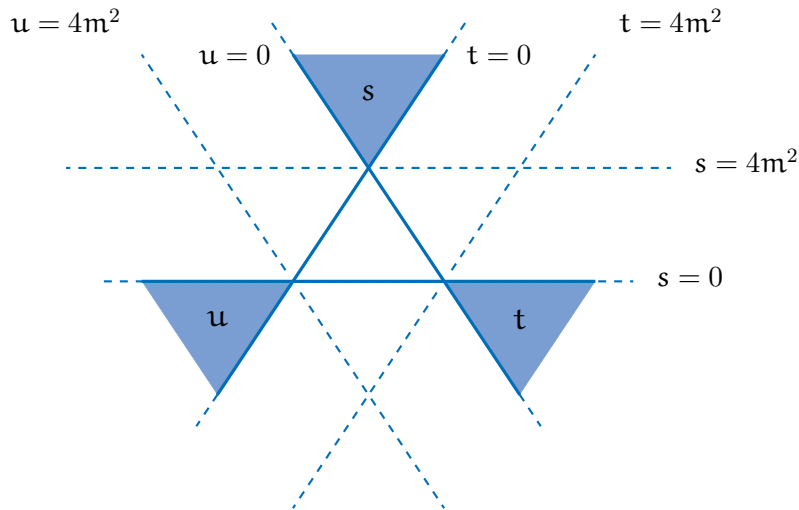


Figure 2.3: Diagram of the three physical regions associated with an equal-mass scattering in the s , t and u channels.

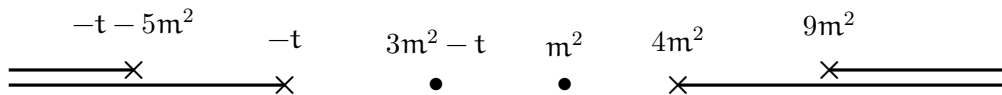


Figure 2.4: Diagram of the scattering amplitude singularities (all channels) for the two-body equal-mass example.

these kinematic invariants are independent, as they obey³ $s+t+u = 4m^2$. By choosing s and t to be independent, and fixing t , the singularities in the u -channel give:

$$u = m^2 \quad \rightarrow \quad s = 3m^2 - t \quad (2.27)$$

$$u = (nm)^2 \quad \rightarrow \quad s = (4 - n^2)m^2 - t. \quad (2.28)$$

This now gives a singularity structure for the amplitude of all processes, as seen diagrammatically in Figure 2.4.

The discussions throughout this chapter provide a general idea of what S-matrix theory says about scattering amplitudes and their mathematical features. The focus of the next chapter will be the study of the singularity structure from the perspective of Regge theory. The analytical continuation applied in this case will lead to the identification of Regge poles (such as the Pomeron) that represent a powerful phenomenological tool.

³When the masses of the particles are chosen to be equal, see Appendix B.

3 Regge Theory

The methodology of Regge theory links the high-energy behavior of scattering amplitudes with a set of resonances referred to as Regge poles [4, 5, 7]. The approach has a long history as a phenomenological success, enabling the study of processes for which theoretical frameworks are nonexistent or scarce. This chapter is centered on the discussion of how these poles arise from the analytic continuation of angular momentum to complex values. For this purpose, it will be necessary to apply the partial wave expansion to write amplitudes in terms of the different angular momentum contributions.

From there, the identified poles can be tied to the phenomenology of diffractive scattering, that this work aims to describe. The behavior of proton-proton and proton-antiproton scattering will then be expressed in terms of the exchange of a particular Regge state, called the Pomeron. Through the optical theorem, it will be possible to see how the properties of the Pomeron exchange can be used to guarantee cross-sections compatible with experiments. Due to empirical observations, the cross-sections have long been known to increase with energy (for energies above 100GeV). The rate of growth must, however, respect the Froissart-Martin bound to ensure unitarity [6, 8]. The implications of this limit for Regge trajectories will be part of the content of this chapter as well.

3.1| Conceptual Overview

The idea of allowing complex values of angular momentum was successfully applied to nonrelativistic scattering by a potential by Tullio Regge, in 1959 [4]. Regge noticed that this treatment provided direct determinations for most potentials from scattering amplitudes, and could be used to generalize dispersion relations to cases with high momentum transfer. In this case, the study of the structure of scattering amplitudes, as mentioned in the previous chapter, is straightforward.

Soon after, Steven Frautschi and Geoffrey Chew saw in Regge's approach a possible key to strong interactions, from the perspective of relativistic S-matrix theory [7]. Here,

if the postulates of unitarity, analyticity and crossing are accepted, it is possible to get highly useful fits of scattering amplitudes by utilizing the same analytical continuation. They posited that all the poles in the S-matrix would correspond to some Regge pole. This aspect of the idea constitutes an application of the maximal analyticity postulate to angular momenta. Clarifying the link between this description and QCD, and thereby relating Regge theory to first principles, could give a fuller picture of strong interactions.

Working from the properties of the S-matrix, the next sections will show that relativistic scattering amplitudes $A(\ell, t)$ will have simple poles that obey the following relationships:

$$\ell = \alpha(t). \quad (3.1)$$

Here the variable ℓ refers to some physical value in angular momentum space and the functions $\alpha(t)$ are called *Regge trajectories*. They represent families of bound states or resonances, which are exchanged in the t-channel. From each of these trajectories, one can find straightforward contributions to asymptotic scattering amplitudes as functions of energy. These take the following form:

$$A(s, t) \underset{s \rightarrow \infty}{\sim} s^{\alpha(t)} \quad (3.2)$$

Recall that Mandelstam variable s corresponds to the square of the energy in the case of center-of-mass scattering. The t-channel exchange of the trajectory with the largest real part will then determine the behavior of the s-channel scattering amplitude. Then, through the optical theorem, it is possible to write high-energy observables such as the cross-section as a linear combination of powers of s .

In order to elaborate on this summary, the next section introduces the *partial wave expansion* of scattering amplitudes. This will help rewrite amplitudes as summations in angular momentum, to perform the analytical continuation proposed by Regge.

3.2| Partial Wave Expansion

Partial wave expansions can be applied whenever one is working with scattering due to a spherically symmetrical potential. Consider the example of a plane wave $\psi(\vec{r})$ (spinless) in nonrelativistic quantum mechanics, as illustrated in Figure 3.1. The potential $V(\vec{r})$ is assumed to have a finite range, as when working with the S-matrix. The scattering process is described through the following Schrödinger's equation [23]:

$$-\frac{\hbar}{2\mu} \nabla^2 \psi(\vec{r}) + V(\vec{r})\psi(\vec{r}) = E\psi(\vec{r}) \quad (3.3)$$

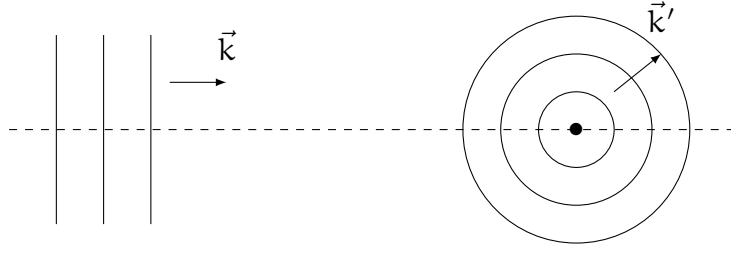


Figure 3.1: Scattering of a plane wave by a spherical potential.

The wavefunction after the scattering occurs is

$$\psi(\vec{r}) \underset{r \rightarrow \infty}{\sim} e^{i\vec{k} \cdot \vec{r}} + f(\vec{k}, \vec{k}') \frac{e^{ikr}}{r}, \quad (3.4)$$

where \vec{k} and \vec{k}' are the incoming and outgoing wavevectors. Factor $f(\vec{k}, \vec{k}')$ is the scattering amplitude and contains the dependence of the solution with the potential.

Due to the symmetry of this problem, it makes sense to separate the contributions to the amplitude of each of the angular momenta, as they will be conserved throughout the process [38]. For spinless particles, the angular dependence for angular momentum ℓ is given by a Legendre polynomial P_ℓ . Therefore, the amplitude for the scattering in the center-of-mass frame can be written as a series expansion:

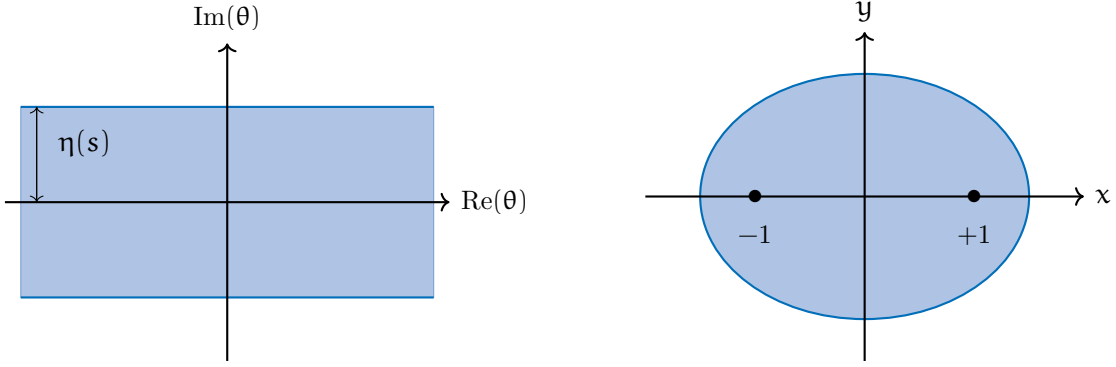
$$f(k, \theta) = \sum_{\ell=0}^{\infty} (2\ell + 1) a_\ell(k) P_\ell(\cos\theta), \quad (3.5)$$

where θ refers to the scattering angle (between \vec{k} and \vec{k}'). Factors $a_\ell(k)$ are partial wave amplitudes. As they contain the information of the interaction (in this case via potential $V(\vec{r})$), they can be expressed in terms of S-matrix eigenvalues S_ℓ [39].

$$a_\ell(k) = \frac{S_\ell(k) - 1}{2ik} \quad (3.6)$$

3.3| Domains of Amplitude Convergence

Before proceeding to implement the expression in equation (3.5) to obtain the analytical continuation in complex ℓ , it is important to mention the domain of convergence of this expanded amplitude. As was illustrated in the example of Section 2.3.1, understanding the mathematical properties of the amplitudes is fundamental to applying analytical continuations, and to the study of the singularity structures. An



(a) Domain of convergence in the complex θ plane.

(b) Domain of convergence in the complex $\cos \theta$ plane (Lehmann ellipse).

Figure 3.2: Illustrations of convergence when allowing complex values of $\cos \theta$.

amplitude in the s -channel will have a partial wave expansion:

$$A(s, \theta) = \sum_{\ell=0}^{\infty} (2\ell + 1) A_{\ell}(s) P_{\ell}(\cos \theta). \quad (3.7)$$

For the sake of simplicity, the analysis will be restricted to the equal-mass two-body scalar case, where $\cos \theta = 1 + \frac{2t}{s-4m^2}$ (see Appendix B). Then, the amplitude is well defined for the s -channel domain, where $s \geq 4m^2$ (see Figure 2.3) [23].

As was mentioned in the previous chapter, the goal of performing an analytical expansion is to describe a greater domain of the kinematic variables through the same amplitude. Having established the convergence for the s -channel, it is then worth exploring if allowing complex values of the Mandelstam variables can advance that objective. For this purpose, consider a complex-valued $\cos \theta$.

As ℓ goes to infinity, the Legendre polynomials tend to $\mathcal{O}(e^{\ell |\text{Im} \theta|})$ [23]. Because of this, ensuring the convergence of the scattering amplitude in this limit requires the partial amplitudes to behave as $A_{\ell}(s) \sim e^{\ell \eta(s)}$. The function $\eta(s)$ imposes the restriction in the complex- θ plane, given by $|\text{Im} \theta| \leq \eta(s)$. The domain is represented in the complex plane in Figure 3.2a.

To visualize whether an expansion of the domain of convergence has been achieved, it is convenient to think of this domain in the complex $\cos \theta$ plane. Consider $\cos \theta \equiv x + iy$. Initially, when the variable is real, the domain of convergence in the s -channel corresponds to $-1 \leq \cos \theta \leq 1$. After the introduction of complex values, the domain in terms of $\cos \theta$ will be given by an ellipse with foci at ± 1 , known as the Lehmann ellipse. The ellipse has axes that depend on $\eta(s)$, and is defined by the following

3. REGGE THEORY

equation:

$$\frac{x^2}{\chi^2} + \frac{y^2}{\chi^2 - 1} = 1, \quad \text{with } \chi = \cosh \eta(s). \quad (3.8)$$

The domain of convergence given by this ellipse (as shown in Figure 3.2b) is larger than the physical domain. However, this continuation still does not allow access to amplitudes for arbitrarily large values of $\cos \theta$. In terms of the Mandelstam invariants, at a given value of s , it will not be possible to obtain a well-defined amplitude for all t or u [23]. Therefore, this extension of the domain is not useful to the goal of obtaining a scattering amplitude for all channels.

The next subsection will show that the Regge approach to analytical continuation will in effect be able to provide the desired outcome.

3.3.1| Continuation to Complex Angular Momenta

To understand the effect of complex momenta on amplitude convergence, it is useful to consider the example where ℓ is chosen to be purely imaginary. In this case, the analogous procedure can be applied to determine that asymptotic convergence is guaranteed for:

$$A_{|\ell|} \underset{\ell \rightarrow i\infty}{\sim} e^{-|\ell|\delta(s)}. \quad (3.9)$$

Now the domain of convergence is given by $\delta(s) \geq |\text{Re } \theta|$. That is, instead of a horizontal strip domain in the complex θ plane as in Figure 3.2a, the domain is a vertical strip. Now, using $\cos \theta \equiv x + iy$ and $\cos \xi = \delta(s)$ it is possible to conclude that the domain of convergence in the xy plane is described by the hyperbola

$$\frac{x^2}{\xi^2} - \frac{y^2}{1 - \xi^2} = 1. \quad (3.10)$$

From this new domain, which is shown in Figure 3.3, it is possible to get two key takeaways. The first and most important one is that, due to the hyperbola being an open domain, the issue of being unable to generalize scattering amplitudes at large $|t|$ or $|u|$ is no longer present. The image also shows that the expansion to imaginary momenta produces a convergence domain that overlaps with the Lehmann ellipse obtained in the previous analysis. Therefore, the new expansion can represent the same scattering amplitudes in the extended domain [23].

3.4| Analytical Continuation for All Channels

Having shown that the consideration of imaginary momenta is indeed a viable approach to the analytical continuation of amplitudes to all channels, what follows is

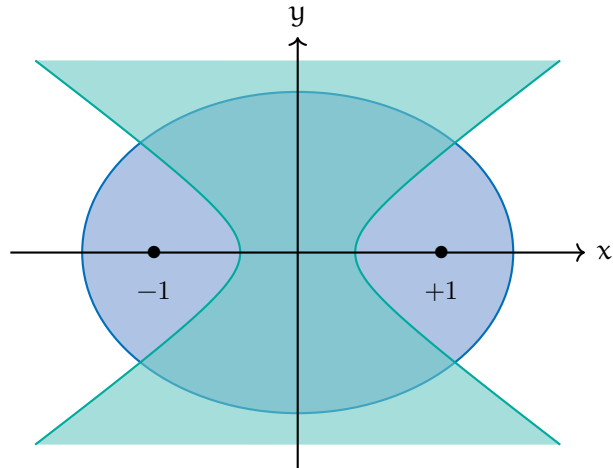


Figure 3.3: Domain of convergence hyperbola for imaginary ℓ in the complex $\cos \theta$ plane (with Lehmann ellipse).

a detailed discussion of that process.

Chapter 2 dealt with the properties of the S-matrix and some of their consequences on the scattering amplitudes. When performing an analytical continuation (by allowing kinematic variables to be complex) one expects to obtain unique representations of amplitudes. Satisfying this requirement calls for the examination of the properties of the scattering amplitudes. This can be done in the context of a uniqueness theorem owing to Carlson.

Carlson's theorem states that analytic functions displaying fast growth at infinity cannot coincide when evaluated at integers [40, 41]. In the case of amplitudes, it means only one analytic function will reduce to the correct partial amplitudes for physical ℓ 's. This is guaranteed for complex-momenta amplitudes $A(\ell, s)$ that verify that:

- a. The singularities are *isolated* in the complex- ℓ plane. This property allows the use of the residue theorem.
- b. The function is *holomorphic* (and therefore analytic) for $\text{Re } \ell \geq L$, for some arbitrary quantity L . This is a requirement from Carlson's theorem.
- c. At infinity $A(\ell, s) \xrightarrow{\ell \rightarrow \infty} 0$, in the right half of the ℓ -complex plane. Carlson's theorem applies to functions bounded by an exponential in this limit.

A scattering amplitude satisfying these conditions is compatible with the relativistic S-matrix formalism, provided it obeys particular dispersion relations [23].

Assume a function $A(\ell, s)$ which satisfies these properties, and is therefore unique.

3. REGGE THEORY

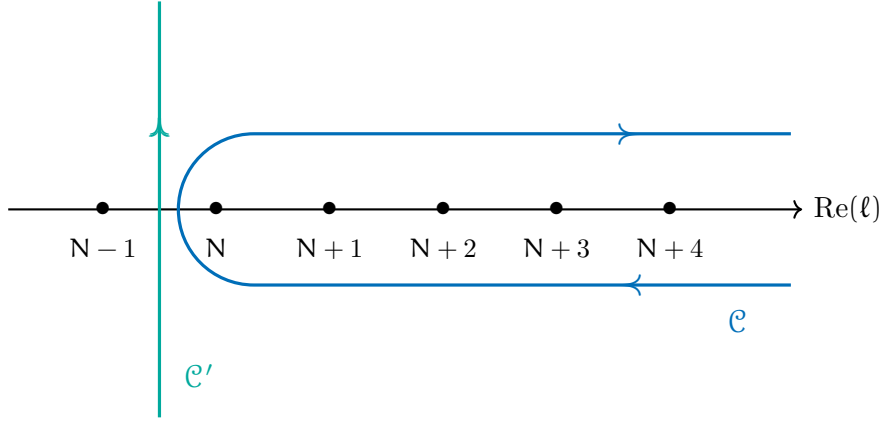


Figure 3.4: Integration contours for scattering amplitudes in the Watson-Sommerfeld representation.

The partial wave expansion from (3.7) can be rewritten using the residue theorem as:

$$\begin{aligned}
 A(s, \theta) &= \sum_{\ell=0}^{N-1} (2\ell + 1) A_{\ell}(s) P_{\ell}(\cos\theta) \\
 &\quad - \frac{1}{2i} \int_{\mathcal{C}} (2\ell + 1) A(\ell, s) \frac{P_{\ell}(-\cos\theta)}{\sin \pi\ell} d\ell.
 \end{aligned} \tag{3.11}$$

In the expression, N represents the lowest integer satisfying $N > L$, and \mathcal{C} is the contour surrounding the poles at $|\operatorname{Re} \ell| \geq L$ (Figure 3.4). This essentially separates the contribution of the holomorphic and nonholomorphic regions and introduces poles at physical values of angular momentum for $\operatorname{Re} \ell \geq L$. The introduction of the poles due to the factor $\sin \pi\ell$ does not modify the relationship between the amplitude $A(s, \theta)$ and the physical amplitudes $A_{\ell}(s)$ given for integer ℓ .

The integral can be performed by deforming contour \mathcal{C} into a straight contour \mathcal{C}' going to infinity, as is also shown in Figure 3.4. This new contour is closed at infinity by a semicircle. Due to property c. of $A(\ell, s)$ and the asymptotic behavior of Legendre polynomials, the semicircular path does not contribute to the integral. So, equation (3.11) is rewritten as

$$\begin{aligned}
 A(s, \theta) &= \sum_{\ell=0}^{N-1} (2\ell + 1) A_{\ell}(s) P_{\ell}(\cos\theta) \\
 &\quad - \frac{1}{2i} \int_{a-i\infty}^{a+i\infty} (2\ell + 1) A(\ell, s) \frac{P_{\ell}(-\cos\theta)}{\sin \pi\ell} d\ell.
 \end{aligned} \tag{3.12}$$

Here the contour $\mathcal{C}' = (a - i\infty, a + i\infty)$, as it represents a vertical line in the complex- ℓ

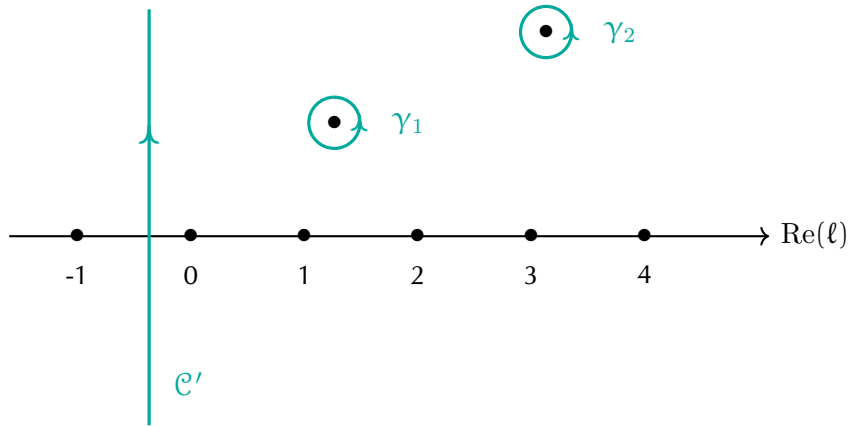


Figure 3.5: Deformed contours for scattering amplitudes in the Watson-Sommerfeld representation.

plane¹.

With the goal of representing the amplitude in terms of its singularity structure, consider what happens when the contour is moved towards lower values of $\text{Re } \ell$. The integral gets contributions from the residues of the singularities of $A(\ell, s)$, which now lie to the right of the contour, as shown in Figure 3.5. There will also be other poles present due to the $1/\sin \pi \ell$ factor introduced in the previous step. Taking the contour down to include singularities for all real and positive ℓ gives the *Watson-Sommerfeld Representation* [42, 43]:

$$\begin{aligned}
 A(s, \theta) = & \sum_i (2\alpha_i(s) + 1) \beta_i(s) \frac{P_{\alpha_i}(-\cos\theta)}{\sin \pi \alpha_i} \\
 & - \frac{1}{2i} \int_{c-i\infty}^{c+i\infty} (2\ell + 1) A(\ell, s) \frac{P_\ell(-\cos\theta)}{\sin \pi \ell} d\ell.
 \end{aligned} \tag{3.13}$$

Functions $\alpha_i(s)$ represent the poles in the amplitude, while factors $\beta_i(s)$ are the residues associated with each pole. The variable c in the integration limits is valued according with $-\frac{1}{2} \leq \text{Re } c < 0$. This corresponds to going down to $-\frac{1}{2} \leq \text{Re } \ell < 0$. The integration contour after this process is illustrated in Figure 3.5.

This tool had a rich history before being applied to scattering by a potential. The implementation for this particular problem was developed by Regge [4]. The domain of convergence is once again given by studying the third property of amplitude, and from the asymptotic properties of the Legendre polynomials. The resulting amplitude is well-defined in a larger domain than the Lehmann ellipse. It also describes regions not covered by the hyperbola of Figure 3.3.

¹Note that a must obey $\text{Re } a \geq L$.

3. REGGE THEORY

Having arrived at the result in equation (3.13), it is possible to identify what is known as *Regge poles*, which will be crucial to this thesis. The functions $\alpha_i(s)$ give the locations (in the complex plane) of the Regge poles, which were obtained through the analytical continuation procedure. Regge poles are commonly referred to as trajectories, as the positions given by α_i depend on the energy. Further sections will cover in more detail how these poles and residues can be expressed, and also utilized to obtain scattering amplitudes through parametrization.

3.4.1| Asymptotic Behavior in the Watson-Sommerfeld Representation

As was mentioned previously, it is of particular interest to obtain analytical amplitudes that contain the information for multiple scattering channels. Due to that, the Watson-Sommerfeld representation should be tested at high values of the Mandelstam variables.

Consider the Watson-Sommerfeld result in the limit of large t (at fixed s). Recalling that $\cos \theta = 1 + \frac{2t}{s-4m^2}$, this is equivalent to allowing the cosine to take large values. In this limit, the properties of the Legendre polynomials indicate that, provided $\text{Re } \ell > 1/2$ [44]:

$$P_\ell \sim (\cos \theta)^\ell. \quad (3.14)$$

When evaluating the integral in (3.13), its contribution to the amplitude will be asymptotically insignificant.

In the limit, the amplitude simplifies to:

$$A(s, \theta) \simeq - \sum_i \beta_i(s) \frac{(-z)^{\alpha_i(s)}}{\sin \pi \alpha_i(s)}, \quad (3.15)$$

where some factors have been absorbed into $\beta_i(s)$. This series will be dominated by the pole with the largest real value in α_i , located furthest to the right in the complex- ℓ plane. The behavior of the scattering amplitude can be simplified further, giving:

$$A(s, t) \underset{t \rightarrow \infty}{\sim} -\beta(s) \frac{t^{\alpha(s)}}{\sin \pi \alpha(s)}, \quad (3.16)$$

where $\alpha(s)$ is the leading Regge pole, and $\beta(s)$ its corresponding residue as utilized in the previous equation. It is worth noting that taking into account other types of singularity, such as cuts, will provide corrections to this result. However, this thesis will not provide further discussion of these contributions.

If, instead, one is interested in high- s scattering amplitudes, due to the crossing

property, the result is analogous:

$$A(s, t) \underset{s \rightarrow \infty}{\sim} -\beta_i(t) \frac{s^{\alpha_i(t)}}{\sin \pi \alpha_i(t)}. \quad (3.17)$$

This work will use t-channel Regge poles, as the focus will be on high energy (i.e. large s) scattering amplitudes. This is because the increase of the amplitude with s could lead to the violation of unitarity, as will be shown in Section 3.5.1. The behavior of diffractive processes at high energy will be dominated by the Regge pole known as the Pomeron.

Recalling the discussions of energy scales in the first chapter, it is worth pointing out that, although Regge theory is applicable in the high energy limit, it does not necessarily mean it is easily linked to perturbative QCD. Although results from Regge theory can, in some cases, be interpreted from perturbative gauge theory, the interest in the theory lies in its description of diffractive processes. These soft interactions have significant contributions to high-energy hadronic scattering, but, as was explained in Section 1.3, also involve non-perturbative scales.

In the Regge limit, this section showed that complex angular momenta enable the determination of scattering amplitudes in terms of its poles. Due to this, the concept of Regge poles was embraced by proponents of S-matrix theory. See for example the discussion that took place in 1967, based on a talk by Chew [45].

3.4.2| Signatures of Regge Poles

The previous section mentioned that the crossing property could be applied to write the asymptotic amplitude with Regge poles for a different channel. Although the result obtained from the s-channel can indeed be translated to the t-channel, it leads to complications. When studying relativistic scattering, the crossing procedure introduces divergences in the amplitudes. The issue can be resolved by distinguishing between *even* and *odd* contributions. This is the general idea behind the *signature*, a quantum number whose *raison d'être* is the resolution of these divergences.

Consider what happens when exchanging the contributions from channels s and u . Using that $u(-z_t, t) = s(z_t, t)$ for $z_t = \cos \theta_t = 1 + \frac{2s}{t-4m^2}$ (see Appendix B) [23], this is equivalent to taking $z_t \rightarrow -z_t$. Through properties of the Legendre polynomials, these factors transform as $P_\ell(-z_t) = (-1)^\ell P_\ell(z_t)$. The issue with the presence of factors $(-1)^\ell$ is that it is incompatible with property c. of the analytical amplitudes in Section 3.4 ($A(\ell, s) \xrightarrow{\ell \rightarrow \infty} 0$) [46]. Recall that this property guaranteed the uniqueness of the function through Carlson's theorem.

In the context of nonrelativistic mechanics, divergent terms only appear when there

3. REGGE THEORY

are exchange terms in the potentials². However, in relativistic scattering, a potential is always expected to allow exchanges. These manifest as discontinuities of the scattering amplitudes. The issue can be circumvented by considering two distinct analytical functions. Each of the functions will contain only odd or even contributions to the partial wave amplitudes A_ℓ^ξ . The partial amplitudes can be expressed as³:

$$A_\ell(t) = \frac{1}{2} \sum_{\xi=\pm 1} (1 + \xi e^{-i\pi\ell}) A_\ell^\xi. \quad (3.18)$$

The summation index ξ represents the signature quantum number. It can take values $+1$ for a positive signature (even ℓ) and -1 for a negative signature (odd ℓ). Now each of the partial amplitudes (even and odd) is analytical, well-behaved at large angular momenta, and uniquely determined.

Repeating the Watson-Sommerfeld representation procedure for each of these amplitudes leads to

$$A(z_t) \underset{|z_t| \rightarrow \infty}{\simeq} - \sum_{\xi=\pm 1} \sum_{i_\xi} \beta_{i_\xi}(t) \frac{1 + \xi e^{-i\pi\alpha_{i_\xi}(t)}}{\sin \pi\alpha_{i_\xi}(t)} (-z_t)^{\alpha_{i_\xi}(t)}. \quad (3.19)$$

In relation to the previous result in equation (3.15), the separation of the amplitudes through the definition of A_ℓ^ξ simply introduces factors $(1 + \xi e^{-i\pi\alpha_{i_\xi}(t)})$. After this, calculating amplitudes requires the classification of Regge poles according to their signature.

Taking $s \rightarrow \infty$ and keeping only the contribution of the leading pole, the amplitude can be written as:

$$A(s, t) \underset{s \rightarrow \infty}{\sim} -\beta(t) \frac{1 + \xi e^{i\alpha(t)}}{\sin \pi\alpha(t)} t^{\alpha(s)}, \quad (3.20)$$

when working with t-channel singularities. The analogous result will be valid for s-channel singularities at high t .

3.5| Regge Poles

So far, this work has not explored the meaning of the Regge poles. In terms of Regge poles, when $\ell \rightarrow \alpha(t)$, partial wave amplitudes behave as

$$A(\ell, t) \sim \frac{\beta(t)}{\ell - \alpha(t)}. \quad (3.21)$$

²An exchange term obeys $\hat{V}\psi(x) = V(x)\psi(-x)$.

³ $e^{-i\pi\ell} = (-1)^\ell$ if ℓ is an integer.

The pole $\alpha(t)$ in reality represents a trajectory in kinematic space. For positive values of t (in the nonphysical region for the s -channel), the poles represent resonances and bound states, with different possible values of ℓ . Function $\alpha(t)$ is called a trajectory because it interpolates between these states. The amplitudes obtained from a Regge pole can be interpreted as an exchange of a family of resonances, as linked by this trajectory. Note that the asymptotic behavior for the s -channel is in fact given by exchanges in the t -channel, and vice versa. The overall exchanged state is often referred to as a *Reggeon*.

As was explained in the previous section, resonances in the ℓ plane will be either even or odd. A trajectory with a positive signature will interpolate resonances with even angular momentum, and one with a negative signature will interpolate resonances with odd angular momentum. Different processes may involve different trajectories depending on the quantum numbers that participate in the process.

An interesting quality of Regge trajectories is that the small- t expansion

$$\alpha(t) = \alpha_0 + \alpha' t \quad (3.22)$$

can actually be generalized to relatively high values of t whenever the resonances being interpolated possess the same quantum numbers [23]. In this thesis, the amplitudes of interest will be evaluated in the forward direction (per the optical theorem). Therefore the use of linear trajectories in t (with minor corrections) is well justified. The intercept α_0 and the slope α' (for each trajectory considered) will be some of the parameters obtained in the determinations of cross-sections.

It is often convenient to express one-Reggeon amplitudes as

$$A(s, t) = \beta(t)\eta(t)s^{\alpha(t)}, \quad (3.23)$$

where η is the signature factor. The factor takes the following values:

$$\eta(t) = -\frac{e^{-i\frac{\pi}{2}\alpha(t)}}{\sin \frac{\pi}{2}\alpha(t)} \quad \text{for } \xi = 1 \quad (3.24)$$

$$\eta(t) = -i\frac{e^{-i\frac{\pi}{2}\alpha(t)}}{\cos \frac{\pi}{2}\alpha(t)} \quad \text{for } \xi = -1 \quad (3.25)$$

For small t (linear trajectories) this simplifies to:

$$\eta(t) = \eta(0)e^{-i\frac{\pi}{2}\alpha(t)}. \quad (3.26)$$

This notation will be applied throughout the remainder of this thesis.

3. REGGE THEORY

3.5.1| The Pomeron

As was discussed previously, the main Regge trajectory of interest in this work is the Pomeron. Contrary to other leading trajectories which tend to have intercepts near 0.5, the Pomeron is typically found to have an intercept slightly greater than 1 when using Regge theory to fit experimental data [23]. The behavior of secondary trajectories is discussed in more detail in Chapter 5.

Reggeon intercepts regulate the growth of amplitudes with energy (\sqrt{s} in the center-of-mass frame). Intercepts greater than one can lead to unitarity violations⁴. The Froissart-Martin bound is a theorem derived from S-matrix analyticity and unitarity properties [6,8]. It shows the restrictions on the asymptotic growth rate of cross-sections with energy. The total cross-sections cannot grow faster than $\ln^2 s$, as expressed by:

$$\sigma_{\text{tot}} \leq C \ln^2 s \quad \text{as } s \rightarrow \infty, \quad (3.27)$$

where C is some constant. In hadronic scattering the value of C is given by the pion mass, as this is the lightest particle that can be exchanged in the t channel [46,48].

From the optical theorem and (3.23), the contribution of a Reggeon to the cross-section takes the following form:

$$\sigma_{\text{tot}} \underset{s \rightarrow \infty}{\simeq} s^{\alpha(0)-1}. \quad (3.28)$$

At the asymptotic limit, this means trajectories with $\alpha(0) \leq 1$ will satisfy the bound.

It is natural then to wonder why the Pomeron is so important to the description of hadronic processes, given its apparent conflict with unitarity. The Pomeron was postulated in the 60s, in response to cross-sections that were expected to be asymptotically constant. As introduced by Chew, Frautschi, and Gribov, the trajectory had intercept 1, saturating the unitarity bound [5, 7].

This state was named after Isaak Pomeranchuk because it makes sure that the cross-sections obey certain conditions he postulated. The Pomeranchuk theorem states that the cross-sections for particle-particle and particle-antiparticle processes will be asymptotically equal (at $s \rightarrow \infty$). Due to this theorem, the Pomeron is expected to have the quantum numbers of the vacuum. As proposed, the Pomeron was theorized to dominate all diffraction peaks [7].

As experimental data for hadronic scattering came to light, cross-sections were found to increase logarithmically at high energy. Attempts to reflect this behavior led to the wide implementation of the supercritical Pomeron with a slightly larger

⁴This is also true for exchanged particles of spin greater or equal to 2. However, this can be resolved through a process known as *Reggeization* [47].

intercept [47]. This is also referred to as the *soft Pomeron*, as it is essential to the description of hadronic diffraction. The unitarity violations that may arise require careful consideration, but do not negate the usefulness of the supercritical Pomeron. Some aspects worth highlighting are that:

- Pomeron unitarity violations could occur at energies beyond what is observable now or in the near future [23, 46].
- The rate of growth of the cross-sections could be reduced by taking into account the exchange of multiple Pomerons. This is equivalent to including Regge cuts in the formulation of amplitudes [23, 46].
- It is possible to ensure unitarity through the Eikonal and U-matrix schemes, as will be shown in Chapter 4. This is the methodology of interest in this work.

The discussion in Chapter 1 stated that hadronic processes are dominated by strong interactions. Therefore, there should be a way to describe them in the language of QCD. The discussion of the Pomeron so far has been fairly abstract, and somewhat disconnected from the Lagrangian approach to quantum field theory. This is one of the challenges in Regge theory, it is not clear how it fits within such a well-verified and first-principle-rooted theory as QCD. However, in the case of perturbative interactions, there exists a *hard Pomeron* formalism. This approach is based on BFKL (Balitsky, Fadin, Kuraev, Lipatov) theory, which aimed to link the Pomeron with the building blocks of QCD (quarks and gluons) [49–53]. Despite this, the relationship between the soft and hard Pomeron is not fully understood.

A difficulty in studying the Pomeron is that measurements of states with vacuum-like properties are not trivial. Contrary to other Regge trajectories the Pomeron does not interpolate the typical resonances studied in particle physics. According to BFKL theory, it is expected, instead, to interpolate hypothetical bound states of gluons, known as *glueballs*. In other words, the exchange of a Pomeron should be equivalent to a complicated exchange of an even number of gluons. This perspective is compatible with perturbative QCD in hard processes [54–56].

3.5.2| The Odderon

The Pomeron has an odd signature counterpart known as the Odderon. It was proposed by Łukaszuk and Nicolescu in the early 70s [57], but the evidence to support its existence was hard to obtain. At sufficiently high energy, it is expected to explain the differences between proton-proton and proton-antiproton scattering amplitudes.

Recently, there has been renewed interest in this resonance. The behavior of proton scattering that has been registered by the TOTEM experiment has provided evidence

of Odderon contributions. This was announced by CERN in 2021, based on the work in [9] and [10]. In terms of QCD, the Odderon corresponds to a bound state of an odd number of quarks. It is typically associated with a three-gluon glueball.

The detection of this state and the current availability of 13 TeV proton collision data led to the consideration of the Odderon in the analysis that will be presented here.

3.6| Some Open Questions in Regge Theory

As was explained throughout this chapter, Regge theory is a very powerful tool in the description of soft (quasi-forward region) hadronic scattering, where working from the QCD Lagrangian is not possible. It is worth mentioning some of the gaps that still remain in Regge theory.

- The dynamical origins of the mathematical description Regge theory provides are unclear.
- Although from a perturbative point of view the Pomeron and Odderon are thought to interpolate *glueballs*, these are only postulated particles. This means that the diffractive descriptions from Reggeons are dominated by trajectories interpolating bound states that have not been linked to observed particles. This is not the case for some secondary trajectories, which are tied to known mesons and baryons.
- The relationship between the soft Pomeron and the hard Pomeron is unclear. It is not known, for example, if they are distinct, or if there is some transition between them, given by the change in energy scale.
- The inclusion of higher-order corrections affects the magnitude of the resulting soft Pomeron intercept, making it deviate from values obtained by relying on simpler fits. This aspect relates to the motivations of this work, where different unitarity corrections are expected to approximate some set of multi-Reggeon exchanges (see Chapter 4).
- Having found evidence for Odderon contributions at the LHC, the door is open to learn more about its characteristics. Some questions to answer are what the Odderon intercept should be, and if a distinction needs to be made between a soft and a hard Odderon.
- There is still open discussion over to what extent a hard Pomeron contribution is present in elastic scattering.

- Further experimental measurements for higher energies will show whether the Pomeron model still provides an adequate description of data.

To summarize, this chapter showed how S-matrix theory and the analysis of scattering amplitudes lead to the Regge formulation. Through Reggeon contributions dominated by the Pomeron, it will be possible to obtain predictions for hadronic cross-sections. However, the Pomeron model can display unitarity violations, which should be handled with appropriate care. The following chapter will introduce the unitarization methods that this thesis aims to compare in view of new empirical evidence.

4 Unitarization Schemes

Chapter 3 explained how the Pomeron approach to diffractive scattering could lead to unitarity issues. However, the possible violation of the property is not insurmountable. The present chapter will delve into the unitarization schemes that will be applied in this work to restore unitarity.

Before explaining the details of unitarization, it is merited to discuss why it is worth focusing on this approach. As was mentioned before, many have argued that unitarity violations are not even relevant at experimentally accessible energies. However, even harkening back to the Tevatron era¹, there has been work suggesting that unitarity violations could already be present at the available energies [58–61]. For example, in [58], it is shown that although unitarity is guaranteed at presently available energies for integrated quantities, such as cross-sections, it is violated when looking at amplitudes in impact parameter space. The impact parameter space description of amplitudes will be discussed in the next section.

It is not straightforward to determine the cutoff energy where unitarity is no longer assured by the Pomeron model. As the property needs to be fulfilled regardless, it makes sense to impose it from the beginning when calculating amplitudes.

Likewise, the inclusion of cuts has been shown to “tame” the rise of the amplitudes with energy, as well as correct other behaviors in pole-only models [23, 38, 46]. It is possible in fact to calculate the form that cut contributions to amplitudes take. The issue underlying this approach is that cut Regge theory is not as well understood as the pole contributions. Separating the observed effects of the poles from those of the cuts can also be a challenge, even in the perturbative case [62].

Another aspect to note is that as $|t|$ grows, the dependence of the amplitudes with energy becomes increasingly complicated. Then, at sufficiently high $|t|$, perturbative QCD can be applied [23, 38]. This negates the need for Regge theory in the high $|t|$ kinematic region, as there is already a fundamental and well-verified theory that can be used.

¹The Tevatron was a synchrotron experiment that ran from 1983 to 2011 at Fermilab. The accelerator produced beams of up to 1 TeV of energy. It was succeeded by the LHC experiment at CERN, where proton beams have been accelerated up to 6.8 TeV.

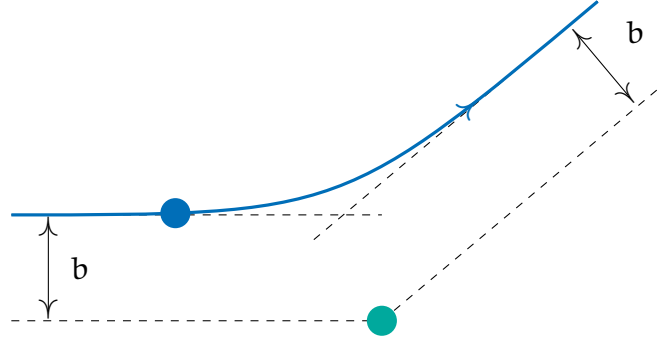


Figure 4.1: Illustration showing impact parameter b in a particle collision event.

As the rest of the chapter will show, the unitarization schemes can be thought of in terms of the inclusion of multiple pole exchanges. In this sense, the unitarization schemes do not necessarily represent a rejection of the cut-based restoration of unitarity. The unitarization procedures in fact constitute approximate incorporations of more complex Reggeon-mediated diagrams. As such, they are also a tool to generalize amplitude calculations to high- $|t|$, away from the elastic case [63].

4.1| Unitarity in the Impact Parameter Representation

To obtain the unitarization schemes, it is necessary to consider unitarity relations in the impact parameter space. The introduced parameter b of particle collision represents the perpendicular distance between the path of the incoming particle and the center of the scatterer, as shown in Figure 4.1.

As an overview, through the unitarization schemes, it will be possible to write unitarized amplitudes in terms of functions $\chi(s, b)$. These functions will be defined from the Regge scattering amplitudes, led by the Pomeron exchange. Then, unitarized cross-sections can be expressed as:

$$\sigma_{\text{tot}} = 4\pi \text{Im} \int_0^{\infty} db \, b \, F(\chi(s, b)), \quad (4.1)$$

where function $G(\chi(s, b))$ will vary according to the chosen scheme [64].

To understand the process in detail, recall the unitarity equation (2.13). It is possible to translate this relation by taking the amplitudes into the impact parameter space. Using a Fourier-Bessel transform one can define:

$$H(s, b) = \frac{1}{8\pi s} \int_0^{\infty} dq \, q \, J_0(b\sqrt{-t}) A_{\text{el}}(s, t), \quad (4.2)$$

where J_0 refers to the Bessel function of the first kind. Variable q represents the

momentum transferred in the process. The definitions of the Mandelstam variables in Appendix A.2 give $t = -q^2$.

This approach to rewriting amplitudes has been well studied, and the interpretation of quantity b as an impact parameter has been established. See for example [65]. The relation is exact and can be applied at all energies. One of the benefits of its implementation is that writing amplitudes in terms of the invariant momentum transfer in t is more natural for relativistic scattering than the dependence on angles used in partial wave expansion.

The transformed unitarity equation then results in

$$\text{Im } H(s, b) = |H(s, b)|^2 + G_{\text{in}}(s, b). \quad (4.3)$$

The term $G_{\text{in}}(s, b)$ represents the contributions of all inelastic processes to the intermediate states summed over in (2.13), and is called the *inelastic overlap function*. This is where most of the unknowns in the theory are contained.

The impact parameter unitarity constraint has more than one possible solution ($H(s, b)$ satisfying Equation (4.3)). The following sections will discuss the solutions corresponding to the Eikonal approximation and the U-matrix.

4.2| The Eikonal and the U-matrix

Unitarity equation (4.3) imposes restrictions over function $H(s, b)$, representing inelastic contributions in impact parameter space. The inelastic contribution in G_{in} is taken to be bounded by $G_{\text{in}}(s, b) \geq 0$, and the following relation stems from unitarity [66, 67]:

$$0 \leq |H(s, b)|^2 \leq \text{Im } H(s, b) \leq 1. \quad (4.4)$$

Therefore the inelastic overlap function must obey $0 \leq G_{\text{in}}(s, b) \leq 1$. There is a straightforward interpretation of this. When $G_{\text{in}}(s, b) = 0$ the elastic processes dominate. However, when $G_{\text{in}}(s, b) = 1$ there is full absorption [24]. Recall that $|H(s, b)|^2$ is the elastic counterpart of $G_{\text{in}}(s, b)$ and as such presents the complementary behavior.

The two solutions to the unitarity equation are given by:

$$H(s, b) = \frac{1}{2} \left[1 \pm \sqrt{1 - 4G_{\text{in}}(s, b)} \right]. \quad (4.5)$$

4.2.1| Eikonal Scheme

Taking first the minus sign solution leads to the *eikonal approximation*², where

$$H(s, b) = \frac{i}{2} [1 - e^{-i\chi(s, b)}]. \quad (4.6)$$

The term $\chi(s, b)$ is purely imaginary at the high energy limit $s \rightarrow \infty$ and is known as the *eikonal function*. This is where the information of the processes is included, from the amplitudes that can be calculated in Regge theory. The eikonal is in fact a transformation of this amplitude according to

$$\chi(s, b) = \frac{1}{s} \int_0^\infty q dq J_0(bq) A_{\text{Born}}(s, t). \quad (4.7)$$

Here, the amplitude is taken to be a Born amplitude. In perturbative terms, the Born amplitude represents the simplest exchange processes. In Regge theory, it is calculated from single-Reggeon exchange amplitudes. Considering the inverse of equation (4.2), the eikonalized amplitude can be written in terms of $\chi(s, b)$:

$$A_{\text{eik}}(s, t) = is \int_0^\infty b db J_0(bq) [1 - e^{-i\chi(s, b)}]. \quad (4.8)$$

From there it follows that the eikonalized amplitude includes the Born amplitude at low order, but also includes further contributions. These are expected to take the form $\mathbb{P} + \mathbb{P}\mathbb{P} + \mathbb{P}\mathbb{P}\mathbb{P} + \dots$, representing the multiplicity of exchanged Pomerons \mathbb{P} [67]. Although it is not always viable to calculate higher-order contributions to verify that they coincide with the eikonal approximation, it is still possible to assert that this is what occurs at a phenomenological level [64].

4.2.2| U-matrix Scheme

A second solution corresponds to the U-matrix scheme, and it has the form

$$H(s, b) = \frac{\text{Im} \tilde{\chi}(s, b)}{1 - i\tilde{\chi}(s, b)}. \quad (4.9)$$

²The name eikonal comes from the Greek word for image, as equations of this form can also be obtained when studying optical wave scattering. It can also be obtained in nonrelativistic quantum mechanics. The approximation works in the high-energy limit (when particle energy is significantly greater than the potential).

4. UNITARIZATION SCHEMES

Function $\tilde{\chi}(s, b)$ is analogous in its role to the eikonal function³. The two can be related by $\tilde{\chi}(s, b) = \frac{\chi(s, b)}{2}$. In view of this, the functions required to write eikonized or U-matrix amplitudes are calculated for Regge Poles from essentially the same procedure. The U-matrix-unitarized amplitude is:

$$A_{U\text{-mtx}}(s, t) = is \int_0^\infty b db J_0(bq) \left[\frac{2\tilde{\chi}(s, b)}{1 + \tilde{\chi}(s, b)} \right]. \quad (4.10)$$

As will be detailed in the next section, both schemes are expected to share relevant properties in order to be viable approaches to unitarity. Given that they stem from the same equation, both the eikonal and the U-matrix are widely used to restore unitarity for the supercritical Pomeron. However, their differences become more evident as the energy increases. Therefore, the most recent LHC data could potentially help determine if one of the schemes shows greater agreement with experiments. The study of this possible distinction constitutes the main goal of this thesis.

4.3| Scheme Properties and Differences

To begin the discussion of the unitarization schemes presented it is worth highlighting some fundamental aspects in which they coincide. Firstly it is clear that both unitarization schemes should reduce to the same (Born) scattering amplitude at low energy [64]. At high energy, however, each of the schemes represents the inclusion of different higher-order diagrams. In other words, the unitarization is achieved through different scattering mechanisms. Therefore, eikonal and U-matrix amplitudes should differ at high energy, and in consequence, so should observables such as the cross-section.

Both schemes impose a bound on the amplitudes. The eikonalization procedure enforces the *black disc limit*. The restriction can be expressed as $\text{Im } H(s, b) \leq \frac{1}{2}$. At the asymptote, the saturation of this constraint leads to $\sigma_{el}(s) = \sigma_{in}(s) = \frac{1}{2}\sigma_{tot}(s)$ (equivalently $\frac{\sigma_{el}}{\sigma_{tot}} \rightarrow \frac{1}{2}$) [66]. This represents equal contributions from elastic and absorption processes to the total cross-section. The restriction corresponds to an upper bound in the allowed values of impact parameter b . Hence the possibility of defining a disc in impact parameter space, as mapped onto the unitarity domain by the unitarization process.

In the context of proton scattering, when the black disc limit is reached the proton

³The U-matrix solution for $H(s, b)$ is often expressed, instead of in terms of $\tilde{\chi}$ a function U . This helps in part to explain the name. However, note that $\tilde{\chi}$ is not actually a matrix. Just like in the eikonal case, the name stems from the appearance of equations of this form in other physical contexts. It is also known as the generalized reaction matrix. See for example the derivation in [68].

is said to become black (maximally absorptive). The inelastic term $G_{in}(s, b)$ is also referred to as *shadow profile function*, as the “shadow” produced by summing over all inelastic processes can be thought to “generate” elastic scattering.

On the other hand, with the U-matrix, the behavior for $s \rightarrow \infty$ is $\frac{\sigma_{el}}{\sigma_{tot}} \rightarrow 1$. This means that asymptotically, the elastic contributions to the cross-section should dominate at high energies. From this, it is possible to see that determining that a particular scheme is more compatible with observations leads to different predictions for hadron diffraction.

The use of the U-matrix allows elastic amplitudes to exceed the black disc limit and keep increasing up to the complete unitarity circle. The U-matrix is said to display “anti-shadowing”. In impact parameter space, a proton in this picture has a “grey” center (where absorption and transparency coexist) with a surrounding black ring [64].

It has been shown that eikonalization may, in some cases, allow small asymptotic violations of unitarity for the supercritical Pomeron [69]. This is not expected to affect the results presented in this thesis [67].

The first four chapters have established the theoretical building blocks of the approach implemented in this work for diffractive scattering. The following chapter will refer to the methodology applied to compare the unitarization results for experimental data. It will also detail the technical considerations that were used to obtain those results.

5 Models and Methodology

The goal of this chapter is to delve into the more technical details of this work's approach to unitarity in diffractive scattering. It aims to show how the optical theorem, Regge poles and unitarization schemes come together to make predictions for proton-proton and proton-antiproton collisions. With this in mind, it will be relevant to discuss the observables that will be considered, the datasets used, the Reggeons that were included, the fits that linked the calculations with the experiments, and more.

As an overview, the work consisted of applying a χ^2 minimization fit over the parameters associated with each of the Reggeons. The parameters include, for example, the intercept and slope of the Pomeron, as given by equation (3.22). The amplitudes calculated from Regge theory were unitarized using numerical integration. Then they were used to calculate total cross-sections, differential cross-sections, and the ρ parameter, as will be expanded on in this chapter. The χ^2 method of statistical testing consists of finding a set of parameters for which the theoretical predictions are in satisfactory agreement with experimental data.

The process was realized for data from the TOTEM and ATLAS experiments at the LHC, to allow comparisons to be drawn. It was also possible to compare different criteria in some of the choices that will be outlined in this chapter, such as the inclusion of the Odderon.

5.1| Included Reggeons

Firstly, recall the properties and amplitudes for the Reggeons as given by Regge theory. As equation (3.23) showed, the amplitude contribution of each Reggeon can be written in terms of a signature factor $\eta(t)$, and the Regge pole trajectory $\alpha(t)$. It also includes a factor $\beta(t)$ which contains the residue of the Regge pole and some other absorbed terms.

For the purposes of the fitting procedure, equation (3.23) is further rewritten as

follows:

$$A_i(s, t) = \beta^2(t)\eta(t) \left(\frac{s}{s_0} \right)^{\alpha(t)}, \quad (5.1)$$

This expression for the amplitude is conventionally used when performing the types of calculations presented here. Note that $\beta(t)$ has been redefined through factorization. The constant s_0 is a mass scale and is fixed at 1 GeV^2 .

In order to simplify the dependence on the Regge trajectory, the signature factors are chosen according to the approximation in Covolan et al. [58]. By noticing that the sine and cosine factors in (3.24) and (3.25) will have smaller contributions than the exponential at $t = 0$, it is possible to obtain:

$$\eta_+(t) = -e^{-i\frac{\pi}{2}\alpha_i(t)} \quad (\text{even signature}) \quad (5.2)$$

$$\eta_-(t) = -ie^{-i\frac{\pi}{2}\alpha_i(t)} \quad (\text{odd signature}) \quad (5.3)$$

Recall that the optical theorem, which will be used to calculate cross-sections, takes input amplitudes evaluated in the forward limit. Therefore, the emphasis in the calculations was placed at small $|t|$ throughout the methodology implemented.

5.1.1| Pomeron

As was mentioned previously, the amplitude contributions are dominated by the Pomeron exchange. It is natural then to begin by outlining the details of its inclusion in this work.

- As the Pomeron carries the quantum numbers of the vacuum, its signature will be even.
- The factor $\beta(t)$ represents the proton-Pomeron interaction vertex. These vertices are illustrated in the Pomeron exchange diagram in Figure 5.1. The vertices can be interpreted as a coupling magnitude times a vertex form factor, which reflects the compositeness of these particles (as a function of t). The exact expressions that the form factors should have is not known. However, there are standard ways to model the expected behavior, as will be discussed later in this section.
- The Pomeron trajectory is generally taken to be linear, as shown in equation (3.22). As the calculations focus on the supercritical Pomeron ($\alpha_0 \geq 1$), the intercept α_0 is expressed as $1 + \epsilon$. The parameter ϵ to determine reflects by how much the intercept exceeds criticality. In this work, a further correction is taken into account, corresponding to a two-pion loop.

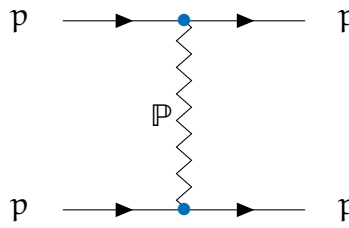


Figure 5.1: Diagram of Pomeron pole exchange between two protons.

The implementation of the first point is self-explanatory. The choices associated with $\beta(t)$, however, are subject to more consideration. In fact, the exact form factor related to this interaction is unknown and some parametrization must be selected. Recall that in Section 2.2.2 it was mentioned that the imaginary contributions to amplitudes are expected to peak at $t = 0$ and decrease quickly as $|t|$ increases.

At a simple level, the vertex is often modeled as an exponential in t (with two parameters), as follows:

$$\beta_{\mathbb{P}}(t) = \beta_{\mathbb{P}}(0)e^{r_{\mathbb{P}}t/2}. \quad (5.4)$$

This choice will be referred to as Model I. Parameters $\beta_{\mathbb{P}}(0)$ and $r_{\mathbb{P}}$ are obtained from the fitting procedure. In the region of interest (s -channel) t is negative, therefore the use of an exponential vertex reflects the qualitative behavior expected from the amplitudes.

Another common two-parameter approach to the proton-Pomeron vertex is using a power-like vertex of the form:

$$\beta_{\mathbb{P}}(t) = \frac{\beta_{\mathbb{P}}(0)}{(1 - t/m_{\rho}^2)(1 - t/\alpha_{\mathbb{P}})}. \quad (5.5)$$

This type of vertex will be used in Model II. In this model, factors $\alpha_{\mathbb{P}}$ and $\beta_{\mathbb{P}}(0)$ are obtained from the fit. The quantity m_{ρ} that appears in the expression refers to the mass of the ρ meson. The relevance of this meson on the form factors of strongly interacting particles is discussed further in the next section.

The implementation of these two models enabled the comparison of vertices that appear in the literature of the area. Note that it is also possible to implement a more complex vertex with a higher number of parameters. In the early stages of this work, several proton-Pomeron vertex expressions were tested, including, for instance, linear combinations of exponentials, and thus more free parameters. Consequently, it was determined that the improvements in the small t region were not significant enough to justify the increased computational cost.

5.1.2| Correction to the Pomeron Trajectory

Regarding the Pomeron trajectory, the two-pion loop correction (see Figure 5.2) results in a trajectory of the following form:

$$\alpha_{\mathbb{P}}(t) = 1 + \epsilon + \alpha'_{\mathbb{P}} t \frac{m_{\pi}^2}{32\pi^3} h(\tau), \quad (5.6)$$

where variable τ is given by $\tau = 4m_{\pi}^2/|t|$. The constant m_{π} is the mass of the pion (139.6 MeV).

There is a lot to be said about function $h(\tau)$, and the terms therein. Note that this chapter provides a general overview of the multiple choices that were required to apply the models used in this work. However, many of them have their own rich histories and several valid approaches, making it unfeasible to provide a truly comprehensive account of these topics.

First of all, consider why the two-pion loop in Figure 5.2 should be included. This stems from taking into account the nearest singularity with respect to the Pomeron trajectory, as required by t -channel unitarity. This singularity corresponds to the two-pion production threshold. Pions are the lightest mesons, as well as the lightest hadrons. In fact, due to this, the pion was thought to carry the strong interaction before QCD was established.

The correction function $h(\tau)$ is defined as [70–72]:

$$h(\tau) = -\frac{4}{\tau} F_{\pi}^2(t) \left[2\tau - (1 + \tau)^{3/2} \ln \left(\frac{\sqrt{1 + \tau} + 1}{\sqrt{1 + \tau} - 1} \right) + \ln \left(\frac{m^2}{m_{\pi}^2} \right) \right]. \quad (5.7)$$

The expression includes a scaling mass m , typically fixed at 1 GeV. The factor $F_{\pi}^2(t)$ is the pion-Pomeron vertex. The standard expression for the vertex corresponds to a simple pole and has the form $F_{\pi}(t) = \beta_{\pi}/(1 - t/\alpha_1)$, where β_{π} specifies the value of the coupling.

The mass scale α_1 is the square of the mass of the ρ meson (775.5 MeV). This choice is due to an effective theory called *Vector Meson Dominance*, which preceded the current knowledge of QCD [73]. It was based on the postulate that the hadronic contributions to photon vacuum polarization should only correspond to light vector mesons. Out of this category of particles, the ρ meson would be dominant, as it is the lightest.

Through these assumptions, the pion form factor is obtained from a low-order approach to the electromagnetic vacuum interactions of the pion [74]. Its decrease is found to be regulated by the dominant vector meson, hence the term $\alpha_1 = m_{\rho}^2$. It

is worth mentioning that, although Vector Meson Dominance still proves useful, it does not provide a full picture of hadronic interactions. In fact, other valid approaches to the pion-Pomeron vertex can be implemented. The magnitude of α_1 could be a parameter determined through the fitting procedure, for example. This also explains the mass term that appears in the proton-Pomeron form factor in equation (5.5).

Once again, the form factor cannot be obtained from first principles, but several parametrizations can be proposed. Reasonable restrictions on the behavior of the amplitudes with t are usually the driving force behind these choices. Differential cross-sections, as functions of t , are key to the evaluation of the agreement of these form factors with experiments. For the elastic scattering regime, the observable is slightly better described by inverse power parametrizations at small $|t|$. However, exponential form factors are conventionally used, as they guarantee that soft amplitudes decrease faster than those from perturbative regimes. This provides a desirable asymptotic behavior at higher t , while still showing good agreement closer to the forward region [75]. The form factor chosen here is standard, and should not greatly affect the results [76].

The most important assumption regarding the pion-loop correction is that according to the additive quark model, β_π relates to the proton-Pomeron coupling by $\beta_\pi/\beta_P(0) = 2/3$. This relation has been verified through experimental ratios of pion-proton and proton-proton cross-sections (at low energy) [76]. It stems from modeling hadron-hadron interactions in terms of Pomeron exchanges between two quarks, each belonging to one of the hadrons. The total amplitudes of a hadron-hadron interaction mediated by a Pomeron are then proportional to the amounts of quarks in each hadron. That is, an interaction amplitude between hadron 1 (with n_1 quarks) and hadron 2 (with n_2 quarks) has a multiplicative factor $n_1 n_2$ [77]. As a pion contains two quarks and a proton has three, the ratio between pion-proton and proton-proton total cross-sections is then found to be $2/3$.

Although a lot has been stated so far about the choices in the implementation of the pion-loop correction, the origin of equation (5.7) is yet to be explained. The role of $h(\tau)$ is modeling the behavior of the Pomeron trajectory near the pion production singularity. This can be done to different levels of precision. The expression used in this case can be obtained by studying once again the unitarity and analytical continuation of partial waves in the t -channel. A more complete picture of the considerations behind this is presented in [70].

The inclusion of the nonlinear terms in the trajectory affects the slope of the diffraction peak centered at $t = 0$. In other words, it affects the behavior of the differential cross-section, as this is the observable that contains process information in

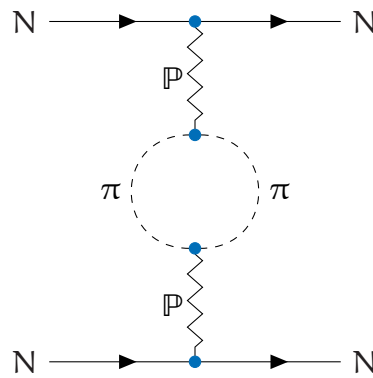


Figure 5.2: Feynman diagram for the two-pion loop contribution to Pomeron exchange in nucleon interaction.

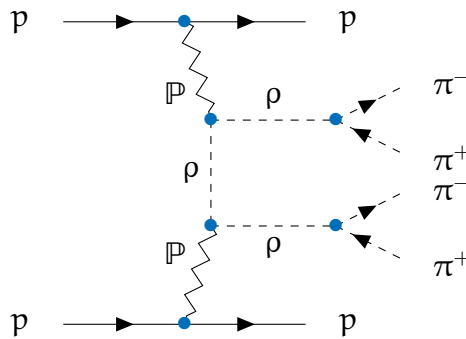


Figure 5.3: Example of proton-proton event diagram with Pomeron and ρ -meson contributions.

terms of the angle (expressed through variable t). This effect is particularly relevant at small t . When applied jointly with the eikonal approximation, the effects of both corrections tend to eliminate the dependence of the slope with t (close to $t = 0$), which is consistent with the available data. It is worth mentioning that the magnitude of the effect of the pion-loop correction is influenced by the energy as well [76].

Having established how the dominant Reggeon contribution of the Pomeron was implemented in this work, the following section will show the details of the inclusion of secondary Reggeons $f(\alpha)$ and $\omega(\rho)$.

5.1.3| Secondary Reggeon Trajectories $f - \alpha$ and $\omega - \rho$

The secondary contributions considered are those corresponding to mesonic Regge trajectories. These meson trajectories interpolate light mesons ρ , f , α and ω . An example of a proton-proton scattering process with contributions from ρ -mesons (which decay into pion pairs) can be seen in Figure 5.3.

The intercepts for the light meson Regge trajectories are below 1, but greater than

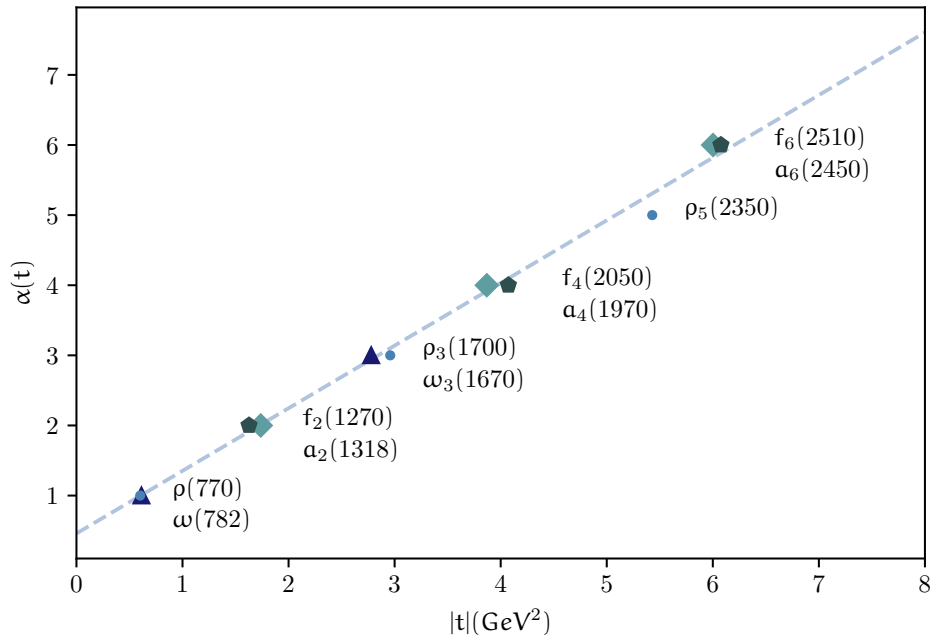


Figure 5.4: Chew-Frautschi plot of $|t| = m^2$ (energy) vs spin (angular momentum) for leading mesonic trajectories, with a linear fit. Data from PDG [3]

for other possible trajectories, such as those linked to baryons. When calculating amplitudes, only two contributions for meson trajectories were included. This is due to the phenomena of *exchange degeneracy* that Regge trajectories display. As can be seen in the plot in Figure 5.4, the trajectories interpolating each of these meson families are essentially overlapping¹. Although the degeneracy of the trajectories is not an exact property, it is still reasonable to use it to justify excluding further mesonic trajectories from the analysis.

The choice of only two distinct trajectories is explained by the fact that one of these trajectories was given a positive signature and the a second negative one. Therefore, implementing these two is sufficient to represent the interpolation over even and odd angular momenta. From now on, the functions and parameters for $f - a$ degenerate trajectories will be indicated with subscript (+) and those related to $\omega - \rho$ mesons will be labeled (-).

Due to the smaller effects on the amplitudes that these trajectories represent (when compared to the Pomeron), they will simply be taken as linear. The fit from Figure 5.4 shows that this is a reasonable choice according to current data for the properties of the light mesons. As the intercepts are known to be smaller than 1 the fit parameters

¹It is also worth pointing out that the figure shows that they remain broadly linear as $|t|$ increases.

ϵ_{\pm} were used as follows:

$$\alpha_{\pm}(t) = 1 - \epsilon_{\pm} + \alpha'_{\pm} t. \quad (5.8)$$

The values for the slopes of these trajectories were chosen to be fixed at 0.9 GeV^{-2} . It is well-established that the mesonic (and baryonic) Regge trajectories all present similar slopes of approximately this value. This is in fact verified by the fit shown in Figure 5.4 for the latest Particle Data Group data on the masses of the interpolated mesons [3]. A key difference between mesonic and Pomeron/Odderon trajectories is that meson trajectories interpolate known, and oftentimes detectable particles. Therefore their trajectories can be determined as shown in the plot, instead of working with cross-section data.

Fixing some of the Reggeon parameters before performing a cross-section fit can drastically reduce the computational intensiveness of the approach. As such, it is useful to include this previous knowledge for secondary contributions, prioritizing the determination of Pomeron and Odderon parameters.

Just as in the Pomeron case, the proton-Reggeon vertices β_{\pm} are chosen to be exponential, and can be expressed as follows:

$$\beta_{+}(t) = \beta_{+}(0)e^{r_{+}t/2} \quad (5.9)$$

$$\beta_{-}(t) = \beta_{-}(0)e^{r_{-}t/2}. \quad (5.10)$$

The parameters r_{+} and r_{-} were fixed at 4.0 GeV^{-2} . This choice is consistent with previous determinations of these parameters. It has also been shown that the values of the secondary Reggeon form factor slopes have little statistical effect on the results obtained for the Pomeron [67]. The coupling magnitudes $\beta_{\pm}(0)$ were determined through the fits that were carried out.

The inclusion of secondary Reggeons better reflects the shape of experimental cross-sections at low energy. It also leads to differences between proton-proton and proton-antiproton cross-sections. The Pomeron has the quantum numbers of the vacuum and therefore should couple equally to particles and antiparticles [78]. As a result, a Pomeron exchange is not enough to reflect the clear differences in the experimental data for pp and $p\bar{p}$ scattering. This is achieved through the inclusion of the negative signature secondary contribution. The relationship between Reggeon signature and particle-particle or particle-antiparticle scattering is discussed further in Section 5.2.

5.1.4| Odderon

At this stage, the remaining Reggeon trajectory to discuss is that of the Odderon. The Odderon, as was introduced in Chapter 3, is the odd-signature counterpart of the Pomeron. This Regge state also corresponds to the exchange of a series of unknown gluon states, and as such its trajectory needs to be modeled in a similar way to the Pomeron. The fits to experimental data were performed separately from only the Pomeron and secondary Reggeons, and adding the Odderon.

The choices of proton-Odderon vertex lead to two further models which will be considered. Model III considers an Odderon with an exponential vertex

$$\beta_{\mathbb{O}}(t) = \beta_{\mathbb{O}}(0)e^{r_{\mathbb{O}}t/2}. \quad (5.11)$$

The value of $r_{\mathbb{O}}$ was chosen according to $r_{\mathbb{O}} = r_{\mathbb{P}}/2$. Meanwhile, in Model IV the form factor is, analogously to the Pomeron case, power-like:

$$\beta_{\mathbb{O}}(t) = \frac{\beta_{\mathbb{O}}(0)}{(1 - t/m_{\mathbb{P}}^2)(1 - t/a_{\mathbb{O}})}, \quad (5.12)$$

where $a_{\mathbb{O}} = 2a_{\mathbb{P}}$. Although the choices for $r_{\mathbb{O}}$ and $a_{\mathbb{O}}$ are somewhat arbitrary, they are justified by the expectation that Odderon contributions should decrease slower in t than those of the Pomeron (see for example [79]).

The chosen trajectory for the Odderon considered was simply $\alpha_{\mathbb{O}}(t) = 1$ for all models. This choice is consistent with some predictions for the Odderon intercept stemming from recent works, using, for example, perturbative methods [80–82].

A new parameter for the Odderon was introduced, representing the positivity of the Odderon contribution. Although Pomeron amplitudes are known to be positive, it is not well established if the Odderon contributions must obey this as well [83, 84]. The two possibilities were therefore taken into account when performing the fits. The inclusion of this positivity parameter will be discussed further later in the chapter.

It is worth mentioning that the Odderon effects are expected to be noticeable in some particular aspects of scattering. The first one is at high energies, where, in particular, it should affect the ratio of imaginary and real amplitudes. This is how it was observed, from the first determinations of the ρ parameter at 13 TeV, as obtained by the TOTEM collaboration [9, 10]. The ρ parameter is discussed in Section 5.2.

As a negative signature trajectory, the Odderon should distinguish between proton-proton and proton-antiproton scattering. In particular, the analysis of the differential cross-section away from the forward direction shows significant Odderon effects, see for example [85].

5.1.5| Summary of Fitted and Fixed Parameters

The following tables offer a summary of the Reggeon parameters that were used and other choices which were mentioned in previous sections. It also shows which parameters were obtained through the χ^2 procedure and which were fixed. Table 5.1 corresponds to Models I and III, for the exponential form factor case with and without Odderon. Table 5.2 does the same for the power-like vertices of Models II and IV.

		Pomeron	$f - a$	$\rho - \omega$	Odderon
Trajectory	ϵ	Fitted	Fitted	Fitted	0
	α'	Fitted	0.9 GeV^{-2}	0.9 GeV^{-2}	0
	Linear	No	Yes	Yes	—
Vertex	Type	Exponential	Exponential	Exponential	Exponential
	$\beta(0)$	Fitted	Fitted	Fitted	Fitted
	r	Fitted	4.0 GeV^{-2}	4.0 GeV^{-2}	$r_{\mathbb{P}}/2$
Signature	η	+	+	—	—

Table 5.1: Summary of the parameters and terms used for each Reggeon in Model I (without Odderon) and Model III (with Odderon).

		Pomeron	$f - a$	$\rho - \omega$	Odderon
Trajectory	ϵ	Fitted	Fitted	Fitted	0
	α'	Fitted	0.9 GeV^{-2}	0.9 GeV^{-2}	0
	Linear	No	Yes	Yes	—
Vertex	Type	Power-like	Exponential	Exponential	Power-like
	$\beta(0)$	Fitted	Fitted	Fitted	Fitted
	a	Fitted	—	—	$2a_{\mathbb{P}}$
	r	—	4.0 GeV^{-2}	4.0 GeV^{-2}	—
Signature	η	+	+	—	—

Table 5.2: Summary of the parameters and terms used for each Reggeon in Model II (without Odderon) and Model IV (with Odderon).

5.2| Computed Observables

The Regge amplitudes which can be calculated from the Reggeon contributions were used to compare with three observables. These were total cross-sections, differential cross-sections, and a ratio known as the ρ parameter, which relates the real and imaginary parts of forward amplitudes. These were obtained for both proton-proton and proton-antiproton scattering. This section shows how the observables relate to Regge amplitudes.

First of all, consider how the contributions of different Regge trajectories (as obtained from (5.1)) should be added. In order to obtain Born-level amplitudes it is sufficient to add the different contributions. The main detail that must be taken into account is how the addition should deal with crossing-even and crossing-odd amplitudes. Recall from Section 3.4.2 that a crossing operation introduces a change of sign for odd scattering amplitudes. Taking this into account, alongside the crossing relation between a proton and an antiproton, the Born-level amplitude addition is:

$$A(s, t) = A_{\mathbb{P}}(s, t) + A_+(s, t) + A_-(s, t) + \xi_0 A_0(s, t) \text{ for } pp \text{ scattering} \quad (5.13)$$

$$A(s, t) = A_{\mathbb{P}}(s, t) + A_+(s, t) - A_-(s, t) - \xi_0 A_0(s, t) \text{ for } p\bar{p} \text{ scattering} \quad (5.14)$$

It is worth noting that in the literature the correspondence of each expression with the pp and $p\bar{p}$ case may be inverted, as it depends on whether the minus sign was included in the expression for $\eta_-(t)$ in (5.3). The factors ξ_0 represent the positivity options that were considered for the Odderon, which relate to the phase that its contribution may exhibit. The results were tested for $\xi_0 = 1$ and $\xi_0 = -1$.

When implementing unitarization procedures it is more precise to carry out the sum for functions $\chi(s, b)$ and $\tilde{\chi}(s, b)$. The same sign changes due to crossing properties apply in this approach [68, 86], leading to:

$$\chi(s, b) = \chi_{\mathbb{P}}(s, b) + \chi_+(s, b) + \chi_-(s, b) + \xi_0 \chi_0(s, b) \text{ for } pp \text{ scattering} \quad (5.15)$$

$$\chi(s, b) = \chi_{\mathbb{P}}(s, b) + \chi_+(s, b) - \chi_-(s, b) - \xi_0 \chi_0(s, b) \text{ for } p\bar{p} \text{ scattering.} \quad (5.16)$$

Then, these functions including all Reggeon contributions are used according to Equations (4.8) and (4.10) to obtain the unitarized amplitudes.

The calculation of the cross-sections for each case utilizes the optical theorem presented in Section 2.2.2:

$$\sigma_{\text{tot}} = \frac{1}{s} \text{Im } A_{el}(s, t = 0), \quad (5.17)$$

where elastic amplitude $A_{el}(s, t)$ will correspond to $A_{eik}(s, t)$ or $A_{U-mtx}(s, t)$.

Then, elastic differential cross-sections relate to the elastic scattering amplitudes by:

$$\frac{d\sigma}{dt}(s, t) = \frac{\pi}{s^2} |A(s, t)|^2. \quad (5.18)$$

Notice how in this case, the angular dependence is expressed through Mandelstam variable t . Furthermore, this is the only observable where nonelastic amplitudes were considered ($t \neq 0$).

The last observable that was taken into account was the ρ parameter, as defined by:

$$\rho(s) = \frac{\text{Re } A(s, t = 0)}{\text{Im } A(s, t = 0)}. \quad (5.19)$$

This quantity only depends on forward scattering amplitudes, just like the total cross-sections. However, there are several reasons to justify including it in the analysis. First, it is important to note that the relationship between the imaginary and real components of amplitudes is given by the analyticity and unitarity properties which were extensively discussed throughout this work. Moreover, ρ is predicted to approach 0 from above for $s \rightarrow \infty$. As such, it could be used as an indicator of whether the asymptotic region has been reached by current experimental data [23].

The behavior of the parameter in Regge theory will be dominated by the magnitude of the Pomeron intercept, therefore its inclusion in the fits could produce more reliable results. The ρ parameter is also sensitive to Odderon contributions. Particularly, as shown in [9] recent TOTEM values for the parameter led to the announced discovery of the Odderon in 2021.

The following section explains the datasets for these three observables, as they were used in the analysis carried out in this work.

5.3| Experimental Data

The fits were performed and contrasted for data corresponding to two collaborations at the LHC, TOTEM and ATLAS. TOTEM stands for *TOTAL Elastic and diffractive cross section Measurement*. One of the main goals of this experiment is to achieve great precision in the study of proton-proton collisions. It specializes in the measurement of the forward scattering region [87]. The ATLAS (A Toroidal LHC Apparatus) experiment on the other hand is a general-purpose detector, focused on registering as broad as possible a range of signals that could be produced, allowing for the possible detection

of physics beyond the standard model [88].

Due to the intrinsically different focus of both of these experiments, there are discrepancies between the total cross-section measurements they have produced. This justifies this thesis' goal of obtaining and comparing results for the two, to shed some light on how present models of diffractive and elastic scattering relate to both datasets.

The two collaborations have released data up to $\sqrt{s} = 13$ TeV of energy [89–91]. These correspond to all the observables mentioned in the previous sections. In particular, the analysis included:

- Total cross-section (σ_{tot}) and ρ parameter data for pp up to 13 TeV.
- Differential cross-section data for elastic pp scattering, at 7, 8 and 13 TeV [92–95].

Due to the focus on elastic and diffractive (soft) contributions, the differential cross-section data used was restricted to the quasi-forward region. The fitting procedure was carried out for $-t \leq 0.1$ GeV. This provides more experimental input on the shape of the diffractive peak to improve results for amplitudes near the forward region. It is worth noting that TOTEM data provides both a higher number of data points for the differential cross-sections and values for a greater range in t .

For each experiment, the results for all three observables were subject to a simultaneous fitting procedure, which is detailed in the next section. Note that the lower energy data is not necessarily from the LHC, but comes from the Particle Data Group datasets which concatenate the measurements of several experiments, such as the Tevatron [3]. This is, in particular, true for all the proton-antiproton data used.

5.4| Fitting Method: χ^2

The fits for the experimental data were performed through a χ^2 function. The function measures the quality of the fit for the experimental dataset, weighted according to the error of each data point. It was defined as:

$$\chi^2 = \sum_i \left(\frac{X_{\text{teo}}^i - X_{\text{exp}}^i}{\Delta X^i} \right)^2, \quad (5.20)$$

where X_{exp}^i refers to an experimental data point, X_{teo}^i refers to the corresponding prediction from Reggeon amplitudes, and ΔX^i to the experimental error. Note that the summation is carried over all the considered data, for all of the observables stemming from an experiment. The goodness of fit was evaluated by taking χ^2/ν , where ν represents the degrees of freedom. However, the dominance of systematic error in the data (non-Gaussian distribution) limits the interpretation of this measure.

In order to obtain values for the theoretical model values, a minimization procedure was carried out for χ^2 . The MINUIT library was chosen for this purpose [96]. This tool specializes in the minimization of functions with multiple parameters, through χ^2 methods. It was developed at CERN and is a standard approach to minimization in High Energy Physics.

The MINUIT library offers multiple minimization algorithms, as well as tools for error determination. This work used the Migrad minimizer, which is appropriate for most purposes. The errors were calculated through the HESSE method, which provides an error matrix (inverse of the second-derivative matrix) and parameter errors [97].

Migrad receives a user-defined χ^2 function and initialization values for the parameters. Another user input is the desired confidence level, which in this case was set at 90%.

To summarize, this chapter specified several choices required to model the Reggeon contributions from the Pomeron, Odderon, and secondary trajectories. The scattering amplitudes were unitarized utilizing the eikonal function or the U-matrix. Then, these new amplitudes were used to calculate observables, through relations from Section 5.2 such as the optical theorem. The parameter producing the best predictions according to the experimental data from TOTEM and ATLAS were determined through χ^2 minimization. The following chapter displays the results obtained for each of the unitarization schemes and datasets considered.

6 Results

This chapter will show the main results that were obtained from the fitting procedure. Recall that these were produced for models taking into account the Pomeron and the secondary Reggeons, with and without the Odderon. The different models also refer to the choices of vertex form factor for the Pomeron and Odderon. The results correspond to the fits using the eikonal and U-matrix approaches, as well as the two datasets coming from the ATLAS and TOTEM experiments (Ensembles A and T, respectively). Recall that the lower energy data included in the datasets corresponds to PDG data. It is also worth noting that there are no proton-antiproton data points coming from ATLAS and TOTEM. To begin, a discussion of the fits without an Odderon contribution is provided.

6.1| Fits for the Pomeron

Table 6.1 presents the fitted parameters obtained for the Pomeron and secondary Reggeons using eikonal unitarization. This corresponds to Models I and II, that is, to the two proton-Pomeron form factors considered. The results from the analogous procedure for the U-matrix scheme are presented in Table 6.2.

The experimental data and the fits for ATLAS and TOTEM with Models I and II are shown in the plots of Figures 6.1, 6.2, 6.3, and 6.4. The first and third of these figures correspond to the proton-proton and proton-antiproton cross-sections and ρ parameter for the eikonal and the U-matrix. The second and fourth show the pp elastic differential cross-sections at 7, 8, and 13 TeV for the eikonal and the U-matrix. Note that the experimental data points from ATLAS and TOTEM are highlighted in the plots.

For the Pomeron-based models, the fits obtained show comparable agreement with the datasets for both the eikonal and U-matrix schemes. This can be observed by noting that the values of χ^2/ν take very similar values for both unitarization schemes (when looking at the same model and dataset). Although the values of χ^2/ν for Ensemble T were significantly smaller than those for Ensemble A, there are limitations when evaluating the fit quality. This suggests that this difference is mainly related to the

higher density in differential cross-section measurements (higher degrees of freedom).

The estimates for the Pomeron intercept are slightly sensitive to the choices of vertex form factor and unitarization scheme. However, they are overall compatible with each other, and with previous estimates present in the literature. A result worth highlighting is that TOTEM data reliably results in higher Pomeron intercepts for all models, as well as approximately constant trajectories ($\alpha_{\mathbb{P}}$ compatible with zero).

The more significant differences in the parameters for both experimental ensembles are related to the leading Pomeron contribution, as expected. However, they tend to manifest themselves in parameters such as the trajectory slope $\alpha'_{\mathbb{P}}$ and those parameters regulating the slopes of the Pomeron-hadron vertices, $r_{\mathbb{P}}$ and $a_{\mathbb{P}}$. The discrepancies are particularly significant when contrasting the results for Ensembles A and T, with everything else being equal. This can be attributed to the observation that the differential cross-sections for the ensembles display a vertical shift in relation to each other, at all the considered energy levels. Therefore, they could be explained by the systematic error introduced by each of the datasets.

6. RESULTS

	Eikonal			
	Ensemble A		Ensemble T	
	Model I	Model II	Model I	Model II
ϵ	0.1014 ± 0.0033	0.1112 ± 0.0013	0.1248 ± 0.0027	0.1336 ± 0.0023
$\alpha'_{\mathbb{P}}(\text{GeV}^{-2})$	0.2938 ± 0.0022	0.1148 ± 0.0076	0.56×10^{-9} ± 0.11	0.009 ± 0.040
$\beta_{\mathbb{P}}(0)(\text{GeV}^{-1})$	2.154 ± 0.063	1.999 ± 0.023	1.814 ± 0.043	1.742 ± 0.028
$r_{\mathbb{P}}(\text{GeV}^{-2})$	2.375 ± 0.019	—	7.448 ± 0.087	—
$\alpha_{\mathbb{P}}(\text{GeV}^2)$	—	0.829 ± 0.081	—	0.499 ± 0.084
ϵ_+	0.360 ± 0.048	0.344 ± 0.030	0.286 ± 0.025	0.262 ± 0.015
$\beta_+(0)(\text{GeV}^{-1})$	4.56 ± 0.47	4.374 ± 0.34	4.02 ± 0.21	3.93 ± 0.14
ϵ_-	0.556 ± 0.010	0.550 ± 0.089	0.536 ± 0.067	0.530 ± 0.064
$\beta_-(0)(\text{GeV}^{-1})$	3.68 ± 0.16	3.55 ± 0.67	3.41 ± 0.49	3.39 ± 0.46
ν	226	226	350	350
χ^2/ν	0.86	0.83	0.74	0.65

Table 6.1: Fitted parameters obtained with Eikonal unitarization for the Pomeron (and secondary Reggeon) models.

	U-matrix			
	Ensemble A		Ensemble T	
	Model I	Model II	Model I	Model II
ϵ	0.0911 ± 0.0037	0.0981 ± 0.0029	0.1129 ± 0.0048	0.1150 ± 0.0070
$\alpha'_{\mathbb{P}}(\text{GeV}^{-2})$	0.4425 ± 0.0085	0.2728 ± 0.0089	0.05 ± 0.14	0.10 ± 0.12
$\beta_{\mathbb{P}}(0)(\text{GeV}^{-1})$	2.271 ± 0.075	2.140 ± 0.056	1.926 ± 0.085	1.92 ± 0.11
$r_{\mathbb{P}}(\text{GeV}^{-2})$	0.1051 ± 0.0061	—	7.2 ± 2.8	—
$\alpha_{\mathbb{P}}(\text{GeV}^2)$	—	40 ± 20	—	0.62 ± 0.49
ϵ_+	0.356 ± 0.057	0.369 ± 0.049	0.325 ± 0.050	0.314 ± 0.053
$\beta_+(0)(\text{GeV}^{-1})$	4.71 ± 0.65	4.51 ± 0.48	4.18 ± 0.43	4.14 ± 0.44
ϵ_-	0.551 ± 0.098	0.551 ± 0.043	0.545 ± 0.074	0.542 ± 0.075
$\beta_-(0)(\text{GeV}^{-1})$	3.59 ± 0.74	3.54 ± 0.34	3.43 ± 0.54	3.43 ± 0.54
ν	226	226	350	350
χ^2/ν	0.85	0.86	0.71	0.64

Table 6.2: Fitted parameters obtained with U-matrix unitarization for the Pomeron (and secondary Reggeon) models.

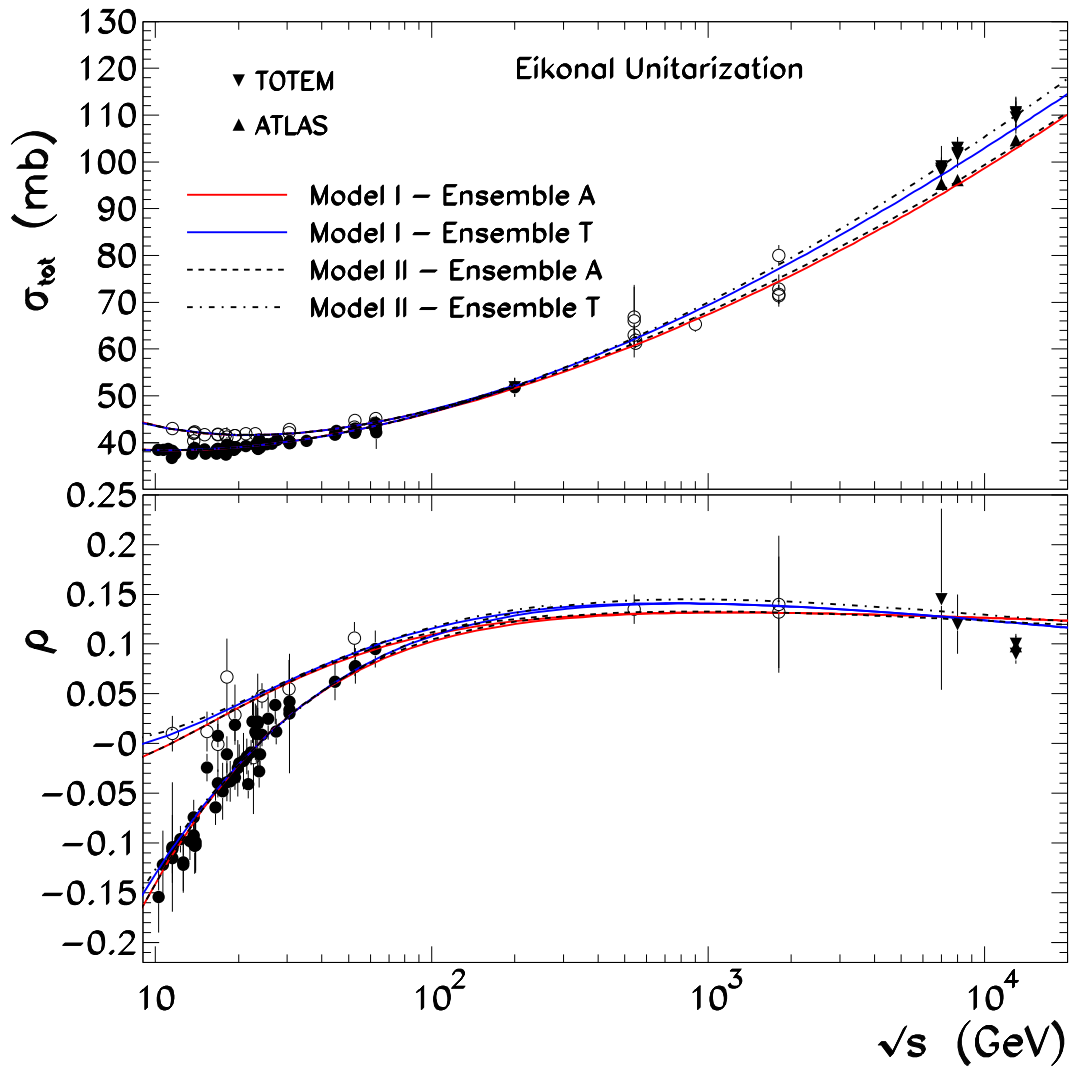


Figure 6.1: Total cross-section and ρ parameter fits for pp (\bullet , \blacktriangle , \blacktriangledown) and $p\bar{p}$ (\circ) channels. Results obtained using eikonal unitarization for Models I and II.

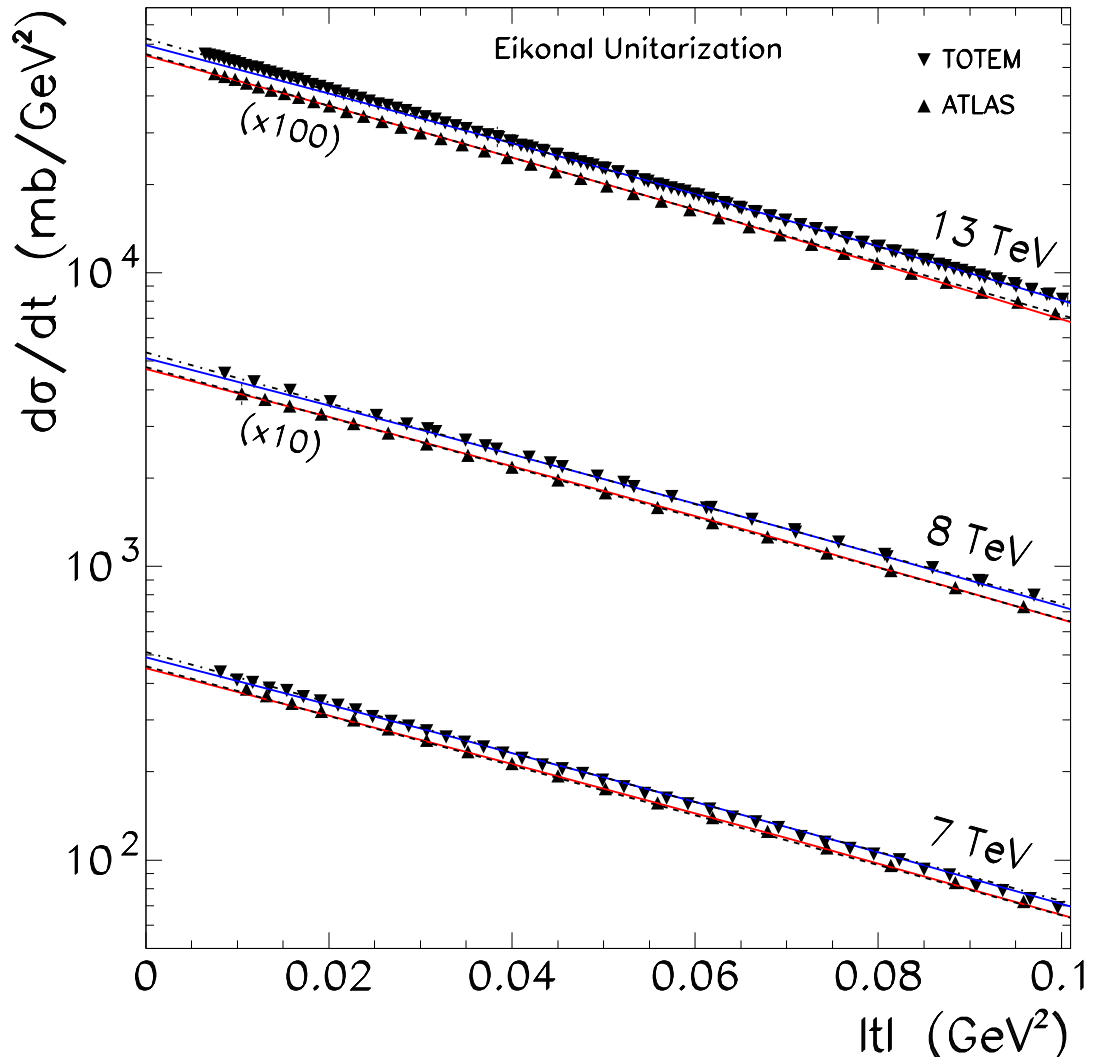


Figure 6.2: Differential cross-section for pp (\blacktriangle , \blacktriangledown) channel. Results obtained using eikonal unitarization for Models I and II.

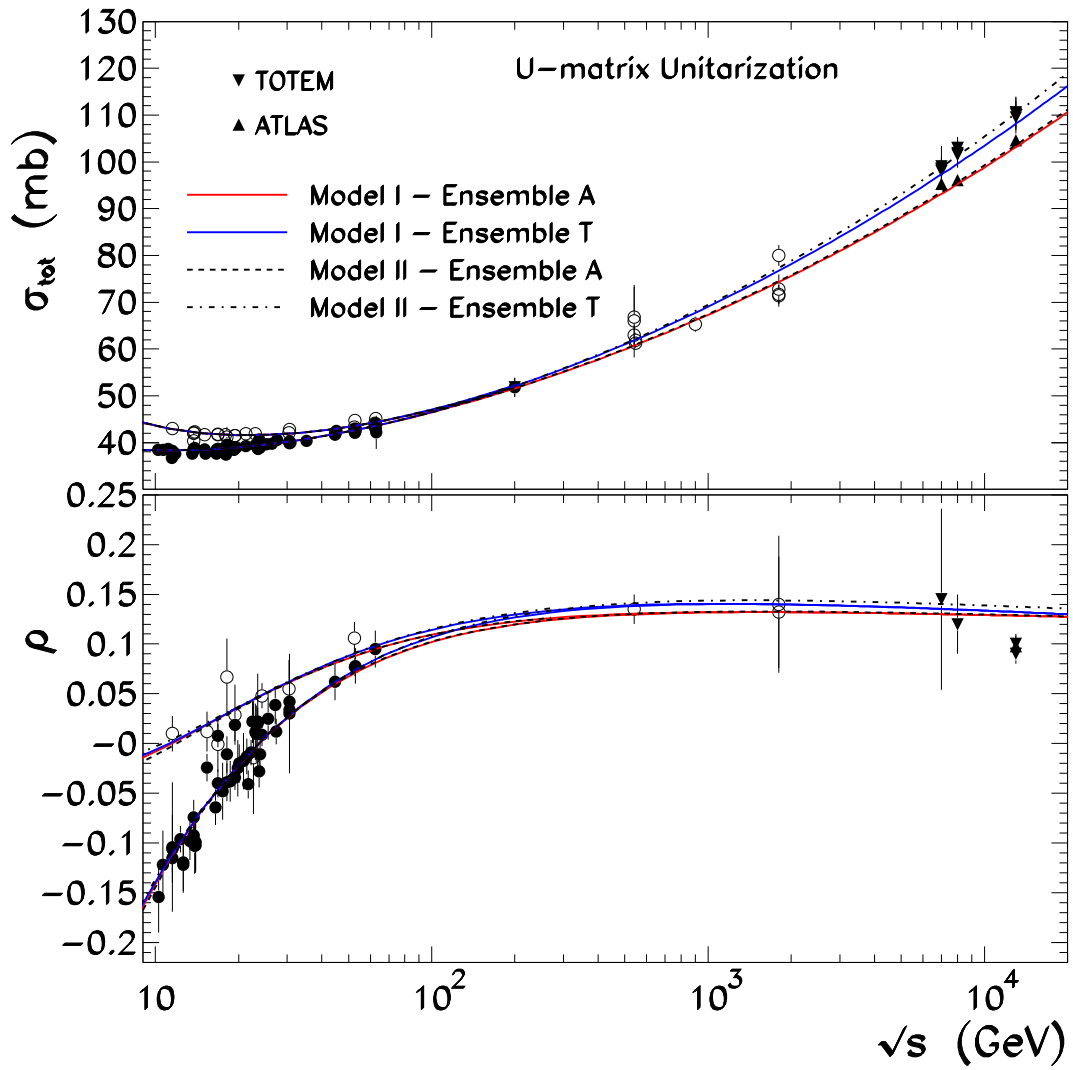


Figure 6.3: Total cross-section and ρ parameter fits for pp (\bullet , \blacktriangle , \blacktriangledown) and $p\bar{p}$ (\circ) channels. Results obtained using U-matrix unitarization for Models I and II.

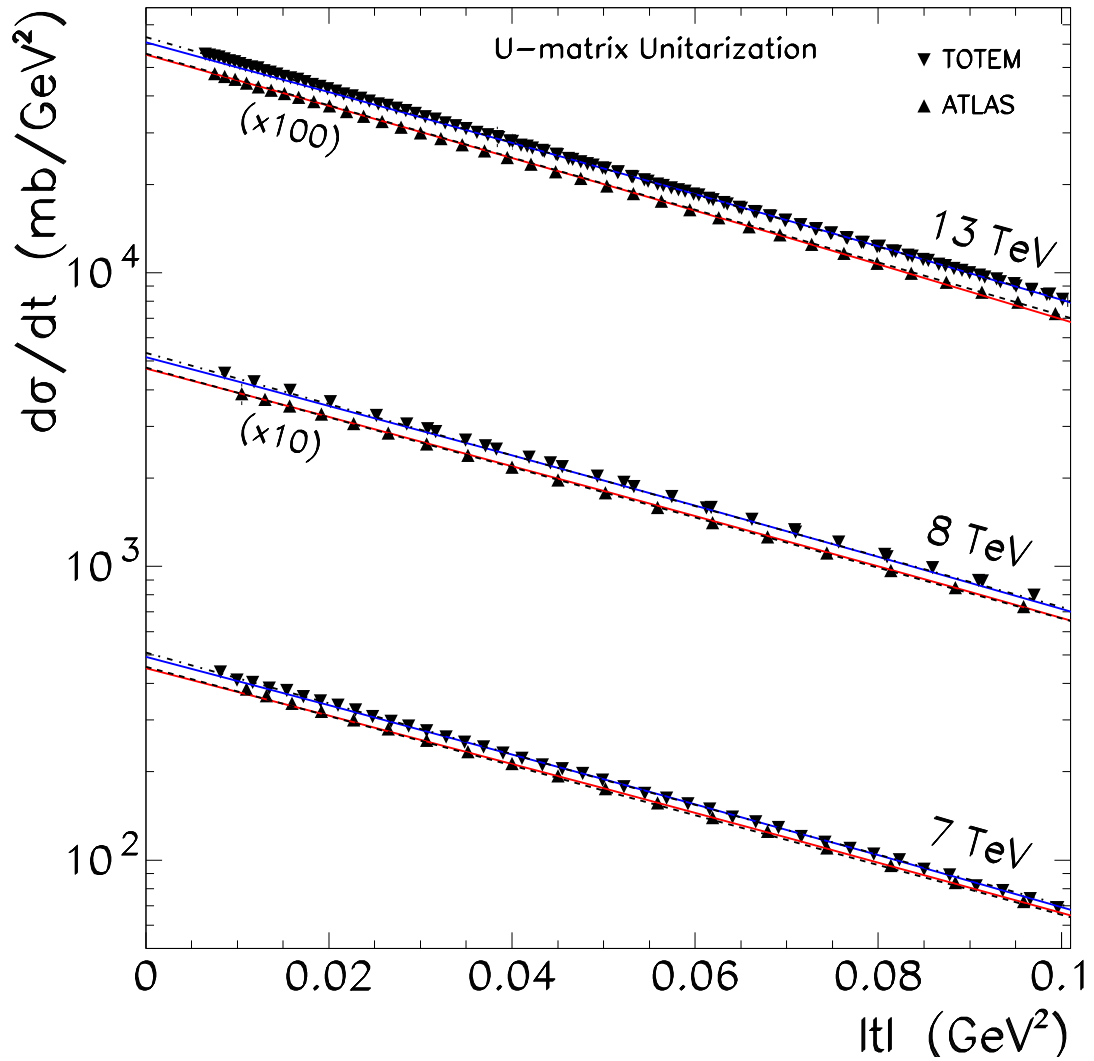


Figure 6.4: Differential cross-section for pp (\blacktriangle , \blacktriangledown) channel. Results obtained using U-matrix unitarization for Models I and II.

6.2| Fits for the Pomeron plus Odderon

6.2.1| The $\xi_0 = -1$ case

The results for Models III and IV, including the Pomeron and Odderon with exponential and power-like form factors are presented first for the $\xi_0 = -1$ case. The fit parameters for the eikonal and U-matrix are included in Tables 6.3 and 6.4. The fits are once again shown for all considered observables in Figures 6.4, 6.6, 6.7, and 6.8.

One of the more significant aspects to point out in the Odderon results is that the magnitude of the Odderon-hadron couplings $\beta_0(0)$ is significantly smaller than the couplings obtained for the Pomeron, as evidenced by all the cases that were included in the analysis¹. This helps explain the elusiveness of the Odderon, whose effects were only confirmed very recently.

A visible effect of the Odderon inclusion is the differentiation between proton-proton and proton-antiproton predictions for the ρ parameter. This can be observed by comparing Figures 6.1 and 6.5, or 6.3 and 6.7. These plots show that, for intermediate values of energy, the pp and $p\bar{p}$ ρ -parameter fits “cross” each other when the Odderon contribution is taken into account.

It is also worth mentioning that for the U-matrix and eikonal schemes, the fits obtained are good and of comparable quality, just as in the case of the Pomeron-only models. For most of the ensemble and scheme combinations, the fits are improved by considering the power-like vertices, as opposed to the exponential. This is consistent with what has been found previously, which suggests that power-like vertices better reflect the t dependence in the quasi-forward region. Perhaps this result would have been different if the differential cross-section data selected involved $-t > 0.1$ GeV, where the data could be more in line with the exponential vertices.

¹The magnitude difference in the couplings is also present for the secondary Reggeons. However, this result is not as relevant as the effect of the Pomeron and Odderon are most important at high energies, while the secondary Reggeon contributions affect the lower energy regions considered.

	Eikonal, $\xi_0 = -1$			
	Ensemble A		Ensemble T	
	Model III	Model IV	Model III	Model IV
ϵ	0.1017 ± 0.0043	0.1043 ± 0.0026	0.1247 ± 0.0048	0.1335 ± 0.0041
$\alpha'_p(\text{GeV}^{-2})$	0.283 ± 0.036	0.242 ± 0.012	0.94×10^{-4} ± 0.059	0.01 ± 0.11
$\beta_p(0)(\text{GeV}^{-1})$	2.146 ± 0.083	2.116 ± 0.011	1.815 ± 0.080	1.744 ± 0.035
$r_p(\text{GeV}^{-2})$	2.58 ± 0.68	—	7.45 ± 0.13	—
$a_p(\text{GeV}^2)$	—	31 ± 11	—	0.50 ± 0.16
ϵ_+	0.359 ± 0.055	0.353 ± 0.020	0.285 ± 0.051	0.261 ± 0.013
$\beta_+(0)(\text{GeV}^{-1})$	4.52 ± 0.54	4.47 ± 0.29	4.00 ± 0.38	3.91 ± 0.16
ϵ_-	0.4823 ± 0.0019	0.482 ± 0.077	0.490 ± 0.030	0.489 ± 0.077
$\beta_-(0)(\text{GeV}^{-1})$	3.20 ± 0.13	3.19 ± 0.50	3.14 ± 0.22	3.15 ± 0.50
$\beta_0(0)(\text{GeV}^{-1})$	0.47 ± 0.24	0.40 ± 0.17	0.31 ± 0.24	0.27 ± 0.20
ν	225	225	349	349
χ^2/ν	0.84	0.80	0.73	0.65

Table 6.3: Fitted parameters obtained with Eikonal unitarization for the Pomeron plus Odderon models, for $\xi_0 = -1$.

6. RESULTS

	U-matrix, $\xi_0 = -1$			
	Ensemble A		Ensemble T	
	Model III	Model IV	Model III	Model IV
ϵ	0.0938 ± 0.0045	0.0978 ± 0.0047	0.1115 ± 0.0035	0.1148 ± 0.0060
$\alpha'_p(\text{GeV}^{-2})$	0.364 ± 0.029	0.273 ± 0.031	0.10 ± 0.15	0.106 ± 0.098
$\beta_p(0)(\text{GeV}^{-1})$	2.215 ± 0.075	2.146 ± 0.066	1.951 ± 0.063	1.919 ± 0.093
$r_p(\text{GeV}^{-2})$	1.57 ± 0.58	—	6.2 ± 3.0	—
$a_p(\text{GeV}^2)$	—	40 ± 24	—	0.63 ± 0.41
ϵ_+	0.374 ± 0.031	0.369 ± 0.026	0.327 ± 0.071	0.313 ± 0.046
$\beta_+(0)(\text{GeV}^{-1})$	4.62 ± 0.50	4.49 ± 0.64	4.18 ± 0.72	4.12 ± 0.38
ϵ_-	0.490 ± 0.047	0.48 ± 0.33	0.49 ± 0.21	0.50 ± 0.12
$\beta_-(0)(\text{GeV}^{-1})$	3.18 ± 0.18	3.08 ± 0.79	3.11 ± 0.42	3.17 ± 0.71
$\beta_0(0)(\text{GeV}^{-1})$	0.44 ± 0.20	0.23 ± 0.15	0.32 ± 0.18	0.27 ± 0.18
ν	225	225	349	349
χ^2/ν	0.83	0.84	0.71	0.64

Table 6.4: Fitted parameters obtained with U-matrix unitarization for the Pomeron plus Odderon models, for $\xi_0 = -1$.

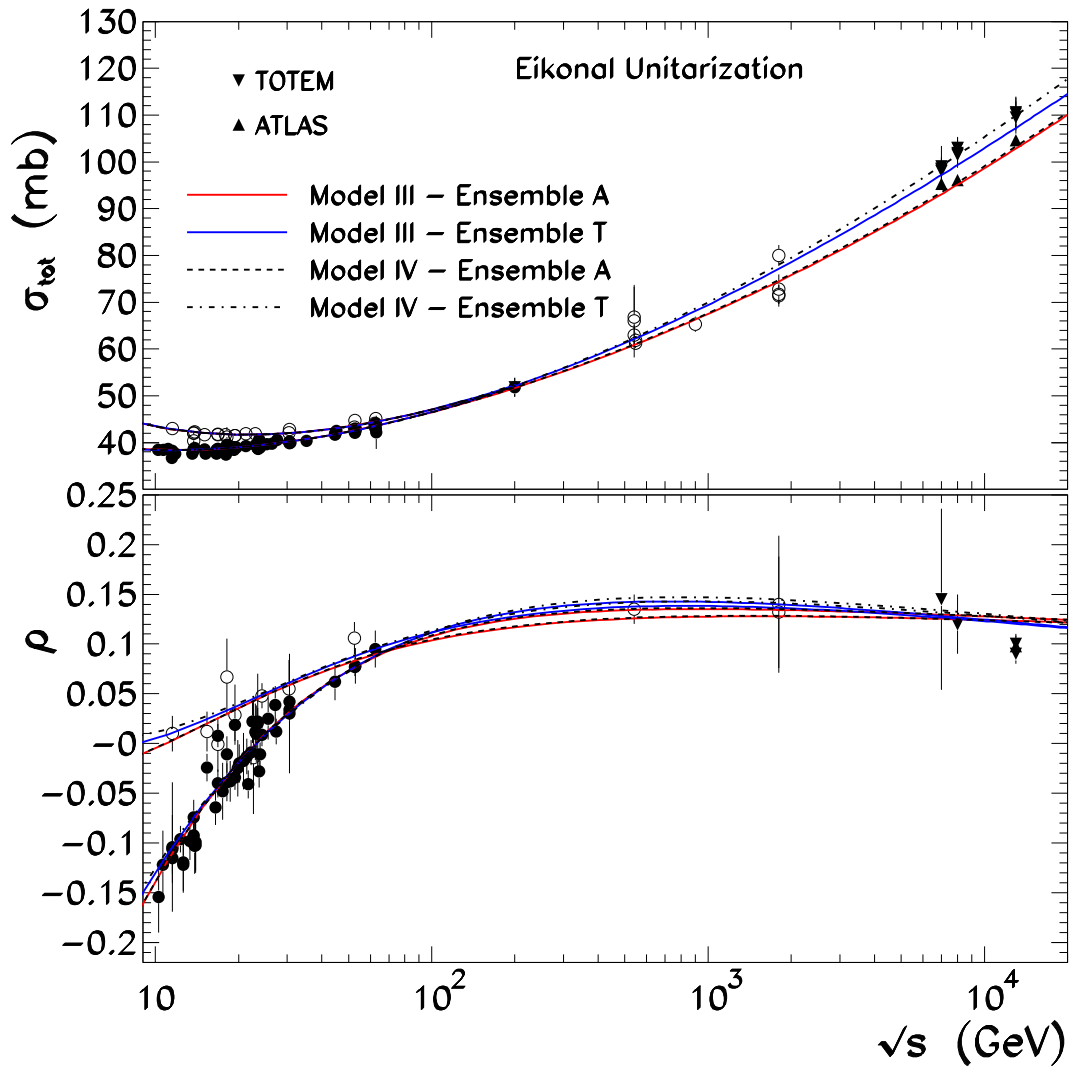


Figure 6.5: Total cross-section and ρ -parameter fits for pp (\bullet , \blacktriangle , \blacktriangledown) and $p\bar{p}$ (\circ) channels. Results obtained using eikonal unitarization for Models III and IV using $\xi_0 = -1$.

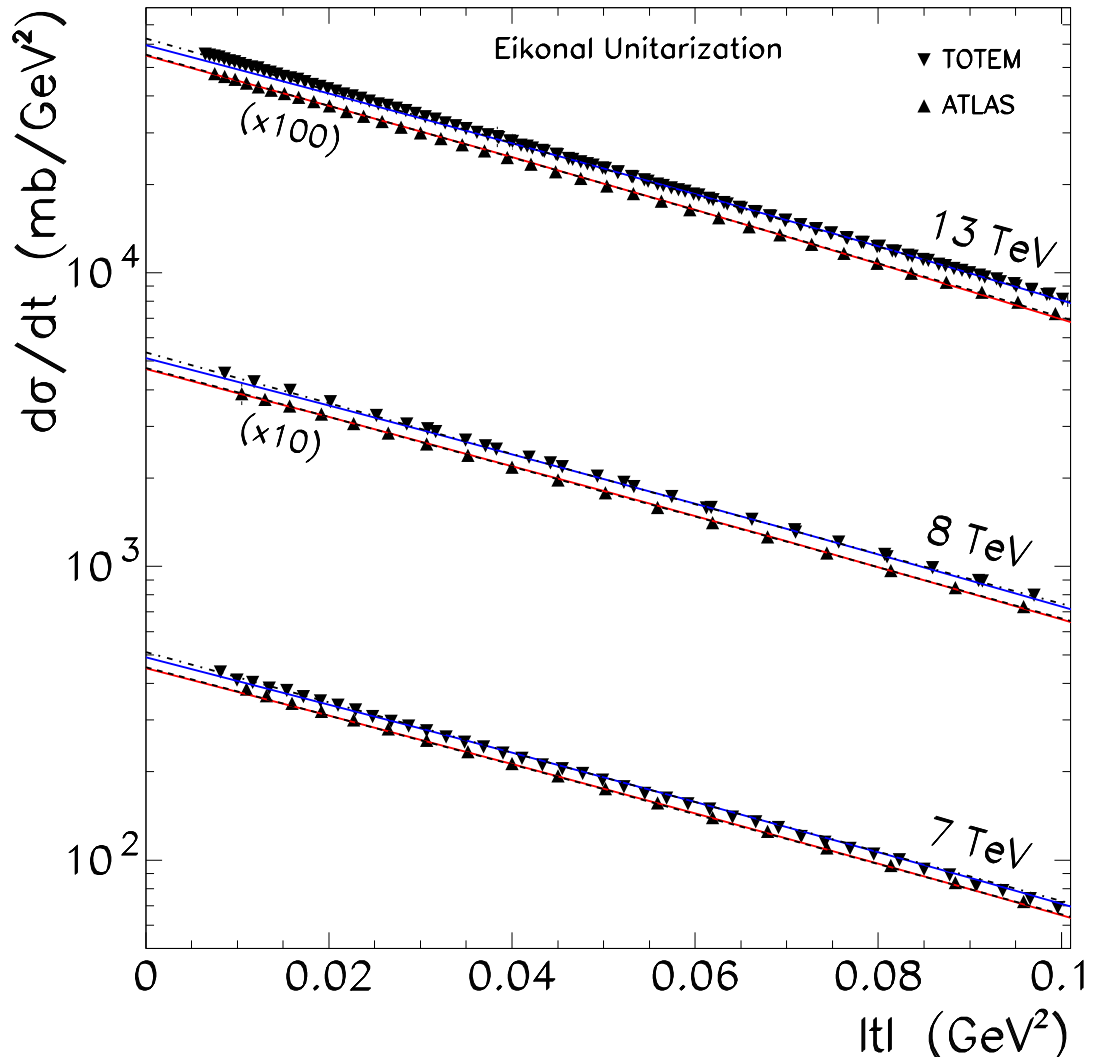


Figure 6.6: Differential cross-section for pp (\blacktriangle , \blacktriangledown) channel. Results obtained using eikonal unitarization for Models III and IV using $\xi_0 = -1$.

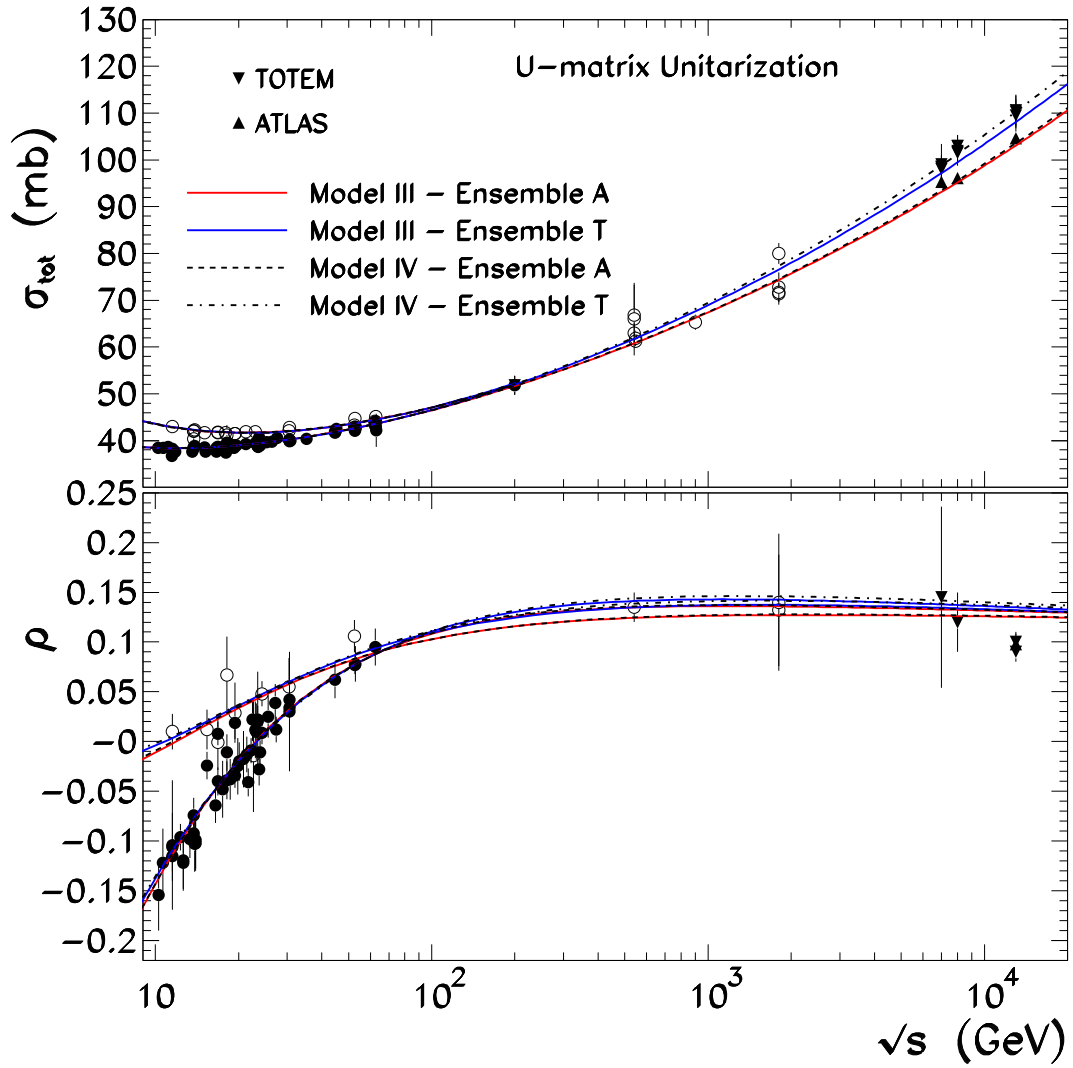


Figure 6.7: Total cross-section and ρ parameter fits for pp (\bullet , \blacktriangle , \blacktriangledown) and $p\bar{p}$ (\circ) channels. Results obtained using U-matrix unitarization for Models III and IV using $\xi_0 = -1$.

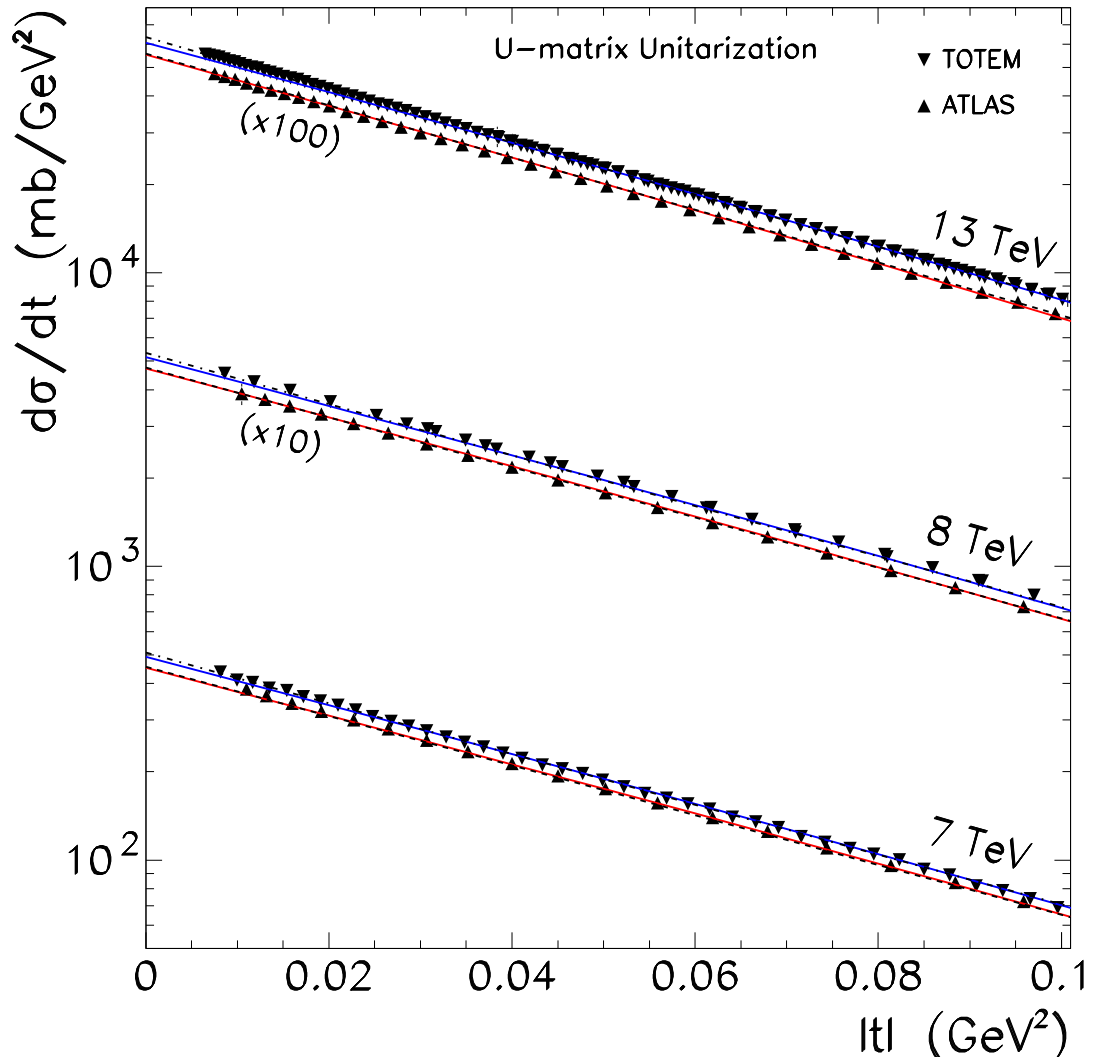


Figure 6.8: Differential cross-section for pp (\blacktriangle , \blacktriangledown) channel. Results obtained using U-matrix unitarization for Models III and IV using $\xi_0 = -1$.

6.2.2| The $\xi_0 = +1$ case

The results taking the positivity factor $\xi_0 = +1$ for all datasets and unitarization schemes did not show significant differences with the models without the Odderon. The fitting procedure showed that the Odderon-hadron coupling $\beta_0(0)$ took values compatible with zero. Meanwhile, the values of the rest of the fitted parameters did not show significant changes relative to the cases that did not include the Odderon. Due to this, the results for $\xi_0 = +1$ are not shown explicitly.

6.3| Comparisons for all models at high energy

Figures 6.9 and 6.10 highlight the fit results for all the models, for both datasets. Figure 6.9 offers side-by-side comparisons for Models I, II III and IV in the eikonal case. Figure 6.10 illustrates the different results for the U-matrix scheme.

It is possible to see, for example, how the results for both the eikonal and U-matrix case seem highly sensitive to the choices of form factor for the Pomeron and Odderon. Moreover, these differences become more pronounced in the fits for TOTEM data.

The inclusion of the Odderon at these energy levels does not seem to lead to major differences between the plots of the Pomeron only fits (when looking at the models with the same form factor). This is coherent with the small Odderon-hadron couplings that were found for the models used. However, it is worth noting that the inclusion of the Odderon leads to a decrease in the intercept and coupling predictions for the negative signature secondary Reggeons. In particular, it takes the odd secondary intercept to values closer to the trajectory outlined by the PDG data in Figure 5.4.

It is important to highlight as well that the model for the Odderon as a simple pole is not enough to reflect the experimental values for the ρ parameter at 13 TeV. A more complex model is required to have better agreement with these data points. In particular, this would be necessary to improve the results in the forward region (for σ_{tot} and ρ). A model of these characteristics could also lead to more significant effects for the Odderon contribution at high energy in the total cross-sections.

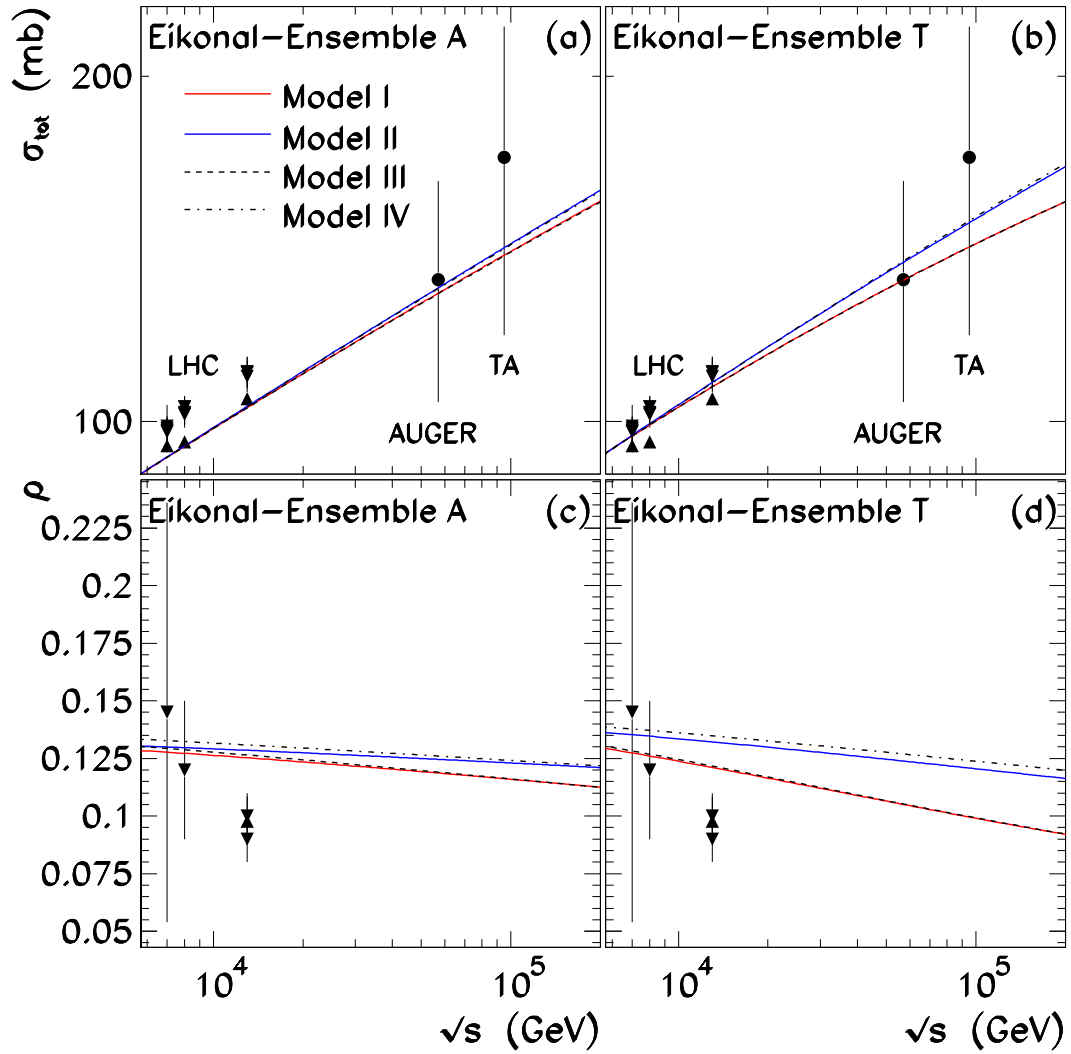


Figure 6.9: High-energy comparison of results for Models I, I, III, and IV in the eikonal scheme. Also included is $\sigma_{\text{tot}}^{\text{pp}}$ data obtained from cosmic-ray experiments (AUGER and TA).

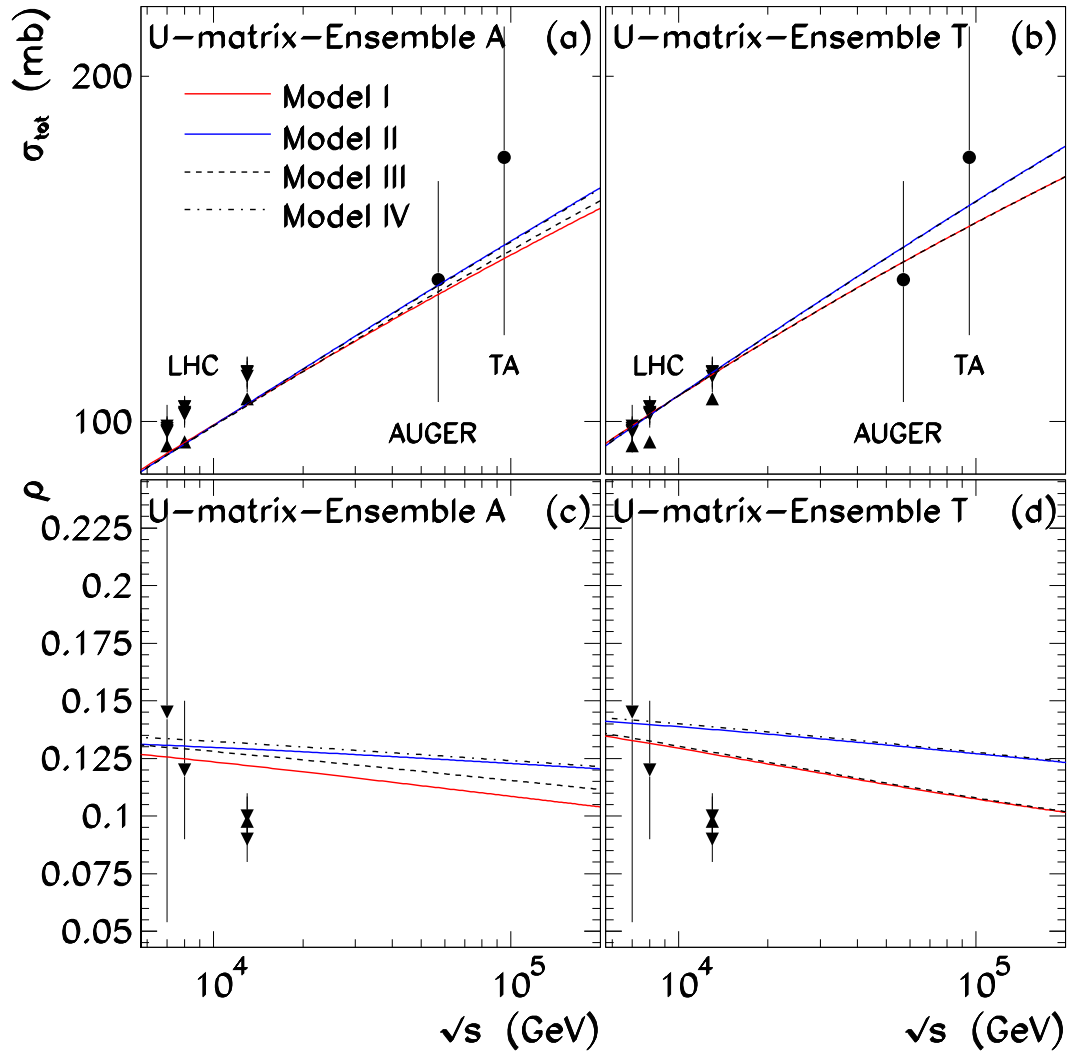


Figure 6.10: High-energy comparison of results for Models I, I, III, and IV in the U-matrix scheme. Also included is $\sigma_{\text{tot}}^{\text{pp}}$ data obtained from cosmic-ray experiments (AUGER and TA)

7 Conclusions

This thesis focused on the study of hadronic scattering through the phenomenological approach of Regge Theory. For this purpose, we carried out χ^2 fits which took into account the latest high-energy data from experiments TOTEM and ATLAS at the LHC. The total cross-section, ρ parameter and elastic differential cross-section were the observables included in the analysis.

The predictions for these observables in the language of Regge theory are dominated by the Pomeron. However, there has been renewed interest in the Odderon contributions, due to its detection at TOTEM. Therefore, our models also took into account this Reggeon. The results for the fits and fit parameters were compared in many aspects, as the fits were based on many different models.

First and foremost, two datasets were used, which led to some discrepancies in the results. The cross-section and differential cross-section data for TOTEM and ATLAS show significant differences. This resulted in different estimates for relevant parameters such as the Pomeron intercept $\alpha_{\mathbb{P}}$. Although the value of χ^2/ν is lower for TOTEM fits, this should not be taken as an indication of higher validity results, as it is likely due to the higher number of degrees of freedom in Ensemble T. In fact, it is worth noting that the ATLAS data has smaller errors. Perhaps future measurements will shed more light on this regard.

The calculations were also performed utilizing two unitarization schemes, the eikonal and the U-matrix. The goal was to distinguish which one of them produces better agreement with experiments. This was motivated by the availability of higher energy data, as the schemes are expected to differ at asymptotically high energy. At this stage, it was not possible to draw significant distinctions between the results produced by both unitarization methodologies. This could be an indication that “asymptopia” has not yet been reached. It is also worth mentioning that the Odderon was typically omitted in previous studies of the unitarization schemes, representing a further contribution of this work to the topic.

The analysis also compared the results using exponential and power-like form factors for hadron-Pomeron and hadron-Odderon vertices. The results tend to favor

power-like factors, particularly for TOTEM data, as evidenced by the lower values of χ^2/ν for Models II and IV. However, it is worth recalling that these form factors regulate the t -variation of scattering amplitudes. Our fits focused only on the quasi-forward region, and although the differential cross-section fits give good results in this region, they may not be as accurate at higher t .

There are also some interesting results stemming from the inclusion of the Odderon. The Odderon coupling was studied for two possible phases in the Odderon amplitudes. This property of the Odderon is *a priori* unknown. Our analysis showed that, in order to have a non-zero coupling for the Odderon, the positivity factor representing the phase must be $\xi_0 = -1$. This choice was favored by our fit results.

Our estimates for the Odderon-hadron coupling $\beta_0(0)$ confirm that, even with $\xi_0 = -1$, the Odderon interacts significantly more weakly with protons than the Pomeron and secondary Reggeons. This is well in line with the difficulties in finding evidence of its effect. It also explains why the presence of the Odderon does not lead to particularly significant deviations from the Pomeron-only models. For example, it does not correct the fact that our fits do not show good agreement with the newest measurements of the ρ parameter. It is likely that a simple-pole model for the Odderon is not enough to reflect this behavior and a more complex model is needed.

Lastly, the Odderon leads to differences in the pp and $p\bar{p}$ predictions for the ρ parameter. Due to being an odd-signature Reggeon the Odderon is expected to distinguish between the proton and antiproton. However, our models show an effect not obtained by simply taking into account the crossing-odd meson trajectories. The effect consists of a visible “crossing” that occurs between the pp and $p\bar{p}$ ρ -parameter fits, occurring at intermediate energies.

To summarize, our results contribute some insight into many aspects of the phenomenology of diffractive hadron scattering. Some further work could consist of improving the models, in particular for the inclusion of the Odderon. However, in the case of unitarization and the parameter discrepancies for TOTEM and ATLAS, further experimental data will likely be necessary to provide more clarity. The perhaps most interesting result obtained is that we verified that a positivity factor $\xi_0 = -1$ is necessary to obtain a non-zero Odderon-proton coupling.

Bibliography

- [1] S. Eidelman and F. Jegerlehner, *Zeitschrift für Physik C Particles and Fields* **67**, 585 (1995).
- [2] J. C. R. Bloch, A. Cucchieri, K. Langfeld, and T. Mendes, *Nuclear Physics B* **687**, 76 (2004).
- [3] Particle Data Group, *Progress of Theoretical and Experimental Physics* **2022**, 083C01 (2022).
- [4] T. Regge, *Il Nuovo Cimento* **14**, 951 (1959).
- [5] V. N. Gribov, *Zhur. Eksptl'. i Teoret. Fiz.* **Vol: 41** (1961).
- [6] M. Froissart, *Physical Review* **123**, 1053 (1961).
- [7] G. F. Chew and S. C. Frautschi, *Phys. Rev. Lett.* **7**, 394 (1961).
- [8] A. Martin, *Physical Review* **129**, 1432 (1963).
- [9] E. Martynov and B. Nicolescu, *Phys. Lett. B* **778**, 414 (2018).
- [10] T. Csörgő, T. Novák, R. Pasechnik, A. Ster, and I. Szanyi, *The European Physical Journal C* **81**, 180 (2021).
- [11] M. Gell-Mann, *Phys. Lett.* **8**, 214 (1964).
- [12] M. E. Peskin and D. V. Schroeder, *An Introduction To Quantum Field Theory*, Avalon Publishing, 1995.
- [13] N. Isgur and J. Paton, *Physical Review D* **31**, 2910 (1985).
- [14] A. Nakamura and T. Saito, *Physics Letters B* **621**, 171 (2005).
- [15] F. Halzen and A. D. Martin, *Quarks and Leptons: An Introductory Course in Modern Particle Physics*, Wiley, 1984.
- [16] M. Breidenbach et al., *Physical Review Letters* **23**, 935 (1969).
- [17] E. D. Bloom et al., *Physical Review Letters* **23**, 930 (1969).
- [18] D. J. Gross and F. Wilczek, *Physical Review Letters* **30**, 1343 (1973).
- [19] H. D. Politzer, *Physical Review Letters* **30**, 1346 (1973).

-
- [20] M. Göckeler et al., *Physical Review Letters* **80**, 4119 (1998).
- [21] M. E. Peskin, Chiral Symmetry, in *Concepts of Elementary Particle Physics*, edited by M. E. Peskin, pages 215–227, Oxford University Press, 2019.
- [22] D. Griffiths, *Introduction to Elementary Particles*, Wiley, 2008.
- [23] V. Barone and E. Predazzi, *High-Energy Particle Diffraction*, Springer Berlin Heidelberg, Berlin, Heidelberg, 2002.
- [24] Particle Data Group, *Progress of Theoretical and Experimental Physics* **2020**, 083C01 (2020).
- [25] E. L. Feinberg and I. Pomerančuk, *Il Nuovo Cimento* **3**, 652 (1956).
- [26] K. Vlastimil, Diffraction and rapidity gap measurements with ATLAS, in *Proceedings of International Conference on the Structure and the Interactions of the Photon Including the 20th International Workshop on Photon-Photon Collisions and the International Workshop on High Energy Photon Linear Colliders — PoS(Photon 2013)*, page 21, Paris, France, 2014, Sissa Medialab.
- [27] J. Prochazka, *Elastic Proton-Proton Collisions at High Energies*, PhD thesis, Charles University, 2016.
- [28] J. A. Wheeler, *Physical Review* **52**, 1107 (1937).
- [29] W. Heisenberg, *Zeitschrift für Physik* **120**, 513 (1943).
- [30] F. J. Dyson, *Physical Review* **75**, 1736 (1949).
- [31] A. R. White, Chapter 4.1.3 - The Past and Future of S-Matrix Theory, in *Scattering*, edited by R. Pike and P. Sabatier, pages 1483–1504, Academic Press, London, 2002.
- [32] R. J. Eden, P. V. Landshoff, D. I. Olive, and J. C. Polkinghorne, *The Analytic S-Matrix*, Cambridge University Press, 2002.
- [33] R. Oehme, *Group 10 - Theory of the Scattering Matrix (1942-1946). An Annotation*, volume 2 of *Collected Works / Gesammelte Werke*, pages 602–610, Springer-Verlag, first edition, 1989.
- [34] G. F. Chew, The S-Matrix Theory of Strong Interactions, Technical Report UCRL-9701, Lawrence Radiation Laboratory, 1961.
- [35] C. Møller, *Matematisk-Fysiske Meddelelser* **23** (1945).
- [36] R. G. Newton, *American Journal of Physics* **44**, 639 (1976).
- [37] M. Broilo, *Dinâmica Não-Perturbativa de Colisões Hadrônicas*, PhD thesis, Universidade Federal de Rio Grande do Sul, 2019.
- [38] P. D. B. Collins, *An Introduction to Regge Theory and High Energy Physics*, Cambridge University Press, 1977.

BIBLIOGRAPHY

- [39] M. L. Goldberger and K. M. Watson, *Collision Theory*, Courier Corporation, 2004.
- [40] E. C. Titchmarsh, *The Theory of Functions*, Oxford University Press, 1939.
- [41] J. Pila, *Rocky Mountain Journal of Mathematics* **35** (2005).
- [42] G. N. Watson and J. W. Nicholson, *Proceedings of the Royal Society of London. Series A, Containing Papers of a Mathematical and Physical Character* **95**, 83 (1997).
- [43] A. Sommerfeld, *Partial Differential Equations in Physics*, Academic Press, 1949.
- [44] Bateman Manuscript Project and H. Bateman, *Higher Transcendental Functions*, volume 1, McGraw-Hill Book Company, 1953.
- [45] G. F. Chew, *S-matrix Theory with Regge Poles*, in *14th Solvay Conference on Physics: Fundamental Problems in Elementary Particle Physics*, pages 65–96, London, 1968, Interscience.
- [46] J. R. Forshaw and D. A. Ross, *Quantum Chromodynamics and the Pomeron*, Cambridge Lecture Notes in Physics, Cambridge University Press, Cambridge, 1997.
- [47] A. B. Kaidalov, *Regge Poles in QCD*, volume 1, pages 603–636, 2001.
- [48] A. Martin and S. M. Roy, *Physical Review D* **91**, 076006 (2015).
- [49] L. N. Lipatov, *Sov. J. Nucl. Phys.* **23**, 338 (1976).
- [50] E. A. Kuraev, L. N. Lipatov, and V. S. Fadin, *Sov. Phys. JETP* **44**, 443 (1976).
- [51] E. A. Kuraev, L. N. Lipatov, and V. S. Fadin, *Sov. Phys. JETP* **45**, 199 (1977).
- [52] I. I. Balitsky and L. N. Lipatov, *Sov. J. Nucl. Phys.* **28**, 822 (1978).
- [53] L. N. Lipatov, *Sov. Phys. JETP* **63**, 904 (1986).
- [54] H. N. Chehime and D. Zeppenfeld, *Evidence for a Hard Pomeron in Perturbative QCD*, 1994.
- [55] S. Nussinov, *Physical Review Letters* **34**, 1286 (1975).
- [56] F. E. Low, *Physical Review D* **12**, 163 (1975).
- [57] L. Łukaszuk and B. Nicolescu, *Lettere al Nuovo Cimento (1971-1985)* **8**, 405 (1973).
- [58] R. J. M. Covolan, J. Montanha, and K. Goulianos, *Physics Letters B* **389**, 176 (1996).
- [59] J. R. Cudell and O. V. Selyugin, *Czechoslovak Journal of Physics* **54**, A441 (2004).
- [60] S. M. Troshin and N. E. Tyurin, *Fizika Ehlementarnykh Chastits i Atomnogo Yadra* **35** (2003).

-
- [61] B. Kopeliovich, B. Povh, and E. Predazzi, *Physics Letters B* **405**, 361 (1997).
- [62] G. Falcioni, E. Gardi, N. Maher, C. Milloy, and L. Vernazza, *Physical Review Letters* **128**, 132001 (2022).
- [63] E. Martynov, *Physical Review D* **76**, 074030 (2007).
- [64] O. V. Selyugin, J. R. Cudell, and E. Predazzi, *The European Physical Journal Special Topics* **162**, 37 (2008).
- [65] T. Adachi and T. Kotani, *Progress of Theoretical Physics Supplement* **65**, 316 (1965).
- [66] P. Desgrolard, L. Jenkovszky, and B. V. Struminsky, *Physics of Atomic Nuclei* **63**, 891 (2000).
- [67] M. Broilo, D. A. Fagundes, E. G. S. Luna, and M. Peláez, *Physical Review D* **103**, 014019 (2021).
- [68] P. M. Nadol'skij, Odderon contribution in U-matrix method, Technical Report IHEP-OTF-91-113, USSR, 1991.
- [69] M. Giffon, E. Martynov, and E. Predazzi, *Zeitschrift für Physik C Particles and Fields* **76**, 155 (1997).
- [70] A. Anselm and V. Gribov, *Physics Letters B* **40**, 487 (1972).
- [71] V. A. Khoze, A. D. Martin, and M. G. Ryskin, *The European Physical Journal C - Particles and Fields* **18**, 167 (2000).
- [72] E. G. S. Luna, V. A. Khoze, A. D. Martin, and M. G. Ryskin, *The European Physical Journal C* **59**, 1 (2009).
- [73] D. Brömmel, *Pion Structure from the Lattice*, PhD thesis, Regensburg U., 2007.
- [74] H. B. O'Connell, B. C. Pearce, A. W. Thomas, and A. G. Williams, *Progress in Particle and Nuclear Physics* **39**, 201 (1997).
- [75] A. Szczurek, N. N. Nikolaev, and J. Speth, *Physical Review C* **66**, 055206 (2002).
- [76] V. A. Khoze, A. D. Martin, and M. G. Ryskin, *Journal of Physics G: Nuclear and Particle Physics* **42**, 025003 (2015).
- [77] P. Desgrolard, M. Giffon, E. Martynov, and E. Predazzi, *European Physical Journal C: Particles and Fields* **9**, 623 (1999).
- [78] A. Donnachie and P. V. Landshoff, *Physics Letters B* **296**, 227 (1992).
- [79] V. Khoze, A. Martin, and M. Ryskin, *Physical Review D* **97** (2018).
- [80] N. Armesto and M. A. Braun, *Zeitschrift für Physik C Particles and Fields* **75**, 709 (1997).
- [81] J. Bartels, L. N. Lipatov, and G. P. Vacca, *Physics Letters B* **477**, 178 (2000).

BIBLIOGRAPHY

- [82] Y. V. Kovchegov, L. Szymanowski, and S. Wallon, *Physics Letters B* **586**, 267 (2004).
- [83] C. Ewerz, *The Odderon in Quantum Chromodynamics*, 2003.
- [84] B. Nicolescu, *Recent Advances in Odderon Physics*, in *Elastic and Diffractive Scattering*, pages 177–186, 2000.
- [85] E. Martynov and B. Nicolescu, *The European Physical Journal C* **79**, 461 (2019).
- [86] M. Broilo, D. A. Fagundes, E. G. S. Luna, and M. J. Menon, *Physics Letters B* **799**, 135047 (2019).
- [87] CERN | The TOTEM experiment, <https://totem-experiment.web.cern.ch/>.
- [88] ATLAS Experiment at CERN, <https://atlas.cern/about>.
- [89] ATLAS Collaboration, *European Physical Journal C* (2022).
- [90] The TOTEM Collaboration, *The European Physical Journal C* **79**, 785 (2019).
- [91] The TOTEM Collaboration, *The European Physical Journal C* **79**, 103 (2019).
- [92] ATLAS Collaboration, *Nuclear Physics B* **889**, 486 (2014).
- [93] ATLAS Collaboration, *Physics Letters B* **761**, 158 (2016).
- [94] The TOTEM Collaboration, *Europhysics Letters* **96**, 21002 (2011).
- [95] The TOTEM Collaboration, *The European Physical Journal C* **76**, 661 (2016).
- [96] F. James and M. Winkler, *MINUIT User's Guide*, 2004.
- [97] W. T. Eadie, D. Drijard, F. E. James, M. Roos, and B. Sadoulet, *Statistical methods in experimental physics; 1st ed.*, North-Holland, Amsterdam, 1971.

Appendices

A Useful Tools in Particle Scattering

A.1| Units

In the context of Quantum Field Theory and high-energy physics, the units of physical quantities are redefined in order to simplify expressions. This system, known as *natural units* stems from setting Planck's constant \hbar and the speed of light in the vacuum c to $\hbar = c = 1$. Therefore, these constants are omitted from equations. If their inclusion becomes necessary, they can be reintroduced by studying the dimensionality of the results.

The standard units of energy in this context are GeVs. From this choice, and using

$$E^2 = p^2c^2 + m^2c^4, \tag{A.1}$$

one finds that the natural units of mass and momentum have energy dimensions. Considering further known physical relations provides the units for other quantities. The following table shows some relevant examples:

Quantity	SI Units	Natural Units
Mass	kg	E
Length	m	1/E
Time	s	1/E
Momentum	kg·m/s	E
Velocity	m/s	-
Charge	C	-
Angular Momentum	kg·m ² /s	-

Table A.1: Dimensions in natural units for relevant quantities.

A.2| Mandelstam Variables

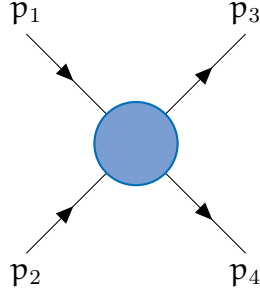


Figure A.1: Diagram illustrating the considered four-momenta.

Mandelstam variables are defined in terms of the external four-momenta of an interaction. The four-momentum of a particle generalizes its usual three-dimensional momentum vector to spacetime coordinates through the inclusion of the relativistic energy. As a result, the structure of a four-momentum four-vector is

$$\mathbf{p} = (E/c, p_x, p_y, p_z), \quad (\text{A.2})$$

where E is the energy, c is the speed of light, and p_i are the three-dimensional momentum components.

Mandelstam variables for a process $A + B \rightarrow C + D$ are defined as [12]:

$$s = (p_1 + p_2)^2 c^2 = (p_3 + p_4)^2 c^2 \quad (\text{A.3})$$

$$t = (p_3 - p_1)^2 c^2 = (p_4 - p_2)^2 c^2 \quad (\text{A.4})$$

$$u = (p_4 - p_1)^2 c^2 = (p_3 - p_2)^2 c^2 \quad (\text{A.5})$$

It is worth noting that the c^2 factor appearing in the definitions is typically omitted due to unit conventions, which are covered in Appendix A.1. These factors are left out of the remainder of this appendix and throughout the thesis.

When looking at relativistic particle interactions the usage of Mandelstam variables is widespread due to its convenience; these variables encode energy, momentum and angle information in a compact Lorentz invariant manner. Appendix B will shed more light on the relations for Mandelstam variables for two-particle equal-mass scattering in the center-of-mass frame, as used throughout this thesis.

Exchanging the roles of these variables is equivalent to performing crossing operations, as described in Section 2.3.3. Note for example that switching momenta p_3 and p_4 is equivalent to exchanging t and u . In terms of Feynman diagrams the s , t and u channel processes for a two-body to two-body interactions are:

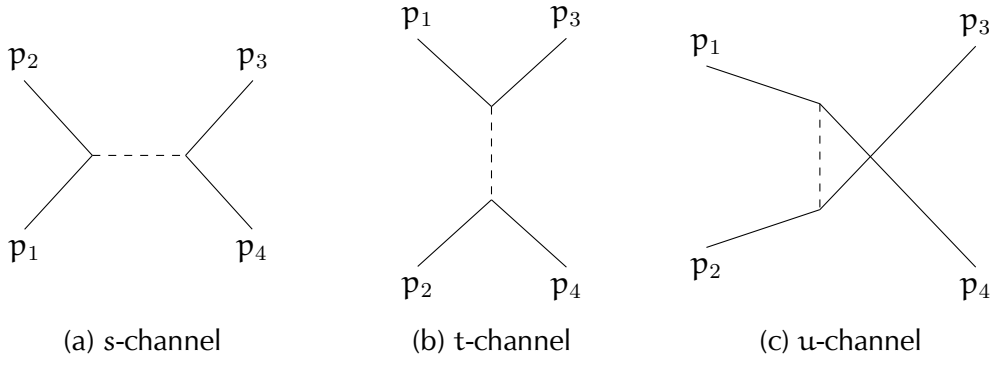


Figure A.2: Feynman diagrams for the different ()-channel reactions.

A very useful property of the Mandelstam variables is the fact that they are not independent from each other. By adding the expressions for the variables and imposing conservation of momentum $(p_1 + p_2 - p_3 - p_4)^2 = 0$ one obtains the following relation:

$$s + t + u = \sum_i m_i^2 \quad (\text{A.6})$$

where the right-hand side of the equation represents the sum over the square masses of all the interacting particles ($p_i^2 = m_i^2$).

B Kinematics

Throughout the thesis, and for the sake of simplicity, relativistic scattering processes are expressed in the center-of-mass system of reference. This appendix outlines some useful expressions for this case, particularly for the Mandelstam variables.

An s-channel reaction $1 + 2 \rightarrow 3 + 4$ in the center-of-mass system should have $\vec{p}_1 + \vec{p}_2 = 0$. Taking into account momentum conservation, if incoming particles 1 and 2 travel along the z-axis with momentum p_z , the 4-momenta of the particles are:

$$p_1 = (E_1, 0, 0, p_z) \quad (\text{B.1})$$

$$p_2 = (E_2, 0, 0, -p_z) \quad (\text{B.2})$$

$$p_3 = (E_3, \vec{p}_\perp, p'_z) \quad (\text{B.3})$$

$$p_4 = (E_4, -\vec{p}_\perp, -p'_z). \quad (\text{B.4})$$

The momentum of the outgoing particles is expressed in terms of z-axis component p'_z and two-dimensional transverse momentum \vec{p}_\perp . These components can be related to the outgoing momentum vector \vec{p}' through scattering angle θ , as defined in Figure B.1

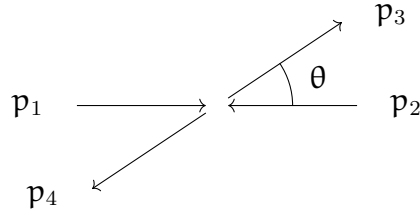


Figure B.1: Momenta and scattering angle in the center-of-mass system.

Then the components of outgoing momenta can be written as:

$$p'_z = |\vec{p}'| \cos \theta \quad (\text{B.5})$$

$$|p_{\perp}| = |\vec{p}'| \sin \theta. \quad (\text{B.6})$$

These relations, alongside the mass-shell conditions of the form $p^2 = E^2 - \vec{p}^2 = m^2$ lead to center-of-mass expression for the Mandelstam invariants.

The s variable is related to the energies of the four particles in the process as follows:

$$E_1 = \frac{1}{\sqrt{2s}}(s + m_1^2 - m_2^2) \quad (\text{B.7})$$

$$E_2 = \frac{1}{\sqrt{2s}}(s + m_2^2 - m_1^2) \quad (\text{B.8})$$

$$E_3 = \frac{1}{\sqrt{2s}}(s + m_3^2 - m_4^2) \quad (\text{B.9})$$

$$E_4 = \frac{1}{\sqrt{2s}}(s + m_4^2 - m_3^2). \quad (\text{B.10})$$

In the high-energy limit ($s \rightarrow \infty$) these expressions reduce to $E_i = \sqrt{s}/2$ for all $i = 1, \dots, 4$. Note that the total energy of the system in this limit obeys $E = \sqrt{s}$, which is why the s variable is commonly used to refer to the scattering energy.

A further simplification that was used throughout this work was taking the equal-mass (elastic) case expressions, where $m_1 = m_2 = m_3 = m_4 = m$. From the equations for the energy it is possible to visualize that, in the high energy limit, the differences between the on-shell masses of the particles can be neglected, and the equal-mass limit can be used to approximate more general cases. The approximation produces straightforward relations between the momenta and scattering angle and the

Mandelstam variables, leading to:

$$\cos \theta = 1 + \frac{2t}{s - 4m^2} \quad (\text{B.11})$$

$$s = 4(\vec{p}^2 + m^2) \quad (\text{B.12})$$

$$t = -2\vec{p}^2(1 - \cos\theta) \quad (\text{B.13})$$

From the last equation, it is clear that in the forward scattering direction ($\theta = 0$) t becomes zero.

By using (A.6) it is also possible to write:

$$u = -2\vec{p}^2(1 + \cos\theta). \quad (\text{B.14})$$

For t and u -channel scattering, there are analogous results. For a t -channel process with scattering angle θ_t one gets:

$$\cos \theta_t = 1 + \frac{2s}{t - 4m^2}, \quad (\text{B.15})$$

and in the u -channel, for scattering angle θ_u :

$$\cos \theta_u = 1 + \frac{2t}{u - 4m^2} \quad (\text{B.16})$$

Then applying a crossing operation for t -channel scattering it is worth noting that $u(-z_t, t) = s(z_t, t)$, where $z_t = \cos \theta_t$. This can be proven by writing (from (B.15)):

$$s = \frac{1}{2}(z_t - 1)(t - 4m^2) = \frac{1}{2}(z_t t - z_t 4m^2 - t + 4m^2), \quad (\text{B.17})$$

then u can be obtained using (A.6)

$$u = 4m^2 - t - \frac{1}{2}(z_t t - z_t 4m^2 - t + 4m^2) = \frac{1}{2}(-z_t - 1)(t - 4m^2). \quad (\text{B.18})$$

Therefore, $u(-z_t, t) = s(z_t, t)$.